POLITECNICO DI MILANO
Scuola di Ingegneria Industriale e dell'Informazione
Corso di Laurea in Ingegneria Nucleare

Optimization of the ion extraction from an Inductively Coupled Plasma (ICP) by IBSimu modeling

Relatore: Prof. Marco Beghi

Tesi di laurea di
Michele Doni
Matricola: 771048

Anno accademico 2012/2013

Contents

List of Figures

List of Tables

Abstract

Questo lavoro di tesi è finalizzato a raggiungere una più profonda comprensione del processo di estrazione di un fascio di ioni da un Inductively Coupled Plasma accoppiato a uno spettrometro di massa (utilizzato per l'analisi di soluzioni radioattive). In particolare, lo studio è stato focalizzato sulla plasma torch e sull'extraction interface - costituita da sampler e skimmer. Per capire i processi che avvengono tra lo skimmer - a valle del quale il plasma perde la sua quasi-neutralità - e la prima lente ottica, è stato utilizzato IBSimu, un software appositamente creato da T. Kalvas per simulare l'estrazione di ioni ed elettroni da una sorgente di plasma. Il profilo del fascio e la discriminazione in massa in corrispondenza della lente ottica sono stati studiati in funzione dei due principali parametri del plasma: il potenziale di plasma e la temperatura degli elettroni. Si è determinata la coppia di valori che massimizza l'efficienza dello strumento e si è verificata una buona corrispondenza con i dati sperimentali.

Abstract

The aim of this thesis work is to reach a better understanding of the extraction process from an ICP coupled to a mass spectrometer, used for radioactive solutions analysis. In particular this work is focused on the first two stages of the ICP-MS: the plasma torch and the extraction interface - formed by the sampler and the skimmer cones. In order to optimize the extraction process, IBSimu, an ion optical simulation package, is used; this software has been conceived specifically for ions and electrons extraction from a plasma source. The beam profile and the mass discrimination at the extraction lens have been studied as a function of the plasma fundamental parameters: the plasma potential and the electron temperature. The best combination of these two values has been found and a good correspondence to the experimental ones has been assessed.

Chapter 1

Introduction

The present work is mainly the result of my trainee at the Paul Scherrer Institute (PSI), Villigen, Switzerland. To perform this work I was associated with the "Hot Laboratory" (OHLA) of said institute, a laboratory equipped with several experimental facilities for material research, in particular for the examination of highly toxic radioactive substances and components. For the measurement of radioactive solutions a Multi-Collector Inductively Coupled Plasma - Mass Spectrometer (MC-ICP-MS) is used. The objective of my trainee was the better understanding of the ion extraction process and the optimization of the working parameters of the ICP by IBSimu modeling, in order to maximize the ion signal at the extraction lens. IBSimu is a software package for the optical simulation of ions and electrons beams, developed at LBNL (Lawrence Berkely National Laboratory) in 2004. Being the inductively coupled plasma one of the most successful analytical plasma sources in emission as well as in mass spectrometry, a very large number of papers is available on this topic and on its applications; a large part of my activity was dedicated to the collection, analysis, comparison and harmonization of the literature. In particular, the focus was on the detailed description and understanding of the Fassel torch - where plasma is formed - and on the interface necessary to transmit the ions into the spectrometer. The study of the literature allowed a good understanding of the extraction process and lead to the selection of parameters needed as input for the computer simulation code.

This thesis is organized as follows: after a general introduction to mass spectrometry (MS), ICP-MS and its applications, a detailed discussion on the extraction process is conducted. How the plasma torch works and its operating conditions are described in Chapter 3; Chapter 4 provides a detailed and complete description of the extraction process, through both the sampler and the skimmer cones. The theoretical description is placed side by side with the equations taken from the literature. The simulation software used in the work is introduced in Chapter 5: its main features are described and the functions of the code are explained. The simulation work in Chapter 6 has two main purposes: (i) find the best combination between plasma potential (U_p) and electron temperature (T_e) in order to have a beam profile - at the extraction lens - represented by a high and sharp peak and

(ii) characterize the plasma of the instrument used (the Neptune MC-ICP-MS). These two achievements were reached step by step; as a consequence it resulted convenient to divide Chapter 6 in different sections, in each one a particular issue - contributing to the final result - is solved and discussed. Since three months are a sufficient period to understand the working of the ICP, but not to overcome its limitations, several efforts are still necessary to use at best this instrument; in Chapter 7 some suggested updates are discussed, both for the simulation and the experimental setup.

Chapter 2

Mass spectrometry

Mass spectrometry (MS) is among[1] the most accurate techniques for the determination of relative molecular weights; for this reason and also thanks to its unique capabilities - ultrahigh detection sensitivity and applicability to all elements and to all types of samples - it is wide popular. MS is an analytical technique in which ions are generated from either inorganic or organic compounds, by any suitable method, and then separated by their mass-to-charge ratio (m/q) to detect their relative abundances. The analyzing process consists of three main steps: ions creation, mass selection and particle detection, as schematized in Figure 2.1. The ion source is required to vaporize, atomize and ionize the analyte. In fact it can be a liquid, a gas mixture or a solid; so the first step is to transform it into a vapour or an aerosol through the high temperature source. It is advantageous to supply as much energy as possible for this process [45]. A high volatilization efficiency is important in order to obtain a high sensitivity and for keeping the matrix interferences involved in the analyses as low as possible. There are different sources, suitable for different types of analysis; thermal ionization, electron impact, secondary ionization or the use of a plasma source are found in the majority of today's inorganic mass spectrometers. In turn, plasma sources can be found in different types, such as Capillary Arc Plasma (CAP) and Microwave Induced Plasma (MIP), but only Inductively Coupled Plasma (ICP) and Glow Discharge (GD) are having a commercial application at the present. Concerning the second step (mass selection), there are many types of mass analyzers; the instrument utilized in this study is an ICP-MS system, the Neptune MC-ICP-MS,[2] from Thermo Scientific. It's a double focusing sector field instrument, that is a device that bends the ions trajectories using a magnetic sector field, and focuses them through an electric sector; these two devices are shown in Figure 2.2 and Figure 2.3.

In the final step, the detector records either the charge induced or the current produced when an ion passes by or hits a surface; the most used detectors are electron multipliers, Faraday cups and ion-to-photon detectors.

[1] Some other techniques are: Laser Light Scattering, Chromatography, Ultracentrifugation, Fourier Transform Infrared Spectroscopy and Electrophoresis.

[2] MC stands for Multi Collector.

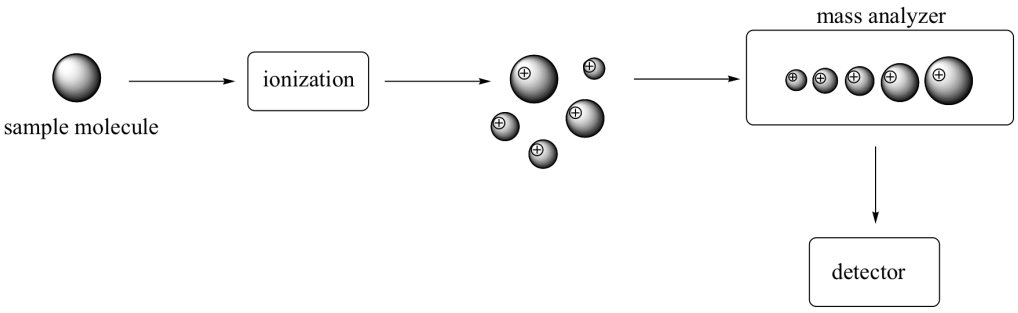

Figure 2.1: Fundamental steps in mass spectrometry (ChemWiki: The Dynamic Chemistry Textbook).

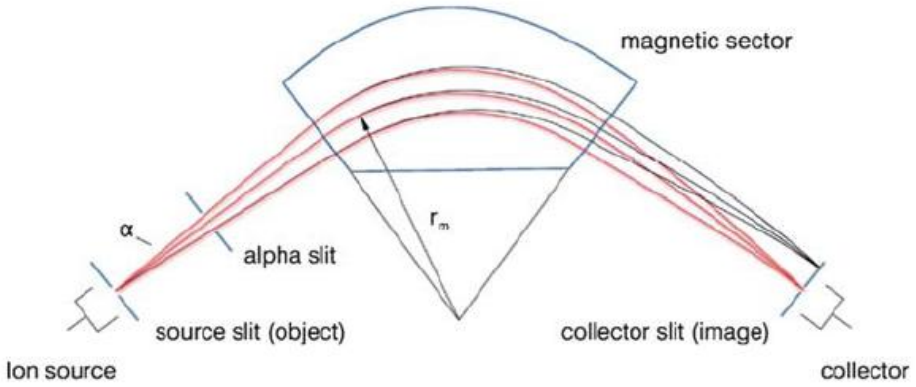

Figure 2.2: Sketch of the geometry of a magnetic sector arrangement [41].

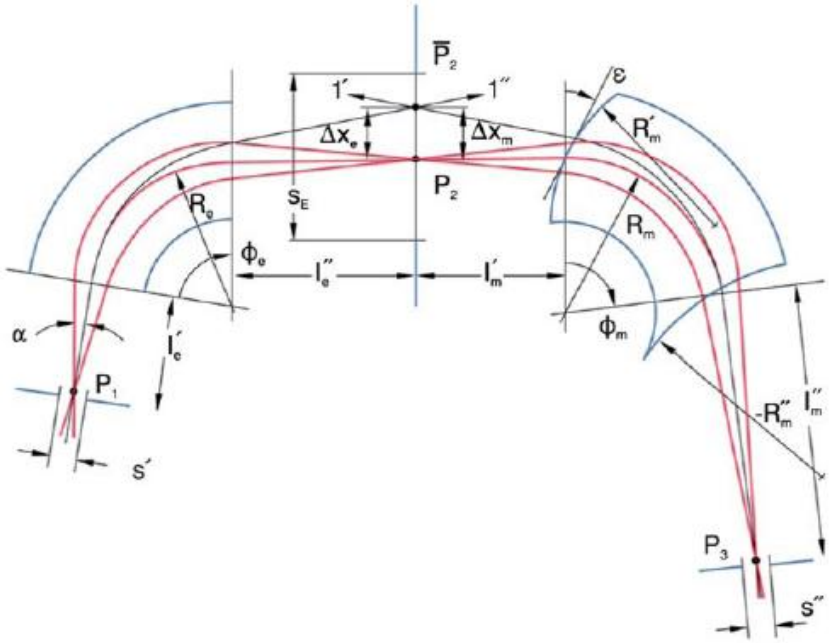

Figure 2.3: Schematic of an electric sector with a Nier-Johnson geometry [41].

2.1 Origin and early history of mass spectrometry

The history of mass spectrometry begins with studies regarding the nature of matter, in particular with the discovery of anode and cathode rays. In 1886 the German physicist Eugen Goldstein coined the term 'cathode rays' for the negatively-charged particles discovered by Johann Hittorf, which are emitted when electric current is forced through a vacuum tube [41]. He also discovered 'Kanalstrahlen' (canal rays), positively-charged particles formed when "electrons" are removed from gas particles in a glass tube filled with gas at reduced pressure and equipped with a perforated cathode. Two years later Wien demonstrated that these canal rays could be deflected by an electric and magnetic sector field. In 1906, J.J.Thomson, as a result of his explorations on the properties of cathode rays, discovered the electron,[3] validating his thesis that the fundamental unit was over 1000 times smaller than an atom. During his studies, he used an instrument (built with his laboratory assistant, E. Everett) for magnetic deflection of cathode rays, that could simultaneously measure e/m and e, thus indirectly measuring the mass of the electron [37]. This work laid the foundation of the mass spectrometry (MS) field. Some years later, in 1912, as part of his exploration

[3]In the same year he receveid the Nobel Prize in Physics "in recognition of the great merits of his theoretical and experimental investigations on the conduction of electricity by gases".

into the composition of canal rays, Thomson and his research assistant, Francis W. Aston, channelled a stream of ionized neon through a magnetic and an electric field and measured its deflection by placing a photographic plate in its path. They observed two patches of light on the photographic plate, which suggested two different parabolas of deflection, and concluded that neon gas is composed of atoms of two different atomic masses (i.e. of two isotopes). So, through what later would be recognized as the first mass spectrometer,[4] they determined the isotopic composition of other stable elements. In 1919, Aston significantly improved the instrument used, separating electric and magnetic fields, arranging them in a way that all ions are focused in the plane of the photo plate and giving the birth to the first full functional mass spectrometer. "For his discovery, by means of his mass spectrograph, of isotopes, in a large number of non-radioactive elements, and for his enunciation of the whole-number rule" Aston was awarded the Nobel Prize in Chemistry in 1922. Of the 283 nuclides of the 83 elements known in 1948, 202 nuclides of 71 elements were found by Aston.[5] In those same years Arthur J. Dempster reported on his mass spectrometer and established the basic theory and design of mass spectrometers, that are still used nowadays. He focused his works (and career) in mass spectrometry and its applications (leading in 1935 to his discovery of the uranium isotope ^{235}U). Based on ion optical calculations performed with Bartky, in 1929 he designed and built a spectrometer with a 180° magnetic sector geometry with directional and velocity focusing. Later, in 1934, he combined the instruments with new ion sources, such as an “electron impact” or “spark” source. Meanwhile, in 1932, Kenneth Bainbridge developed a mass spectrometer with a resolving power of 600 and a relative precision of one part on 10000. He used this instrument to verify the equivalence between mass and energy, $E = mc^2$. Continuing his work, in 1935 Dempster developed the first ‘scanning’ mass spectrometer. In this device, the separation between ions focused into an exit slit was already related directly to the m/z ratio; scanning was performed either by changing the magnetic field or the acceleration voltage. Later, he developed and used different ion sources, for ion generation: the electron impact source and the radio frequency spark source - a discharge generating a discontinuous short-term plasma. In the following years many scientist have been involved in the further development of instruments with directional and velocity focusing; it has to be mentioned the team of Mattauch and Herzog, which in 1934 significantly contributed to the development of double-focusing instruments. But it was the importance of isotopes to the Manhattan Project and World War II that really pushed MS into prominence as a useful tool. The main contribution was from an American physicist, Alfred Nier; he enriched µg amounts of ^{235}U

[4]This instrument used gas discharges tubes to generate ions, which were then passed through parallel electric and magnetic fields.

[5]So, as Thomson could be considered the father of mass spectrometry, Aston is definitely the father of isotopes.

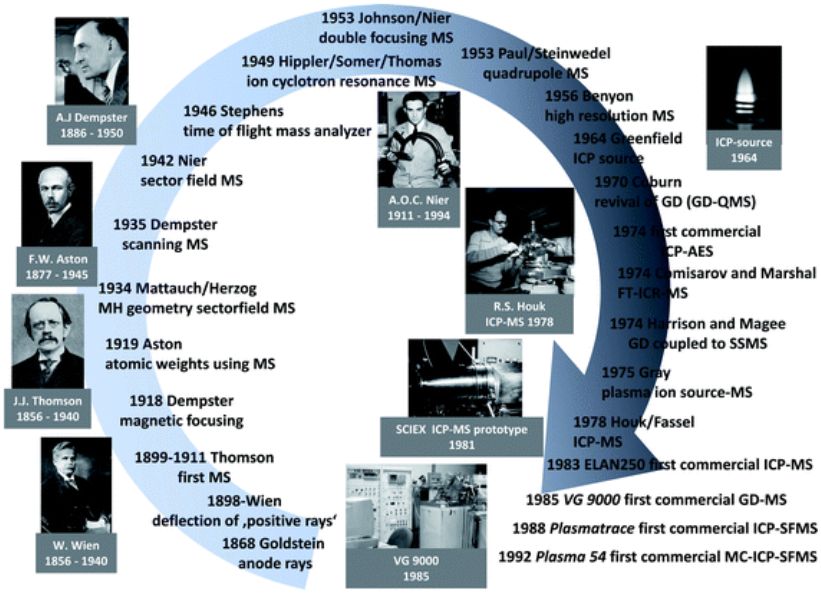

Figure 2.4: Some important events in mass spectrometry history [41].

from Uranium of natural isotope composition[6] and discussed with Johnson the theory known today as Nier-Johnson geometry.[7] Moreover Nier promoted the technique to the people outside the tight community of physicist to which he belonged. By the 1940s mass spectrometers were commercially available, even if they were very expensive; in addition MS utility was limited to quantitative analysis (information not really useful to academic chemists), only to concentration measurements. It is thought to be necessary remembering three american chemists: McLafferty, Biemann and Djerassi. Their work propelled MS into the consciousness of the chemistry community and laid the groundwork for modern biological MS research. The Inductively Coupled Plasma was started to be used as a plasma source only in the 1980s: a practical ICP-MS system was firstly described at the 9th International Mass Spectrometry Conference (Vienna, 1982) [25]. Even if it is a relatively recent instruments, nowadays ICP-MS is considered by several people a routine technique:[8] compared with some other methods of trace elemental analysis, maturity in ICP-MS has been reached very rapidly. A more detailed ICP-MS story is given in chapter 3.

[6] At the time scientists knew that one of the Uranium isotopes underwent slow neutron fission, but they were not sure which one; nobody had yet been able to separate the two isotopes to find out which one was responsible.

[7] An arrangement for a double-focusing mass spectrometer in which a deflection of $\pi/2$ radians in a radial electrostatic field analyser is followed by a magnetic deflection of $\pi/3$ radians; the electrostatic analyser uses a symmetrical object-image arrangement while the magnetic analyser is used asymmetrically.

[8] Using 2004 data, the sales of ICP-MS instruments are increasing by approximately 10% per year.

2.2 ICP-MS description

As said in the previous section, nowadays one of the most important methods in atomic spectrometry is the ICP-MS: the two main reasons for its success are the true multi-element capabilities and the extremely low detection limits.

All ICP sector field instruments consist of [41]:

- an ion source (see chapter 3 for a detailed description);
- a sampling interface (see chapter 4 for a detailed description);
- an electrostatic lens system, used to guide, focus and accelerate the positively charged ion beam onto the entrance slit and to shape the beam, giving it a more rectangular profile (in accordance to the geometry of the entrance slit);
- a magnetic sector, which bends ions according to their momentum; the electromagnet is typically operating in static mode (that is, at a constant field) and the field strength can be changed varying the electric current;
- an electric sector, where differences in ion energies are compensated to a certain extent;
- a curved flight tube, between the poles of the electromagnet;
- an entrance and an exit slit, to shape the geometry of the ion beam and to achieve a good resolution (which depends on the width of the incident ion beam and thus on the width of the entrance slit) ;
- zoom and/or filter optics: in the Neptune, a zoom lens and an energy filter, in order to maintain the direct guidance of the incoming ion beams into the detector and to permit ions with sufficiently high kinetic energies to pass only;
- a detection system, consisting - in the Neptune - of a number of Faraday detectors, arranged along the focal plane to measure all isotopes of interest simultaneously; in addition, there are also electron multipliers, discrete dynode detectors and channeltrons to monitor low isotopic abundance nuclides;
- a vacuum system, otherwise the ions would scatter and there would be a significant loss of transmission and sensitivity (see later for more details about different pressure regions).

It has to be underlined that two different configurations are possible; in the studied case the plasma source and the extraction interface are grounded, as ions are accelerated by the lens system potential. Other instruments have the opposite configuration, with the ion acceleration provided by the

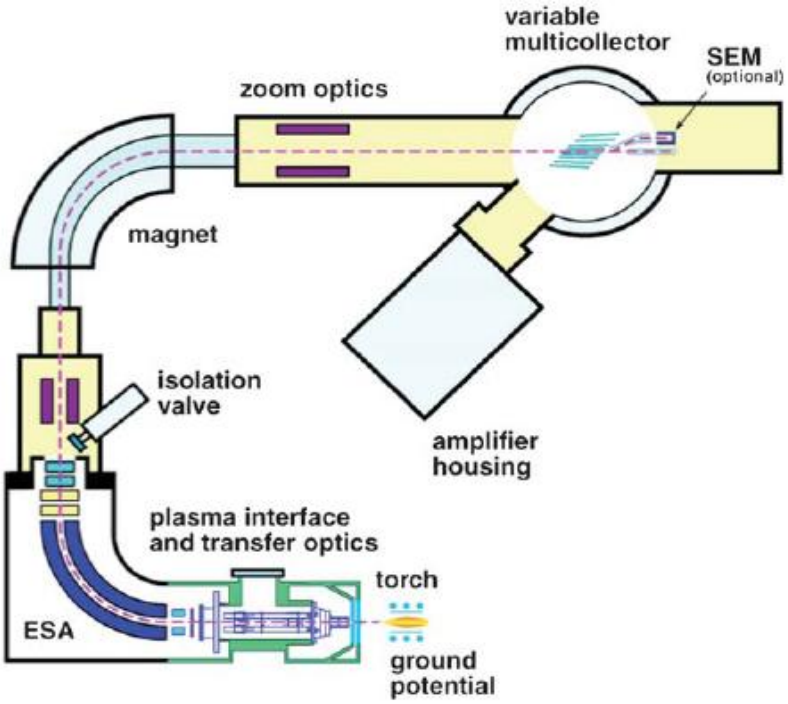

Figure 2.5: Schematic drawing of the Neptune MC-ICP-MS (Thermo Scientific) [41].

interface, posed at a high voltage. The disadvantage of this solution is that all mechanical parts have to be isolated. Moreover the risk of discharges caused by the conducting plasma is high [24]. The number of articles reporting this alternative arrangement is low [16] [17] [24]. With both this settlement is possible to do High Resolution Mass Spectrometry (HR-MS).

The present work is focused on the mass spectrometry first step: the analyte ionization through an ICP; therefore the following argumentation will be focused on the plasma source.[9]

2.3 ICP-MS applications

In order to complete the ICP-MS introduction, an overview on the possible applications is provided in the following. Referring to the examples chosen by Jakubowski et al. [42] in the sector field devices area, it is possible to group the applications in three categories:

- multi-element analysis,
- isotope ratio applications,

[9]Nowadays, ICP sources have a similar design in all commercially available instruments, independently on the type of mass separator [41].

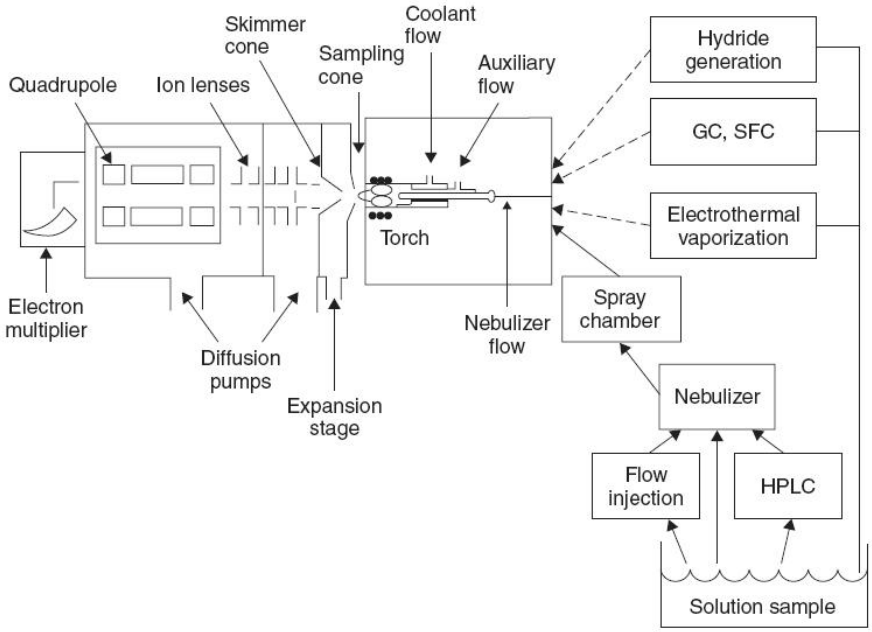

Figure 2.6: Schematic of an ICP-MS system. Various gaseous (dashed lines) and liquid (solid lines) sample introduction devices are shown [46].

- speciation analysis.

Multi-element analysis has been the major application area of sector field (SF) instruments during the last 15 years. The main reasons for their success are the capability of multi-element measurements, high sensitivity, low detection limits and fast and accurate direct data acquisition of the majority of nuclides suffering from spectral interferences at low mass resolution. ICP-SFMS is used for biological and environmental analyses: to determine element concentrations in body fluids - such as blood, urine and cerebrospinal fluid -, for the detection of trace elements in sections of human hairs, for monitoring Ca in biological samples - to study Ca pathways and metabolism -, in water research, to monitor the fate of heavy metals (including Rare Earth Elements) in the environment, for the direct multi-elemental determination of trace elements in diluted sea water and for soil samples analysis - in order to monitor heavy metal mobilization. In industrial applications and materials research, ICP-MS is mainly used in the semi-conductor industry and in the characterization of pure and ultra-pure materials; other applications are quality control of ultra-pure water, ammonia and acids, determination of the stoichiometry and trace impurities in thin barium strontium titanate perovskite layers (used in microelectronics), assessment of the purity of TlBr single crystals and forensic studies or provenance determination. Laser Ablation coupled to ICP-SFMS has to be mentioned because it is used either for bulk quantification of elements, for depth profiling or the identification of contamination spots. Concluding, multi-element analysis is used in food and nutrition science - for beverages,

vegetables, fish and infant food - and in geological and radionuclide applications - for studying trace element concentrations in geological samples, soils, sea water or sea water particulates[10] and radionuclide determination.

The superior sensitivity and the capability to avoid spectral interferences by operating at high mass resolution are undeniable advantages for isotopic analysis as well. Applications range in many fields: from biological to environmental samples, from geological to provenance and migration studies. Tracer experiments were conducted to investigate elemental fluxes in, e.g., the environment or metabolic processes; natural variations in the isotopic composition of selected elements are used for solving problems in a biological context; Pb composition analyses are used to distinguish between natural, geogenic Pb and anthropogenic Pb; through Sr isotopic analysis[11] is possible to trace the provenance of goods, agricultural products, food or even animals and humans - in archaeometry and forensics. Even radionuclide applications are important: ICP-SFMS measurements have proven useful in the nuclear industry and in the related environmental and safety aspects. Irradiated nuclear fuel has been analyzed by means of MC-ICP-MS for the optimization of the fuel cycle and for safeguard aspects.

At last, ICP-MS instruments are used in analytical problems related to biological systems or environment studies; information on speciation is required in order to understand processes related to toxicity, transport and bio-availability of metals or biological processes in which metals are involved. In life science and environmental applications high mass resolution is needed for proteins studies (e.g. for the characterization of metal containing or metal-binding proteins in biological systems), analysis and quantification (e.g. for selenoproteins, metalloproteins and protein-bound metals).

[10] Sea water temperatures can be calculated from Mg/Ca ratios.

[11] Isotopic and elemental signatures bear the potential of providing unique fingerprints which can be directly related to the origin of the sample investigated.

Chapter 3

Plasma torch

The ICP is generated in a discharge gas (Argon, in our case) without using any electrode, by the application of a high frequency electrical current to an induction coil, enveloping the plasma torch [41], as it will be explained in the following. The development of ICP sources began in 1942 [5], when Babat published his first paper on the properties of electrodeless discharges and realized the first ICP operating at atmospheric pressure. About 20 years later, Reed published two articles on his ingenious approach to the stabilization and thermal isolation of the producted plasmas. He underlined three properties that make ICP a superior source of atomization and ionization: high gas temperatures, capability of being sustained in noble gas environments and freedom from electrodes (representing a contamination). As a result of these good analytical performances, studies on ICP were started in 1962 and the first use of an Inductively Coupled Argon Plasma as an ion source for mass spectrometry dates from 1978 [12]. Sciex, Inc., introduced the first commercial instrument for ICP-MS at the 1983 Pittsburgh Conference, which catalyzed an explosive growth of interest in the technique [12]. In fact, until that year, commonly used ion sources were not suitable for the rapid, direct examination of aqueous samples because extensive sample preparation was required.[1] Then, several other instrument companies conducted ICP-MS research and, between 1985 and 2010, about 20 commercially available instruments were introduced to the market (considering both the ICP and the GD plasma source) [41]. For a complete list of the commercial sector field mass spectrometers with plasma based ion sources see Table 3.1.

To understand how an ICP works, it has to be known that high frequency currents flowing in an induction coil generate an oscillating magnetic field, whose lines of force are axially oriented inside the coil. In an ICP, the plasma torch - where plasma is generated - is enveloped in 2 or 3 turns of copper tube, cooled with either water or Argon; this settlement produces an electromagnetic inducted field by a time-varying magnetic field. The power

[1] The sample was evaporated onto a filament for thermal ionization or incorporated into an electrode for spark ionization before the sample-containing substrate was physically mounted in the vacuum system. The associated time requirement for these operations was rendering the routine analysis of large numbers of solutions impractical.

Table 3.1: Commercial sector field mass spectrometer with plasma based ion sources 1985-2010 [41]

Name	Manufacturer[a]	Year of introduction	Status	Type of instrument	Geometry
VG 9000	VG Elemental	1985	discontinued	GD-SFMS	reverse Nier-Johnson
Plasmatrace I	VG Elemental	1988	discontinued	ICP-SFMS	Nier-Johnson
JMS-Plasmax I	JEOL	1991	discontinued	ICP-SFMS	reverse Nier-Johnson
Plasma 54	VG Elemental	1992	discontinued	MC-ICP-SFMS	Nier-Johnson
Element	Finnigan MAT	1993	discontinued	ICP-SFMS	reverse Nier-Johnson
Plasmatrace II	VG Elemental	1994	discontinued	ICP-SFMS	reverse Nier-Johnson
JMS-Plasmax 2	JEOL	1995	discontinued	ICP-SFMS	reverse Nier-Johnson
Nu Plasma	Nu Instruments	1997	discontinued	MC-ICP-SFMS	Nier-Johnson
Axiom	VG Elemental	1998	discontinued	ICP-SFMS	Nier-Johnson
Axiom MC	VG Elemental	1998	discontinued	MC-ICP-SFMS	Nier-Johnson
Element 2	Thermo Quest	1998	available	ICP-SFMS	reverse Nier-Johnson
Nu Plasma 1700	Nu Instruments	1999	available	MC-ICP-SFMS	Nier-Johnson
Neptune	Thermo Quest	2000	available	MC-ICP-SFMS	Nier-Johnson
IsoProbe-P	GV Instruments	2004	discontinued	MC-ICP-SFMS	magnetic sector + hexapole collision cell
Element XR	Thermo Electron	2004	available	ICP-SFMS	reverse Nier-Johnson
AttoM	Nu Instruments	2004	available	ICP-SFMS	Nier-Johnson
Element GD	Thermo Electron	2005	available	GD-SFMS	reverse Nier-Johnson
SPECTRO MS	Spectro Analytical Instruments	2010	available	MC-ICP-SFMS	Mattauch-Herzog
Nu Plasma II	Nu Instruments	2010	available	MC-ICP-SFMS	Nier-Johnson
Astrum	Nu Instruments	2010	available	GD-SFMS	Nier-Johnson
Neptune plus	Thermo Scientific	2009	available	MC-ICP-SFMS	Nier-Johnson

[a]Manufacturer names are according to their names when the instrument was introduced.

supply is given by a radio-frequency (rf) generator, that ranges typically between 1 and 1.5 kW, at a frequency of about 27 MHz. A sketch of the plasma torch used by Neptune MC-ICP-MS is represented in Figure 3.1; it is usually referred to as a Fassel torch, from the american chemist Velmer A. Fassel. The following treatise, which aims to give an overall description of the torch, is mainly based on the publications by Fassel [5] and Houk [12], while a detailed nomeclature description of the system can be found elsewhere [7].

To form a stable plasma, a pattern of three Argon flows is needed; so the Fassel torch consists of three concentric quartz or fused silicate glass tubes, carriyng a total Argon flow between 11 and 18 L/min. Since the plasma temperature is so high, a thermal insulation is needed; the outer tube main operation is thus to insulate the device from the outside environment. To this aim, the Reed's vortex stabilization technique is used [5]: a flow of Argon tangentially introduced streams upward, cooling the inside walls of the outermost quartz tube and centering the plasma radially in the tube. The outer tube has a 2.5 cm diameter and carries a plasma flow between 10 and 15 L/min; it is also responsible for the main supply of Ar to the plasma. The middle tube provides the auxiliary gas ($0.5 - 2$ L/min), whose role is to lift the plasma off the injector. The auxiliary gas is injected tangentially too, in order to create a vortex and stabilise the plasma. The effect of the previous two tubes is to generate a stable toroidal plasma through the centre tube, in which the sample aerosol is injected. The Argon ionization is started by a spark produced by a Tesla coil; the ions and electrons this way formed interact with the floating magnetic field given by the load coil. The result is a high frequency oscillating electron and ion current, which heats the plasma gas to high temperatures: gas-kinetic temperature of $5000 - 8000$ K, ionization temperature of about 7500 K, excitation temperature of $6500 - 7000$ K, and electron temperature of about 10000 K; then plasma is maintained by inductive heating.

The aerosol generated from the sample is either created by nebulization of a liquid sample solution or consists of solid particles carried by a gas flow when sample material is ablated by a laser; it is then transferred into the centre of the plasma by an Argon gas flow ($0.8 - 1$ L/min), through the inner tube. To be effectively atomized and excited, the sample aerosols should remain localized in the interior high-temperature environment of the plasma as long as possible. The sample species employ about 2 ms to reach the observation height of 15 to 20 mm above the load coil (ALC); this time is sufficient in an environment with such a temperature (between 5000 K and 8000 K) to give rise to an efficient volatilization and atomization of the sample components and subsequent excitation and ionization of the atoms thus formed [5].[2]

The Saha-Eggert equation [1] can be used to estimate the efficiency of

[2]Just for a comparison, the residence times and temperatures experienced by the sample are approximately twice those found in the hottest combustion flames common used in AAS [5].

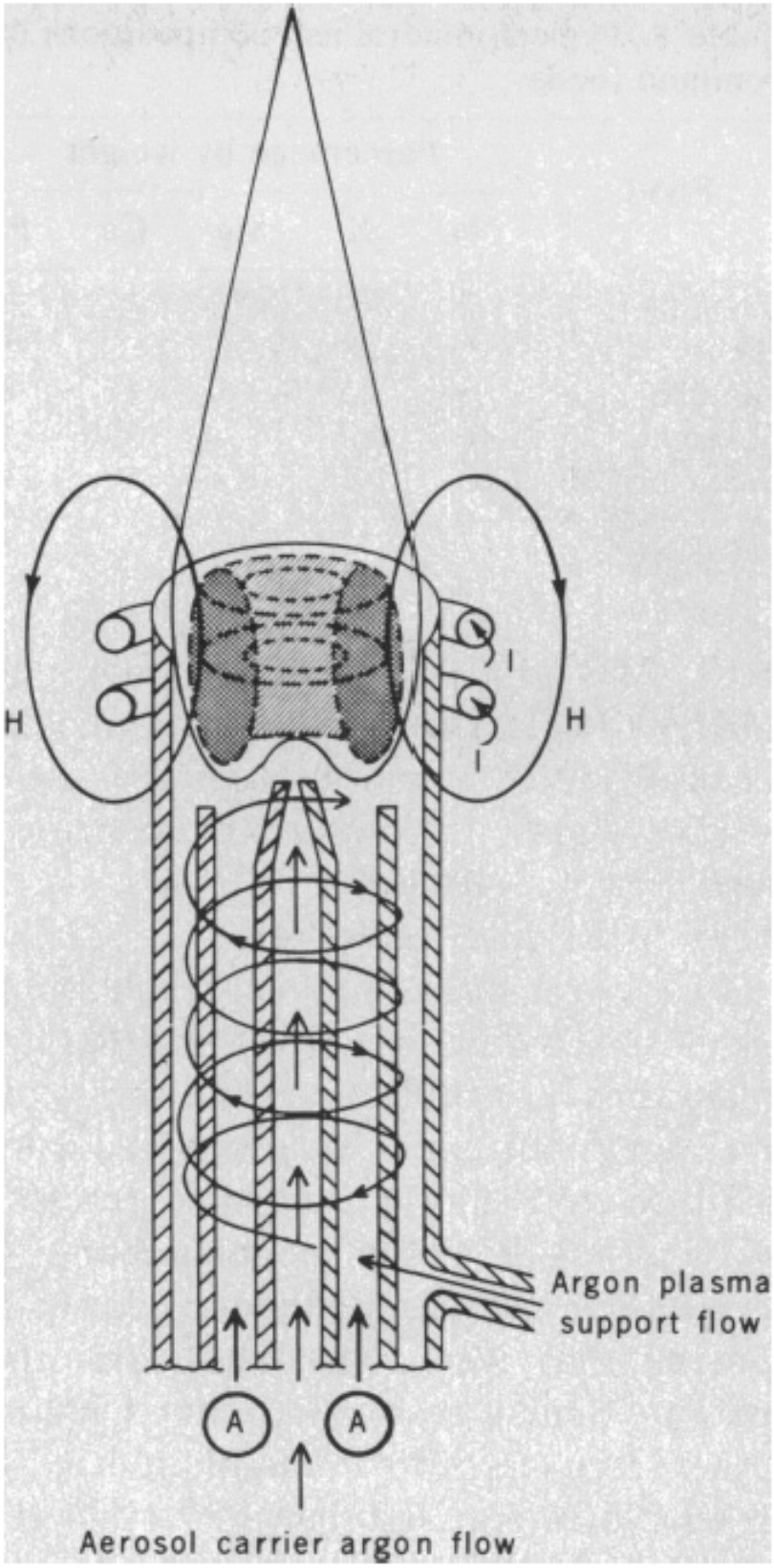

Figure 3.1: Inductively Coupled Plasma configuration [5].

the ionization for the resulting analyte atoms, using the electron densities and temperatures typical for the ICP discharge: it results that all elements with first ionization potentials below 8 eV are completely ($> 90\%$) ionized and even elements with first ionization potentials between 8 and 12 eV are ionized by more than 10% [41]. So the plasma source ionization efficiency is much higher for the ICP than for the other devices;[3] moreover, referring to atomic spectroscopy, it is also economically convenient.[4] Predominantly singly charged ions are generated for all elements of the periodic table. Thus, the mass spectrum observed mainly consists of signals corresponding to the singly charged elemental ions of the nuclides of all elements present in the sample.

ICP sources had been developed for optical spectroscopy; when they were adapted for mass spectrometry, secondary discharges (called "pinches" or "pinch effects") between the plasma and the sampler arose. They were caused by the rf potential in the plasma and they gave rise to numerous deleterious effects: rapid deterioration of the sampling and the skimming cones, contamination of the plasma with sampler and skimmer material, high photon noise and high ion energies with large energy spreads [31]. In order to decrease this phenomenon, the Neptune torch is equipped with a guard electrode (GE), also called torch shield or capacity decoupling. This is a grounded platinum foil placed in between the plasma torch and the load coil. Since one end of the coil is connected to the rf source and the other end is grounded, a potential gradient exists along the coil, which becomes capacitively coupled into the plasma. The plasma, in turn, is electrically coupled through the sheath (see chapter 4) to the sampler. These two impedance sources act as a potential divider; if plasma potential is too high a strong secondary discharge forms between the plasma and the sampling orifice [29]. Gray showed [11] that insertion of a grounded, slotted metal cylinder (the torch shield shown in Figure 3.2) between the load coil and the outer wall of the torch shields the d.c. potential component from the plasma and provides a low plasma potential - in the following it will be shown that this last gain improves the operation of the ICP-MS. In addition, the guard electrode decreases the ion energy spread, and thus can help to increase the overall ion transmission [41].

In order to minimize the plasma potential and secondary discharge, mainly two other different load coil configurations have been used:[5]

- inverted (or reversed) load coil: the load coil is grounded at the downstream end nearest the sampler;
- center-tapped load coil: a high voltage of equal amplitude but opposite phase is applied to the coil edges, while the center is connected to ground.

[3] In the Thermal Ionization Mass Spectrometry is lower than 5%.

[4] The operating cost of these plasmas flowing in the Fassel torch, exclusive of the electrical power, is lower than the cost of the gases needed to operate the nitrous oxide-acetylene flame commonly used in Atomic Absorption Spectroscpy (AAS).

[5] Also the interleaved and the balanced load coils have been studied [31].

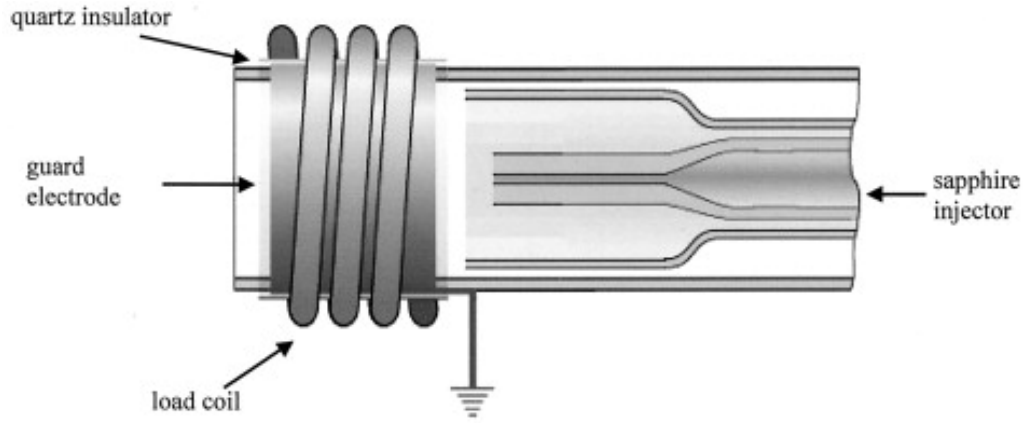

Figure 3.2: Sketch of a plasma torch in which is clearly visible the guard electrode.

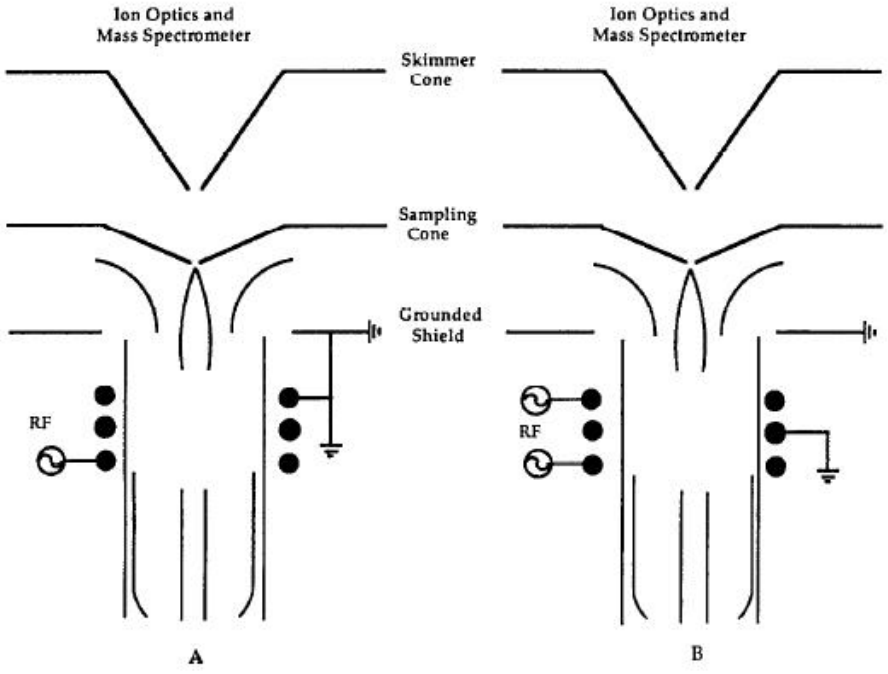

Figure 3.3: Design features of an inverted load-coil (A) and a center-tapped coil (B) [20].

Chapter 4

Extraction interface

In coupling an Inductively Coupled Plasma and a Mass Spectrometer, the trouble is that ICP operates at atmospheric pressure, whereas MS requires an ultra high vacuum (UHV) condition (operating pressure less then 10^{-7} Pa), otherwise the ions would be scattered by the gas atoms. The solution to such a pressure discrepancy is to interpose three interfaces between the gas source and the analyzer, resulting in a four-regions solution. While the first one is at ambient pressure (10^5 Pa), the second region (called interface) is pumped by a regular rotary pump, to obtain a pressure of $2 \cdot 10^2$ Pa. The higher is the grade of vacuum, the better are the instrumental performances features, such as transmission efficiency or abundance sensitivity; as a consequence, stronger vacuum pumps are becoming popular. To preserve the high vacuum condition in the third region, a slide valve is interposed; it is only opened when the plasma is operating stable and is closed before plasma shutdown, to isolate the high vacuum. The third region, where lenses are located, has a pressure of about $5 \cdot 10^{-2}$ Pa, while the mass spectrometer (final region) operates in ultra high vacuum conditions (about 10^{-7} Pa). It has been found that such a low pressure is advantageous in the case of multi collector devices [41]; in order to provide this result, the analyzer is separated from the lens system by a second valve and additional ion getter pumps are required.

The development and improvement of the ion sampling interface for ICP-MS have been crucial aspects of the success of the technique.
The first analytical mass spectrometer for ion sampling from an ICP used a stagnant layer type sampling interface [6] [10][1]. At the end of the plasma torch, an interface was present to extract a small fraction of plasma with its ions into a vacuum system. This interface was composed by two cones, a sampler and a skimmer. The first one consisted of a water-cooled copper cone, on whose tip was mounted a molybdenum disk, through whose center was drilled a 50 µm diameter orifice. Due to this small diameter, an aerodynamically stagnant layer of gas formed between the two cones, as shown in Figure 4.1.

[1]This type of pinhole sampler was adopted in the early days from flame and plasma sampling methodology and from the original work of Gray with a d.c. capillary arc plasma [6].

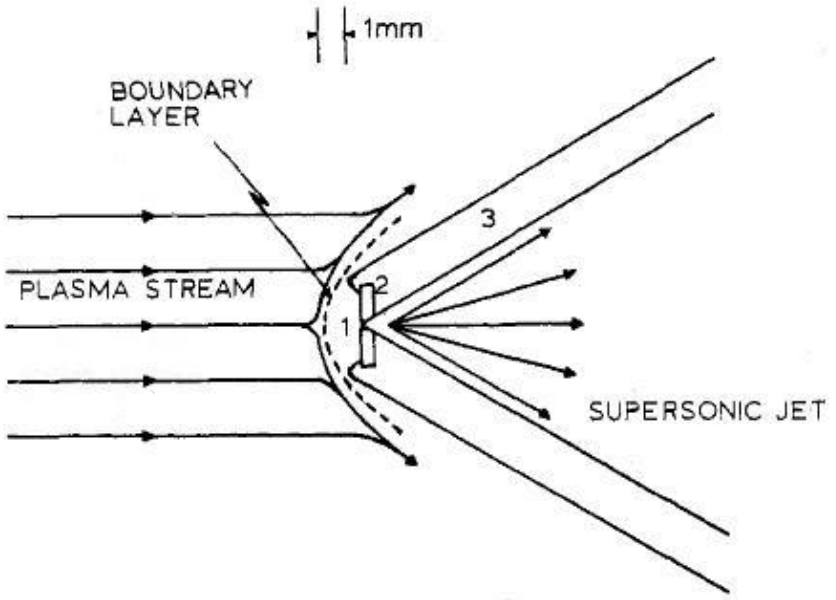

Figure 4.1: Diagram of boundary layer sampling interface for ICP-MS [10].

Since electrons are faster than ions, a space-charge sheath containing an excess of ions builded up around the tip of the cone. This stagnant boundary layer was in thermal contact with the relatively cool sampler, making the layer temperature intermediate between the plasma one and the sampler one. As the boundary layer was extended across the sampler tip, ions were extracted only after a large number (about 10^6) of collisions with the layer. This transport through the boundary layer induced several liabilities: first of all it was probably facilitating ion-electron recombination, ion neutralization at the sampler walls, charge exchange, ion-neutral attachment, nucleation and condensation of solid deposits (mainly due to the formation of involatile metal compounds) and some occurring reactions might have been catalyzed by the metal surface of the orifice disk. Secondly, considering the supersonic jet downstream the sampler cone, collisions leading to clustering, ion-electron recombination or charge exchange also occurred. Consequently, sample deposition occurred in the sampling orifice - metal oxide and metal hydroxide ions had been observed. Progressive solid condensation of sample material both made the extraction efficiency of analyte ions gradual decreasing and restricted the useful life of orifices. Even nowadays the first components that have to be changed in a mass spectrometer are the sampler and the skimmer cones: their lifetime is limited by the sputtering in the region immediately behind the aperture [8]. Back to the problem of solid deposition, with this configuration biological fluids required a dilution factor of several hundred before analyses of such solutions could be performed for more than one hour. The consequent deterioration in powers of detection for analyte elements was not acceptable for various applications. Owing to the difficulties arised with this type of sampling, a new

sampling interface has been adopted: the supersonic nozzle and skimmer [10].[2]

The version of this technique used in our ICP-MS consists of a large sampling orifice: with this configuration it is possible to break through the intermediate sheath and to have a continuum gas flow condition. The sheath is a thin ply around the inner edge of the sampling orifice; in this ply the charged particles shield the rest of the gas flow from the potential on the sampler (usually grounded). Therefore the extracted flow passes through the sampler as a quasineutral plasma,[3] i.e. with essentially equal densities of ions and electrons.[4] Cool layers are still present, but they form obliquely around the inside edge of the orifice, instead of across its mouth [29]. Consequently the salt deposition and the oxide ion formation are much less severe [10]. So, this configuration provides several advantages:

- a much higher total flow of ions;
- a more representative sample of ions from the plasma;
- greater resistance to plugging from deposited solids.

The improved resistance to erosion and expansion is also because such an orifice is made with relatively thick metal near the tip.

Figure 4.2 is a scale drawing of continuum sampling interface. The sampler (or nozzle) (A) is a nickel-made cone, in which tip is drilled a 0.8 mm diameter orifice with a length of 0.25 mm. The internal and external sampler angles are 90° and 120°, respectively. Coaxially placed, 7 mm downstream the sampler, there is the skimmer, made from stainless steel with 50° and 60° internal and external angles, respectively.[5] The short distance between the two cones allows a sequential pressure decrease and it could be varied by changing the thickness of the Teflon spacer (C). Both the sampler and skimmer are grounded; nevertheless there could be some benefits applying a voltage to the skimmer - see section 7.

From the work by Hu et al. [22] it results that larger sampling orifices could bring higher ion signals: the plot in Figure 4.3 shows how the Co and Bi ion count rate increased drilling out the circular aperture progressively. Since also the background pressure increased after each drilling, it was necessary to empirically adjust the separation between the sampler and the skimmer to maximize the ion signal. Moreover, a small orifice is more subjected to clogging compared to a bigger one: as it can be seen in Figure 4.4 a pressure decreasing in the case of the smaller orifice is observed, since it plugs quickly. In conclusion, enlarging the orifice could provide a double

[2]This type of sampling interface have been in use since the pioneering work of Kantrowitz and Grey in 1951 [2].

[3]The charge density is considered to be sufficiently high as to ensure that the characteristic Debye length is small with respect to the dimensions of the interface components - under this condition it's possible to consider the beam as neutral.

[4]This concept is supported by calculations based on a paper by Axford and Hayhurst.

[5]Nowadays, different skimmer cone designs are available, characterized by different transmission efficiency [44].

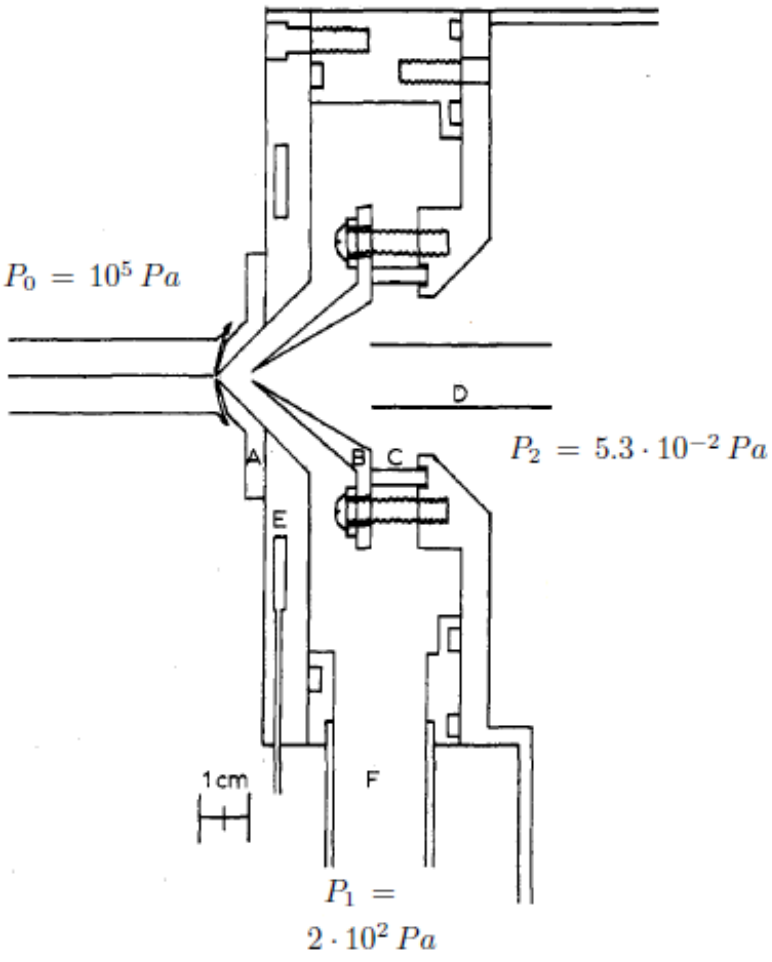

Figure 4.2: Scale drawing of continuum sampling interface for ICP-MS [10].

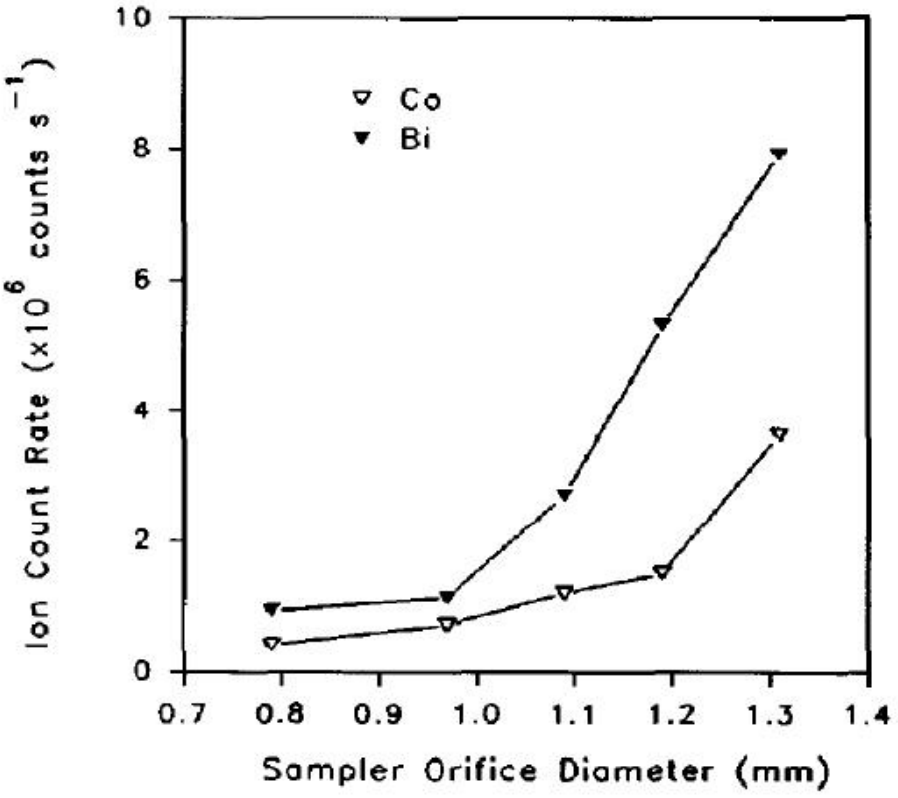

Figure 4.3: Ion count rates as a function of sampler orifice diameter [22].

benefit: a higher ion signal and an improved tolerance to orifice plugging. However it has to be underlined that these studies were conducted with a continuous flow ultrasonic nebulizer, which transported material to the plasma at a rate at least 10 times greater than the one obtained with a conventional pneumatic nebulizer. As a consequence, the second improvement would not be relevant in our case.

In order to understand the performance of this interface and particularly to find the parameters needed in the simulations (see section 6.4) the gas flow (in molecules/s) through the sampler can be calculated through equation (4.1) [9] used by Olivares and Houk in their article (dating 1985):

$$U_0 = \frac{\pi f(\gamma) N_A D_0^2 P_0}{4\sqrt{mRT_0}} \tag{4.1}$$

where $f(\gamma) = \sqrt{\gamma} \cdot [2/(\gamma+1)]^{(\gamma+1)/2(\gamma-1)}$, N_A is Avogadro's number, D_0 the orifice diameter, P_0 the ICP pressure, m the mean molecular weight of Argon, R the gas constant, T_0 the source gas temperature of the ICP, and γ is the specific heat ratio at constant pressure and volume (C_p/C_v) of Argon.

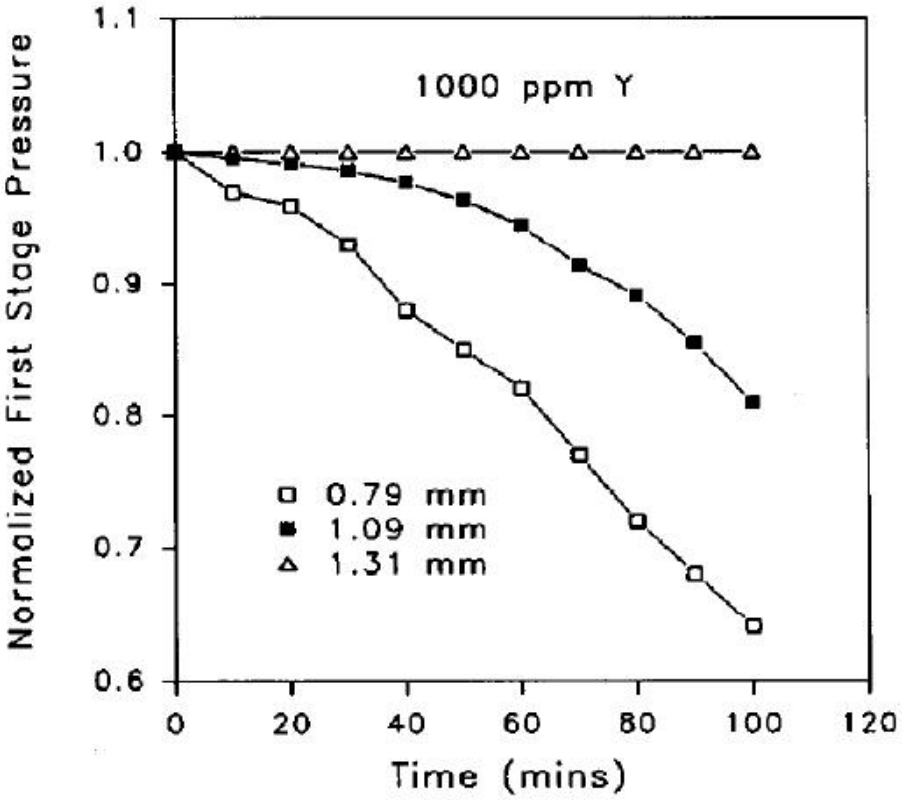

Figure 4.4: Normalized interface pressure as a function of time for continuous nebulization of 1000 ppm Y at sampling orifice [22].

The flow through the skimmer cone is given by the following equation:

$$U_S = U_0 \cdot f(\gamma) \left(\frac{D_S}{X_S} \right)^2 \tag{4.2}$$

where D_S is the skimmer diameter and X_S the skimmer-to-sampler distance. These theoretical results are in good agreement with the experimentally obtained values for an ICP with 10 mg/l Co solution [10]. In a 1988 article, Douglas and French provided another way to describe the gas expansion through these two orifices; in their article the gas flow across the sampler was given by [47]

$$G_0 = 0.445\, n_0\, a_0\, D_0^2 \tag{4.3}$$

where n_0 is the source number density and a_0 the speed of sound in the source:

$$a_0 = \frac{\gamma\, k\, T_0}{m} \tag{4.4}$$

(k is the Boltzmann's constant). The equation for the gas flow through the skimmer uses the gas density and the flow velocity at the skimmer tip, $n(x_S)$ and $v(x_S)$ respectively, and the area of the skimmer orifice A_S:[6]

$$G_S = n(x_S)\, v(x_S)\, A_S \tag{4.5}$$

These two models (the one by Olivares and Houk and the one by Douglas and French) are based on a common assumption: as the plasma plume is expanding from a sonic orifice into a region of lower pressure, it produces the development of the free jet shock wave system [4]. As it can be seen in the cross sectional view showed in Figure 4.5, the flow field consists of a dark core portion, named "zone of silence" (unaffected by the pressure changes along the jet boundary), laterally bounded from a barrel shock and ending with the so called Mach disk (its thickness has been found to be of the order of magnitude of the mean free path [34]).

This phenomenon has been well characterised by Ashkenas and Sherman [3]; they calculated the distance downstream the sampler at which the Mach disk forms:

$$x_M = 0.67 D_0 \cdot \sqrt{P_0/P_1} \tag{4.6}$$

where P_1 is the interface background pressure. This relationship has been confirmed experimentally by optical measurements of emission excited in the Mach disk [29].

As the gas passes through the sampler, it expands adiabatically into the low pressure region; since the mean free path (λ) is much smaller than the diameter orifice, several collisions between fast atoms from the dark core and background atoms occur. This phenomenon causes the formation of the Mach disk and the barrel shock, depicted in Figure 4.5. Moreover, through

[6] The flow velocity is nearly constant at $\sqrt{5kT_0/2m}$.

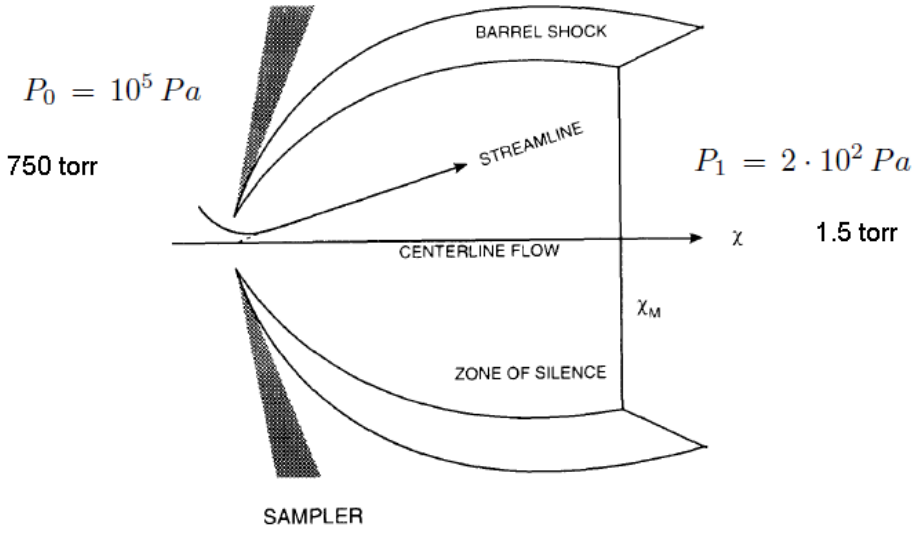

Figure 4.5: Cross sectional view of supersonic expansion behind the sampler [29].

this scattering process, the random thermal motion of atoms in the plasma is converted into directed motion in the zone of silence: the flow velocity can than exceed the local speed of sound and the Mach number becomes greater than one ($M > 1$).[7]

The Mach disk formation is observable analyzing atom velocities and temperatures (showed in Figures 4.6 and 4.7) as a function of distance downstream the sampler cone. The rapid acceleration and cooling of the atoms are expected from a supersonic expansion [34] and is represented by the series of point that start about 2 mm downstream the sampler. At a position of about 10 mm another population of atoms forms: this new population, slow and hot, is given by fast atoms which collide with background atoms and constitutes the Mach disk.

In order to find a numerical result for the gas flow through both the sampler and the skimmer using the two models previously shown, some other relations are needed. The Mach number in the plasma is less than one ($M < 1$); as the gas passes through the sampler the density decreases, the flow speed increases and M increases too. In this region the centerline Mach number for a monoatomic gas - as in this case - is given to a very good approximation by

$$M = 3.26(x/D_0)^{2/3} - 0.61(x/D_0)^{-2/3} \tag{4.7}$$

where x is the axial distance behind the orifice. This means the Mach number reaches 1 at a distance equal to 0.5 orifice diameters downstream

[7] The Mach number is defined as the ratio between between the gas flow speed (u) and the local speed of sound (a_0).

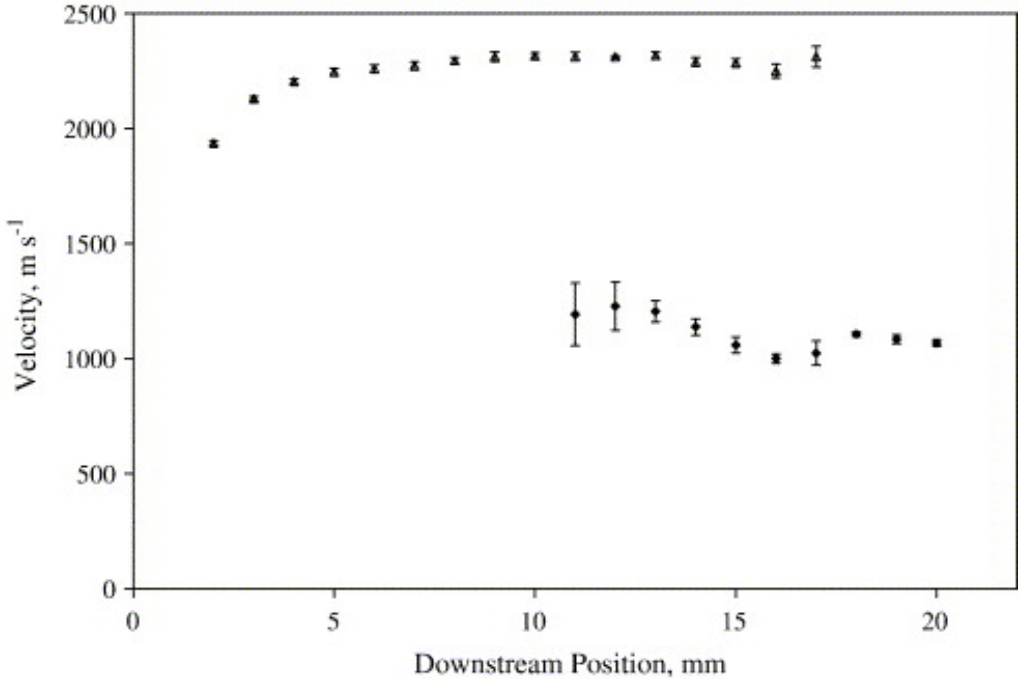

Figure 4.6: Axial velocity dependence downstream from the sampler cone: △ fast, cold component, ⋄ slow, hot component [34].

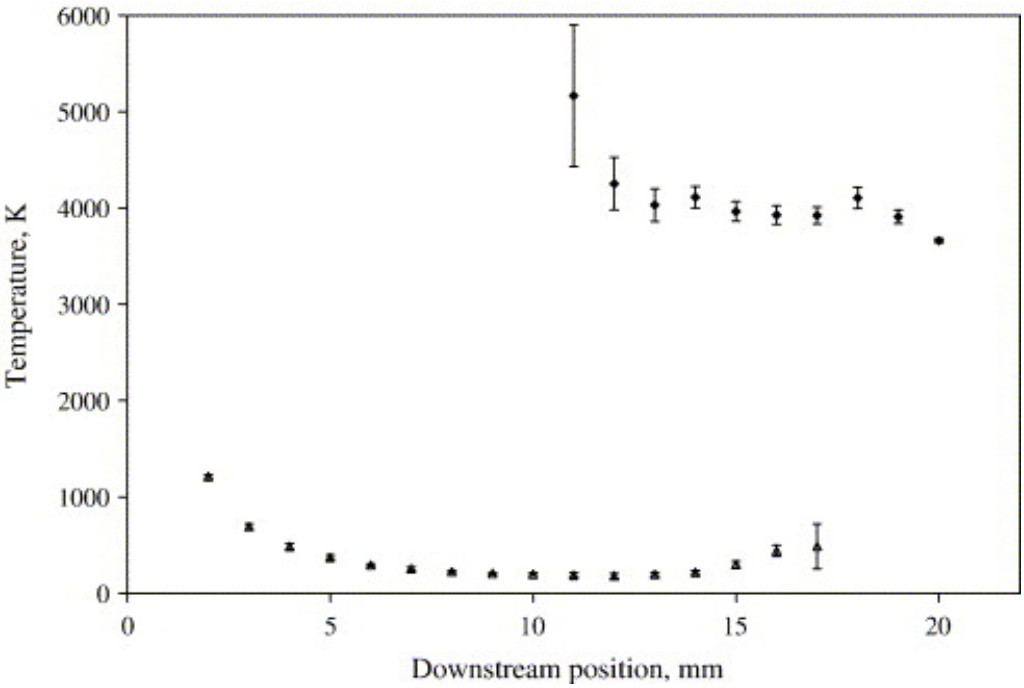

Figure 4.7: Axial temperature dependence downstream from the sampler cone: △ fast, cold component, ⋄ slow, hot component [34].

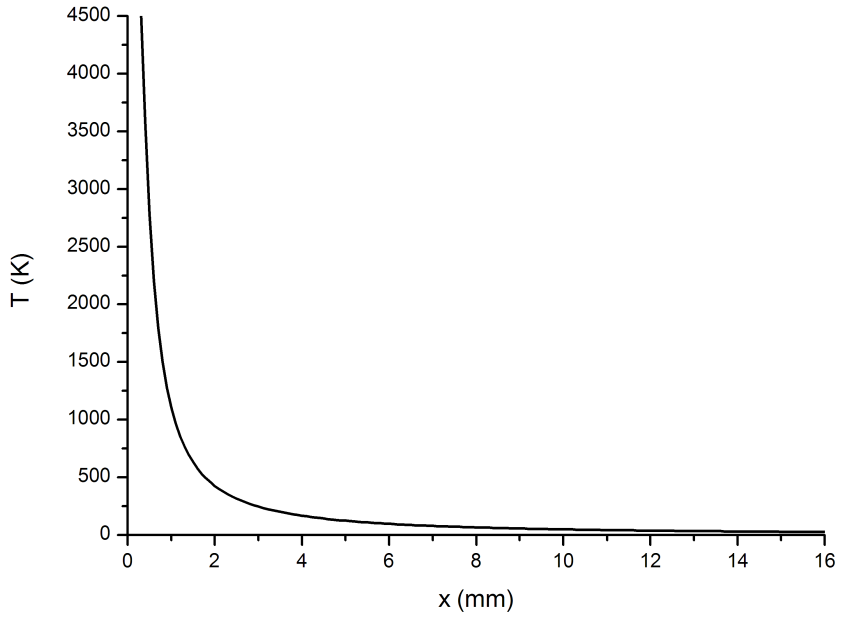

Figure 4.8: Scatter plot of the gas temperature as a function of the distance from the sampler in the free jet, obtained from equation (4.9).

the sampler. Furthermore the gas density and temperature decrease inside the jet, according to the following equations:

$$\frac{n_0}{n} = \left[1 + M^2 \frac{\gamma - 1}{2}\right]^{1/(\gamma-1)} \tag{4.8}$$

$$\frac{T_0}{T} = 1 + M^2 \frac{\gamma - 1}{2} \tag{4.9}$$

where n_0 and T_0 are the gas density and temperature in the source. Equation (4.8) could be approximated back to the onset of the Mach disk by

$$n(x) = 0.161\, n_0\, (D_0/x)^2 \tag{4.10}$$

This relation, that describes the drop in intensity of neutral species along the centerline, has been experimentally confirmed by Niu and Houk, when in 1994 they measured electron densities in the interface with a Langmuir probe [27].

The plot in Figure 4.8 represents the temperature drop described by equation (4.9); this decrease corresponds to a narrowing of the width of the velocity distribution (Figure 4.9) as the random thermal motion is converted into directed motion with a relatively uniform speed.

A combination of all the displayed equations have been used to obtained the results highlighted in Table 4.1.

The gas flows have been obtained with two different equations and are in good agreement, especially in correspondence of the sampler cone. In

Table 4.1: Parameters and constants used to calculate the gas flow - highlighted - through both the sampler and the skimmer with two different models.

Olivares and Houk [10]				Douglas and French [14]			
γ	1.67		specific heat ratio C_p/C_v	γ	1.67		specific heat ratio C_p/C_v
$f(\gamma)$	0.726661			T_0	5000	K	gas temperature
D_{sa}	0.8	mm	sampler diameter	m	$6.6 \cdot 10^{23}$	g	relative atomic mass
P_0	10^5	Pa	ICP pressure	D_{sa}	0.8	mm	sampler diameter
M	39.9	g/mol	relative molecular weight	a_0	1317.97	m/s	speed of sound in the source
T_0	5000	K	gas temperature	n_0	$1.5 \cdot 10^{18}$	cm^{-3}	source density
				x	7	mm	sampler to skimmer distance
U_0	$5.4 \cdot 10^{20}$	atoms/s	gas flow through the sampler	G_0	$5.6 \cdot 10^{20}$	atoms/s	gas flow through the sampler
D_{sk}	0.8	mm	skimmer diameter	M_{sk}	14		Mach number at the skimmer
x	7	mm	sampler to skimmer distance	n_{sk}	$3.0 \cdot 10^{15}$	cm^{-3}	gas density at the skimmer
P_i	861	Pa	impact pressure at the skimmer	v	$1.6 \cdot 10^5$	cm/s	flow velocity
				D_{sk}	0.8	mm	skimmer diameter
U_S	$5.1 \cdot 10^{18}$	atoms/s	gas flow through the skimmer	G_S	$2.5 \cdot 10^{18}$	atoms/s	gas flow through the skimmer

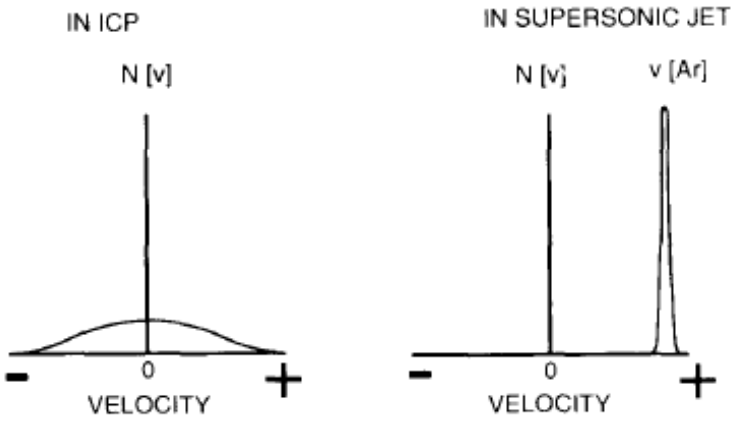

Figure 4.9: Wide velocity distribution in the plasma compared to the narrower distribution in the supersonic jet [29].

the region close to the skimmer there is a factor 2 between the two models results; this difference is negligible since the gas flow probably depends on many other contributions - e.g. the analyte species, the nebulizer gas flow - that can significantly affect the final result.

Regarding the sampler to skimmer distance, Douglas and French showed that the best arrangement corresponds to having the skimmer tip about 2/3 of the way back to the onset of the Mach disk [14] [29]. This result approximately agrees with the one obtained for the maximum intensity in the case of a neutral beam from Campargue expansion [29]:

$$X_S = 0.125\, D_0 \left[\frac{D_0 P_0}{\lambda P_1}\right]^{1/3} \tag{4.11}$$

Even if here λ is referred to as the mean free path inside the sampler orifice, it has no particular subscript as it is expected to be nearly equal to the one for the gas outside the sampler in the ICP.

The skimmer protrudes into the zone of silence so that shock waves form behind the skimmer tip off the outside walls of the skimmer, as shown in the sketch in Figure 4.10. With this configuration, the metal wall of the skimmer where the second shock wave begins is thick enough to conduct away the heat generated and the thin edge of metal at the skimmer tip remains stable. Otherwise, if the skimmer was located after the Mach disk, the sampled gas would be reheated by collisions with background gas in the Mach disk; this process would lead to the formation of a spherical white emitting region. The heat this way producted would be directly transferred to the skimmer tip, too thin to properly conduct the heat away; the result would be the melting or the rapid degradation of the skimmer tip [29].

Calculation of the Knudsen number Kn, especially at the skimmer, is also instructive; it is defined as the ratio of the mean free path λ to the

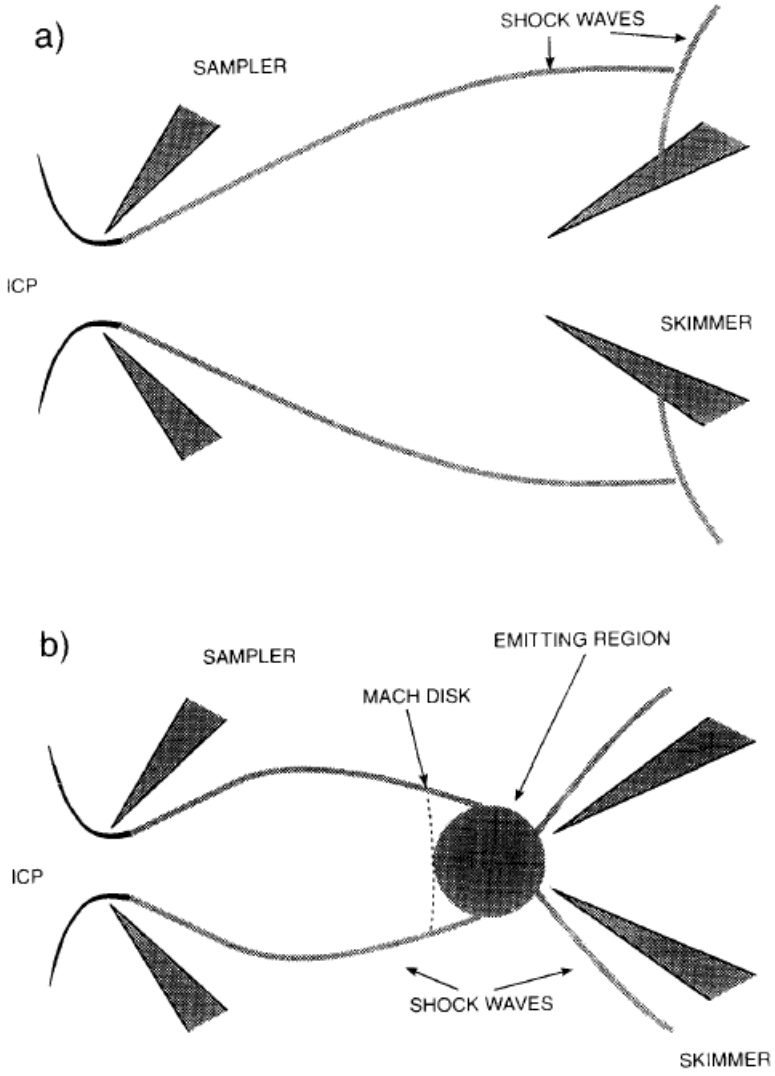

Figure 4.10: Effect of different sampler-skimmer distances. (a) Skimmer at normal position used for analysis. (b) Skimmer outside the zone of silence [29].

skimmer diameter D_S:

$$Kn = \frac{\lambda}{D_S} \tag{4.12}$$

In the small scale Kn quantifies the failure of the Navier-Stokes description: in fact this model corresponds to the collision-dominated transport limit of small Knudsen number $Kn \ll 1$. More specifically, in the presence of hydrodynamic gradients in a homogeneous gas over lenghtscales characterized by $Kn \ll 1$, the Chapman-Enskog expansion procedure can be applied to the governing kinetic (Boltzmann) equation to show that the gas response can be described by linear-gradient constitutive relations which lead to the Navier-Stokes description [33]. Practically, the lower the Kn, the smaller the number of collisions is; Kn would have to be much less than unity (i.e. $\lambda \ll D_S$) for the beam to expand through the skimmer without collisions. The mean free path λ can be expressed through the following relation, based on viscosity measurements and kinetic theory arguments [47]:

$$\lambda = \frac{16/5\,\mu}{nm\sqrt{\frac{2\pi kT}{m}}} = \frac{16/5\,\mu}{n\sqrt{2\pi kTm}} \tag{4.13}$$

where n is the molecular number density, m the particle mass and k the Boltzmann's constant. It is possible to refer to the viscosity coefficient both with μ and η. Niu and Houk report another relation for the Knudsen number:

$$Kn = \frac{\lambda}{D_S} = \frac{1}{1.414\pi\sigma n D_S} \tag{4.14}$$

where σ is the gas kinetic cross section for Ar ($4.1 \cdot 10^{-15}$ cm^2). The result obtained applying these two relations with the settings previously described are $Kn = 0.3$ and $\lambda = 0.2$. These values are consistent with several articles [10] [14] [26] [29]. The literature concerning supersonic expansions indicates that in this case two main disturbances are to be expected around the tip [26]: a thin shock in front of the skimmer and perturbation of the straight line beam flow by collisions of the beam with atoms reflected from the skimmer wall.

Considering now the gas flow rate calculated for our particular case, theoretically the total ion current at the base of the skimmer should be about 0.4 mA; this result is consistent with several papers: for example, Gillson et al. [15], even if with a slightly different setting, calculated an ion current of 10^{16} ions/second, corresponding to 1.5 mA. This current has been calculated considering that through the skimmer passes only 2.6% of the central flow of the ICP. Considering the theoretical loss of analyte ions for Y, Chen and Houk calculated a transmission efficiency from the skimmer to the detector is 0.02%. As a consequence, the overall efficiency of an ICP-MS is about $5 \cdot 10^{-6}$; in other words, theoretically, for every 10^6 analyte ions in the central channel of the ICP, only five ions reach the detector. As it will be explained later, this number is even lower in the reality. Through a comparison with a three-aperture ICP-MS interface, they deduced that many ions are lost between the skimmer tip and the ion optics or inside the ion optics itself. So

it is crucial to understand what happens in this region and how ions are lost. Chapter 6 is aimed to simulate the region where particles fly, including the skimmer and the first lens (named extraction lens), in order to study and characterize the formed beam. Resuming the work by Gillson et al., they repeated the ion current measurements[8] with the same settings for a heavier ion (U^+); the flux resulted higher. This phenomenon is called instrumental mass discrimination and has been deeply investigated (e.g., by Kivel et al. [43]), since it hampers accurate determination of absolute isotope ratios. In general, it consists in having at the spectrometer a stoichiometric composition different from the one characterizing the original sample material. It has been reported that, typically, analyzing two isotopes, the heavier has a higher transport efficiency: the difference is about $10 - 20\%$ in the case of light elements and down to 1% for heavy elements. Four main factors are at the base of mass discrimination:

- sample introduction and ion generation;
- collisions;
- space charge effect;
- energy-selective ion transmission.

The first and the last one are not studied in the present work, since it is limited to the region defined by the skimmer and the first ion lens. As the plasma is quasi-neutral until the starting of the skimmer, it's reasonable to assume that mass discrimination in the interface is mainly caused by collisions. This hypothesis is consistent with the work by Taylor and Farnsworth [44]: they found the absence of any space charge effect during the ion transfer from the source to the spectrometer. Moreover, for the present work, collisions have been considered a negligible contribution compared to space charge effect. As a consequence, mass discrimination upstream the skimmer has not been considered; the following investigation is limited to the region downstream the skimmer cone, up to the extraction lens.[9] Resuming mass discrimination due to space charge effects, it can be explained by postulating that the ion beam within the skimmer is space charge limited: its density is so high that mutual repulsion will not allow the ions to remain tightly focused. Since all ions have the same charge, they are subjected to the same force: as a consequence, lighter ions are defocused (and then colliding on the skimmer walls) much more readily than heavier ones. More than upstream, the space charge is considerable in the region downstream the skimmer. In fact, according to the model by Douglas and French [14], plasma is sampled without significant charge separation.[10]

[8] They used a stainless steel collector - situated 1 in. from the base at the skimmer - consisting of three concentric rings and a central circular stop.

[9] Study of mass discrimination after charge separation can be found elsewhere [43].

[10] In an alternate model, presented by Chambers et al., it is assumed that significant charge separation occurs between the sampler and the skimmer; therefore the ion current through the skimmer would be significantly less than that estimated in this work.

Behind the skimmer, where the beam expands, there are three main contributions to the loss of the ions: the density decreasing - proportionally to $1/x^2$ (where x is the distance from the skimmer) - as a consequence of the expansion, the beam spreading and the preferential loss of electrons. This last phenomenon could be explained considering the Debye length λ_D; downstream of the skimmer λ_D is significant compared to the dimensions of the beam and electrons are lost readily to the inner wall of the skimmer because their high mobility. Moreover, in this stage, the electrostatic field penetration from the extraction lens becomes significant; as a consequence of these two effects, electrons leave a net axial positive space charge [21]. Its significance can be quantitatively described using the perveance P [28]:

$$P = \frac{I}{V^{3/2}} \tag{4.15}$$

where I is the total current and V the accelerating potential. P depends only on the geometry of the extractor and on the type of the particle [28]. For a singly charged ion beam, space charge is negligible if

$$P < 10^{-8} \cdot (m_{ion}/m_e)^{-1/2} \tag{4.16}$$

where m_{ion} and m_e are, respectively, the mass of the particle and of the electron. So, for Argon ions, the maximum perveance without significant space charge effects is $3.7 \cdot 10^{-11}$. In the proximity of the skimmer P is equal to $1.9 \cdot 10^{-7}$ [28], which exceeds the maximum perveance by more than a factor 5000. To obtain a rough estimate for the maximum electron current (for argon), it is possible to assume the skimmer as a cylinder with diameter D and length L:[11]

$$I_{e,max}(A) = 38.6 \cdot 10^{-6} V^{3/2} \left(\frac{D}{L}\right)^2 \tag{4.17}$$

The ion current is related to the electron one:

$$\frac{I_{ion}}{I_e} = \sqrt{\frac{m_e}{m_{ion}}} \tag{4.18}$$

therefore

$$I_{ion,max}(A) = 9.04 \cdot 10^{-7} \sqrt{\frac{z}{m_{ion}}} V^{3/2} \left(\frac{D}{L}\right)^2 \tag{4.19}$$

As hinted before, another cause of losing ions is the rarefaction of the beam as it travels farther from the skimmer tip. The Debye length increasing, by virtue of its inverse square root dependence on the ion density, causes also the ions (not only the electrons) spreading. So, to enhance the transmission efficiency, the distance between the skimmer tip and the ion optics has to be minimized. A substantial increase in ion signal was

[11] The diameter at the base of the skimmer is equal to its length; the average diameter of the skimmer is then about $L/2$ and the ratio D/L is about 0.5.

seen when this separation was reduced to 2.4 cm [22]. At this position, the mouth of the first lens was only 5 mm from the nearest surface of the skimmer wall. Closer separations were tried, but the voltage output for the first lens became unstable, because of an electrical discharge between the ion lens and the skimmer wall or due to a high current flow to the lens. In the Neptune MC-ICP-MS is the thickness of the separation valve limits the smaller distance between the skimmer and the lens.

Table 4.2: Resume of the torch and the extraction interface operating parameters

Forward power	1350 W
Guard electrode	Grounded
Gas flows:	
Cool	14.6 L/min
Auxiliary	0.9 L/min
Sample	0.8 L/min
Make-up	$0.3 - 0.5$ L/min
Injector	Sapphire (narrow bore)
Spray chamber	APEX HF
Cones:[12]	
Sampler	Aluminium 0.9 mm
Skimmer	Aluminium 1.0 mm

[12]Custom design by PSI.

Chapter 5

IBSimu

To simulate what happens during the beam extraction from the plasma source, an ion optical computer simulation package have been used, IBSimu. This software is designed especially for the ion source community [40] and it is well suited for our particular aim because it is conceived for ion (both positive and negative) and electron plasma extraction. Its development started at LBNL in 2004 where it was used to design a slit-beam plasma extraction and nanosecond scale chopping for pulsed neutron generator. Later, at the University of Jyväskylä (Finland), Department of Physics (JYFL), the code was made modular and suitable for many different types of problems. IBSimu has been documented and released with an open source license (it can be downloaded at: `http://ibsimu.sourceforge.net/`) and so it's well suited for use in the scientific community. It is used as a computer library through a C++ interface and it presents several peculiar advantages:

- power and versatility;
- customization and inclusion of new modules;
- automation and batch processing;
- incorporation of code in other software;
- easiness of use (on the main site there are two tutorials `http://ibsimu.sourceforge.net/tutorial.html` and the reference manual `http://ibsimu.sourceforge.net/manual_1_0_5new_solver/index.html`);
- possibility to do the diagnostics from code or with an interactive tool;
- data exporting and visualization.

The code is capable of solving electric fields in 1D, 2D (planar or cylindrical symmetry) or full 3D simulation geometries and it can calculate relativistic continuous wave or pulsed particle trajectories taking into account the space charge density. The starting point is the definition of the geometry, where the simulation is done, and the electrodes (including the

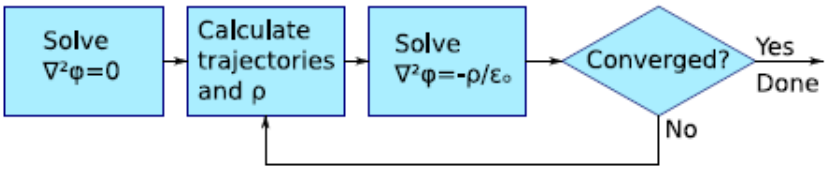

Figure 5.1: Operational diagram for solving the Poisson problem[40].

grounded interfaces), using a mathematical description. In order to calculate the electric potential, the simulation domain is divided in square meshes with constant step size, which dimension can be specified in the geometry section of the code. So the field where particles fly is discretized: for each cell the Poisson's equation

$$\nabla^2\phi = -\frac{\rho}{\epsilon_0} \tag{5.1}$$

is solved using finite difference method (FDM) on the nodes of the mesh.

Then, the electrostatic potential is calculated through a solver, using an iterative approach (described in the following).

The finite difference representation for a vacuum node i is:

$$\frac{\phi_{i-1} - 2\phi_i + \phi_{i+1}}{h^2} = -\frac{\rho_i}{\epsilon_0} \tag{5.2}$$

while Neumann (5.3) or Dirichlet (5.4) boundary conditions can be used for boundary nodes.

$$\frac{-3\phi_i + 4\phi_{i+1} - \phi_{i+2}}{2h} = \frac{d\phi}{dx} \tag{5.3}$$

$$\phi_i = \phi_{const} \tag{5.4}$$

To achieve smooth electric fields on the solid edges, the edge nodes within the solids are adjusted to virtual potentials using subnode information about the geometry:

$$\frac{\beta\phi(x_0 - \alpha h) - (\alpha+\beta)\phi(x_0) + \alpha\phi(x_0 + \beta h)}{\frac{1}{2}(\alpha+\beta)\alpha\beta h^2} = -\frac{\rho(x_0)}{\epsilon_0} \tag{5.5}$$

On the edges of the simulation domain, every solver supports Dirichlet and Neumann (first and second order approximations) boundary conditions. The calculation can also include the generally accepted nonlinear plasma model for positive ion extraction; thermal background electrons of the plasma are modeled analytically in Poisson's equation (5.1) where $\rho = \rho_{ion} - \rho_{e0}\, exp[(U - U_\mathrm{p})/(kT_\mathrm{e}/e)]$ and the plasma potential U_p and the electron temperature T_e are the model parameters. Ion charge density ρ_{ion} is calculated from beam current density and electron charge density ρ_{e0} is set to ρ_{ion} at plasma potential. The electric field (needed for particle

trajectories) is obtained by numerical differentiation and interpolation of potential, using nine closest neighboring mesh nodes. Then, the code calculates the particles trajectory integrating the equations of motion, derived from Lorentz force, with adaptive Runge-Kutta Cash-Karp (fourth and fifth order) algorithm. In 2D and with a null magnetic field:

$$\begin{aligned}
\frac{dx}{dt} &= v_x \\
\frac{dy}{dt} &= v_y \\
\frac{dv_x}{dt} &= a_x = \frac{q}{m} E_x \\
\frac{dv_y}{dt} &= a_y = \frac{q}{m} E_y
\end{aligned}$$

This method has an automatic step-size adjustment for required trajectory accuracy. The implementation of the Runge-Kutta algorithm is used from the GNU Scientific Library. As the CPU available was multicore and the particle tracer is multithreaded, for a high efficiency calculation eleven cores were used for flying particles and one for the potential determination. The particle tracer algorithm finds all the meshes the trajectory passes through and deposits the charge of the particle on the four (eight in 3D) surrounding mesh nodes. The same procedure checks for collisions in the mesh square.

The code in Appendix A was the starting point in my work; to understand the extraction process and to optimize the fundamental parameters (U_p and T_e), I changed some parts of it, as it will be explained in the next chapter.

Hereinafter there is a description of the main operations done by this first code. After including all libraries needed (most of them have been written by Taneli Kalvas), some definitions are present: the number of iterations, the first lens acceleration voltage $Vacc$, the plasma potential U_p, the electron temperature of the plasma T_e, the number of particles per species $n\_particles$ and the kinetic factor $Ekin\_factor\,(KF)$. The last one is given by the ratio between the kinetic energy KE and the mass m; it is defined in this way in order to be equal for all the particles, regardless of their mass (in fact they are sent with a given velocity, not energy). To have the kinetic factor in eV/amu it has been used the following equation:

$$KF\,[\mathrm{eV/amu}] \;=\; \frac{1.66 \cdot 10^{-8}}{3.2} v^2 \tag{5.6}$$

where v is in m/s.

Following the code, a first array is defined to list the masses of the simulated ions in addition to Argon and another one is for the beam current (in µA). In the section "Output definitions" it is possible to set (through boolean variables) what to print during the compiling and at the end of the

code: “debug” and “verbose” provide some status information, the GTK plot represents the trend of both the electric potential and space charge error and “plotting” produces several files (it will be explained in detail later). Before starting the geometry section, the function “fname” is defined; it is used in the “plotting” phase, to print the name of the different files produced in it.

Then, in the geometry section, the skimmer, the interface and the extraction lens are defined, using a cylindrical simmetry: only the upper part is described and then, through a mirror function on x axis, the electric field in the lower part is obtained. In this section the mesh dimension - really important in the next chapter - is also defined. After the insertion in the geometry of the “solid objects”, boundary conditions are setted: at the edges of x and y (numbers from 1 to 4) they are of Neumann type, while for the user defined electrode (7 and 8) they are of Dirichlet type. At this point the initialization of the plasma and of the solver takes place: since several nonlinear solvers are available, the first task was to decide which one was more fitting our requirements (see section 6.1). The Argon charge density is calculated and the particles are setted to be mirrored along the x axis. Thus it is possible to start the iteration loop. This is necessary since there are two contributions to the electric potential: the accelerating voltage (usually -2000 V) of the ion lens and the space charge of the flying particles. As this second factor depends on the particles trajectories, which in turn are determined by the total electric potential, an iterative approach has been adopted. The number of iterations can be set in the beginning of the code: $const\, uint\, n\_iter = 21$ Then the i index spaces in the range $0 \div n_{iter}$ in order to reach the convergence. In the following a brief explanation of the operations executed in every cycle is provided:
$i = 0$: In the first iteration the electric potential is calculated taking into account the electrodes contribute only, i.e. for $\rho = 0$. After computing the electric field, particles are sent.
$i = 1$: As particles are now present, space charge is calculated and set as a variable in the plasma model; in fact, with IBSimu, plasma is a function of space charge ρ, electron temperature T_e and plasma potential U_p. Then electric potential (and subsequently electric field) is recalculated, now as a function of both electrodes and flying particles. As the charge density only changes passing from the first to the second iteration, plasma is calculated only in this step; there is no need to recalculate it in the other steps.
For $i \geq 2$: The potential and field are recalculated and so are the particle trajectories, until both electric potential and space charge converge - i.e. until the difference for these two parameters between two iteration is nearly zero.

There are different function to produce particles, depending on which beam parameters are known:

1. add_2d_beam_with_energy (uint32_t N, double J, double q, double m, double E, double Tp, double Tt, double x1, double y1, double x2, double y2)

2. add_2d_beam_with_velocity (uint32_t N, double J, double q, double m, double v, double dvp, double dvt, double x1, double y1, double x2, double y2)

3. add_2d_KV_beam_with_emittance (uint32_t N, double I, double q, double m, double a, double b, double e, double Ex, double x0, double y0)

4. add_2d_gaussian_beam_with_emittance (uint32_t N, double I, double q, double m, double a, double b, double e, double Ex, double x0, double y0)

where N is the number of particles, J the beam current density (A/m^2), q the charge of beam particle (in multiples of e) and m the mass (u). For the first two functions, the beam is defined on a line from (x1, y1) to (x2, y2) and it propagates into a direction 90° clockwise from the direction of vector pointing from (x1, y1) to (x2, y2); at the beginning the beam profile is uniform. For the first function E represents the beam energy (in eV), while Tp and Tt are the parallel and transverse temperature, respectively, in eV. The particle speeds in direction i are sampled from a gaussian distribution with standard deviation $dv_i = \sqrt{(T_i \cdot e/m)}$, where T_i is the beam temperature in direction i (eV), e is the electron charge (C) and m is the mass of the ion (kg). With the third function, particles are flown in the positive x-direction from a starting location (center point) defined by (x0, y0) and the beam spread in the projectional space is made according to KV/hard-edged (Kapchinsky-Vladimirsky) distribution. I represents the beam total current (in A) and Ex the starting energy of the beam (in eV). The beam is made to match Twiss parameters α (a) and β (b) in projectional direction (y,y'). The rms-emittance of the beam is made to match ϵ_{rms} (e).

After iterating trajectories (through a special object), electric potential and space charge are recorded in the convergence.dat file; at the end of the simulation process this file can be found in the same folder where the source code is. If setted "true" in the beginning, it starts the last phase, the "plotting" one; this is the list of all the plots produced:

- particle traces in the geometry field;
- zoom of particle traces in the range $0 - 1$ mm (the zone including the skimmer and the focus point);
- electric potential as a function of x, usually a curve starting near 0 (the skimmer is grounded but there is the plasma potential contribution) and ending at -2000 V (the lens voltage);
- a 3D plot representing the electric potential as a function of x and y in the skimmer region;
- emittance at 50 mm, as a function of y and the angle y', reporting the values of α, β, γ and ϵ;

- charge density (in C/m^3) as a function of x; it is maximum at the beginning - at the skimmer tip -, then rapidly drops to zero, with a peak in correspondence to the focus point;
- space charge as a function of x and y in the skimmer region;
- kinetic energies (in eV) of flying particles, in a scatter plot, as a function of particles mass;
- signal intensity, in arbitrary units, for each mass, at 8, 50 and 56 mm;
- beam profile histogram plot at 4 and 50 mm;
- a scatter plot for the beam profile, representing the y value as a function of the particles mass, both at 50 and 56 mm.

Chapter 6

Simulation

6.1 Task 1 - solver

The first task was to find and compare the different available solvers, in order to find out which one is the fastest. With this aim, the computing time for 1 and 2 iterations has been determined, using one thread only and considering an Argon beam with $20k$ particles, a beam current of 1 mA and a mesh size equal to 100 µm. The outcome of this comparison is the bar plot in Figure 6.1.

As it can be seen, the UMFPACKSolver is the fastest. Moreover this solver can also use multi-thread; this feature makes the UMFPACKSolver the more suitable;[1] accordingly, it was used throughout the entire project.

6.2 Task 2 - computing time vs mesh size

As explained in the previous chapter, to calculate the electric potential and the charge density, IBSimu divides the simulation domain in small cells, with uniform size: for each cell UMFPACKSolver solves the problem, i.e. Poisson's differential equation, and returns a value. So the mesh size has a large effect on the quality of the approximation: the smaller the mesh size, the higher the quality of the simulation is (down to the limit of $mesh\_size \to 0$, representing the exact solution of the problem). The trouble is that it is impossible to decrease the mesh size infinitely. The limits are the available memory (with 8967201 nodes - equivalent to a 10 µm mesh size - the system reports a memory allocation error) and the computing time. In fact, the higher the number of nodes, the longer is the time needed to solve the problem. So it is useful to find a compromise to solve the problem with a good approximation and in a relatively short time. The relation between computation time and mesh size was investigated for mesh sizes in the range of $15 - 300$ µm. In Table 6.1 and Figure 6.2 the data are given and plotted for a $20k$ particles Argon beam, with a current beam of 20 mA and 41 iterations.

[1] Twelve threads were available on the computer used.

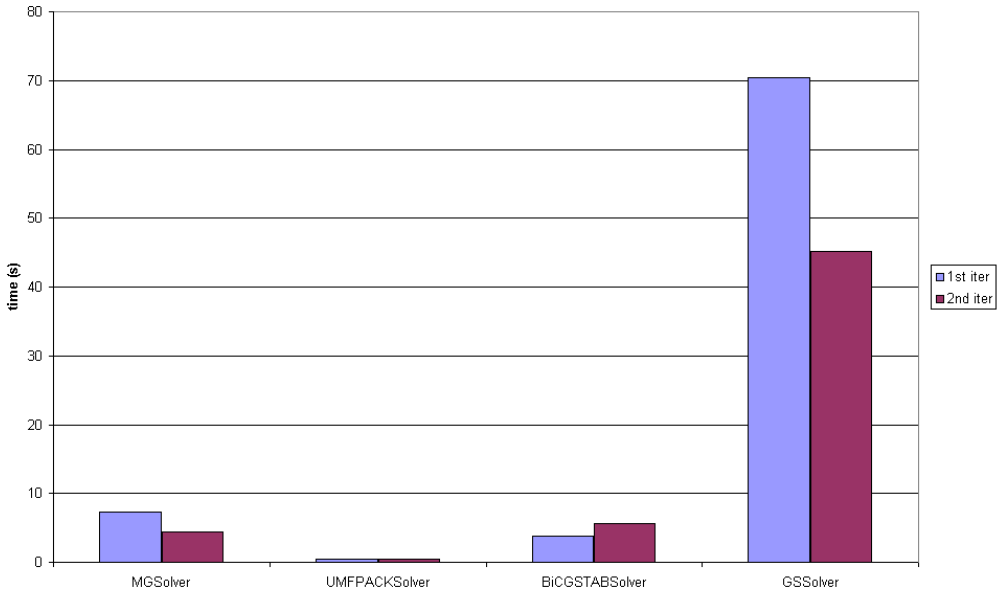

Figure 6.1: Computing time for different solvers.

Table 6.1: Computing time for different mesh sizes

mesh (µm)	no of nodes	time (s)
300	10197	77.85
250	14625	97.61
200	22761	131.92
150	40303	163.45
100	90321	259.35
50	359841	619.59
40	561801	853.01
30	997957	1343.57
25	1436481	2021.08
20	2243601	3608.08
15	3987023	8676.87

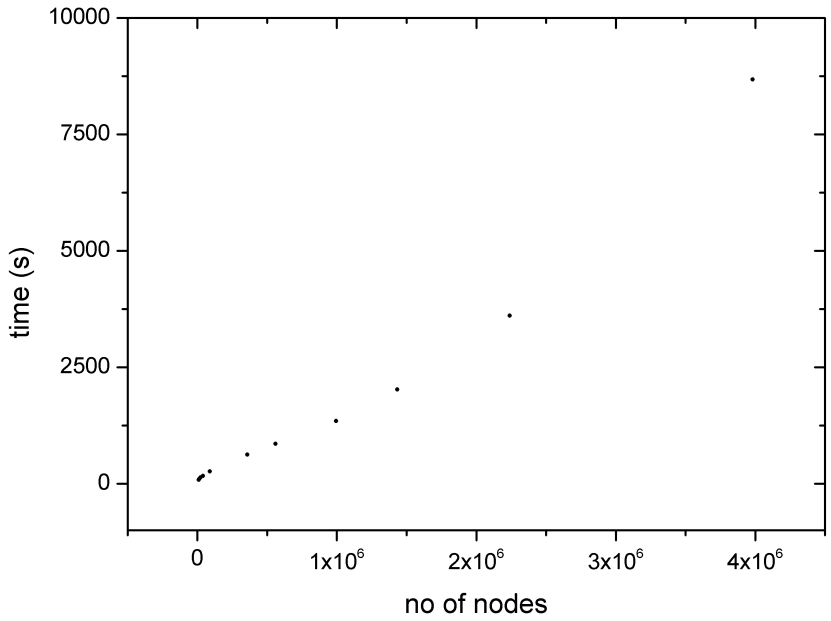

Figure 6.2: Computing time as a function of the number of nodes.

It seems that the data points plotted have 2 different trends: the first data can be fitted with a root function, then (from the 50 µm mesh) the data can be fitted with really good approximation through a square function. The functions used to fit the two curves are respectively

$$y = a \cdot (1+x)^b \text{ (Figure 6.3) and } y = A + B \cdot x + C \cdot x^2 \text{ (Figure 6.4);} \quad (6.1)$$

for the first curve $a = 0.32399$, $b = 0.59039$, for the second curve $A = 390.06724$, $B = 6.03498 \cdot 10^{-4}$ and $C = 3.71075 \cdot 10^{-10}$. As the adjusted R^2 are, respectively, 0.99772 and 0.99998 these could be considered good fits.

As explained before, the mesh size has an impact on the quality of the results: a too large mesh could lead to a simulation not well representing the reality. In Figures 6.5 and 6.6 beam profiles at 50 mm for different mesh sizes are plotted; this trend has been used as judging parameter to test the quality of the results. A brief description of the beam profile evolution from the finest mesh to the coarser one is provided, comparing each one with the former.

Because 15 µm is the smallest mesh size that can be used, the 15 µm profile has been taken as the plot which best represents the beam profile. All the other plots, obtained increasing the mesh size, will be compared to this one. The main task is to reach a good compromise between the beam representation quality and the computing time: it is useful to find a minimum number of nodes which would guarantee a good final result to attain the time optimization. In the following (through a different geometry) the beam profile was fitted with a nonlinear function, taken from the models

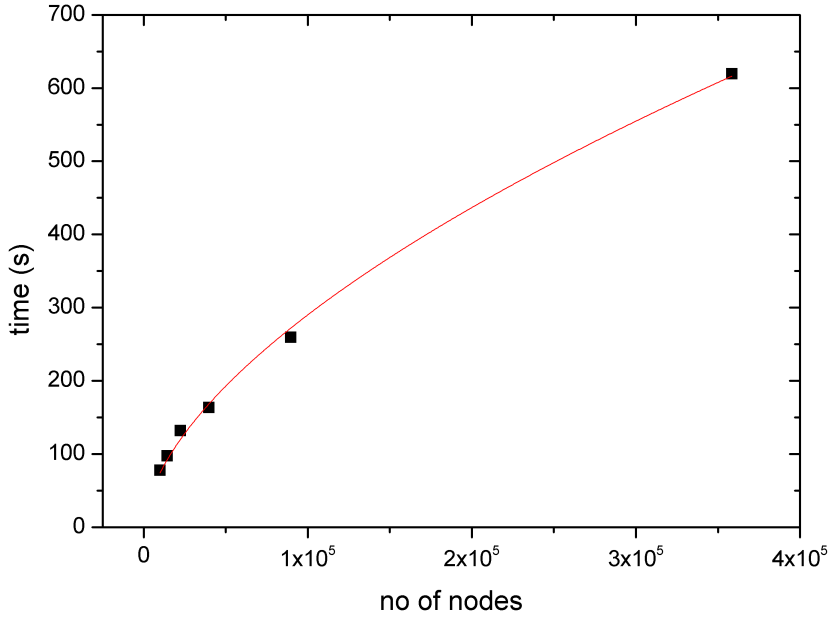

Figure 6.3: Fit for the first six points plotted in Figure 6.2.

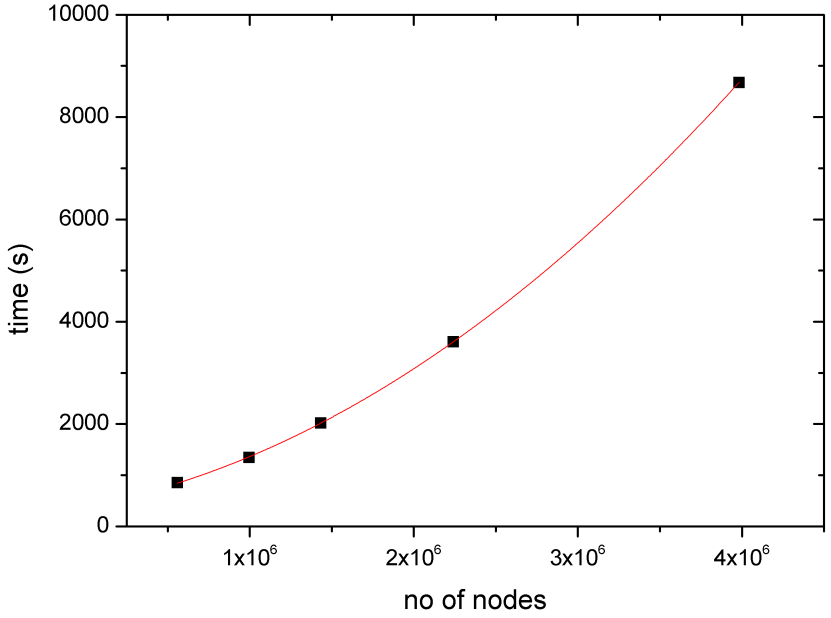

Figure 6.4: Fit for the second part of the data plotted in Figure 6.2.

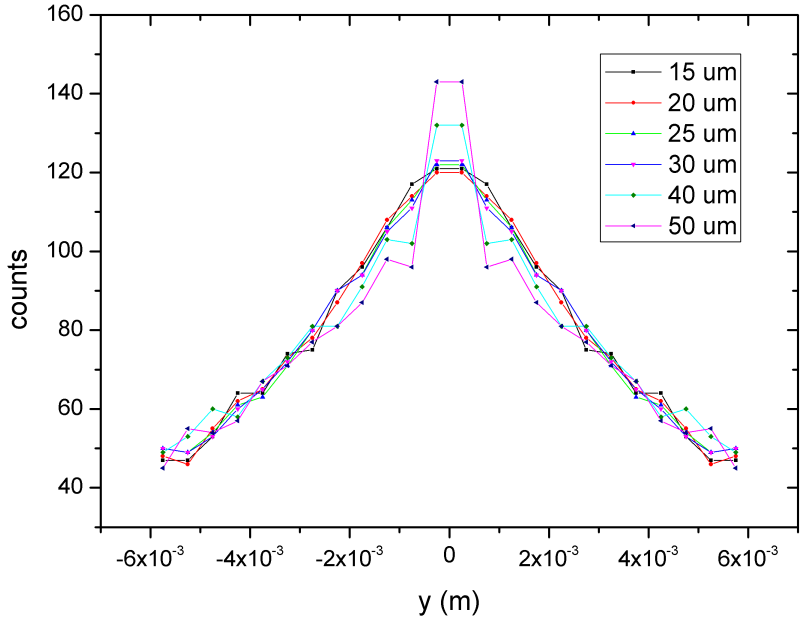

Figure 6.5: Beam profiles for mesh sizes between 15 and 50 µm.

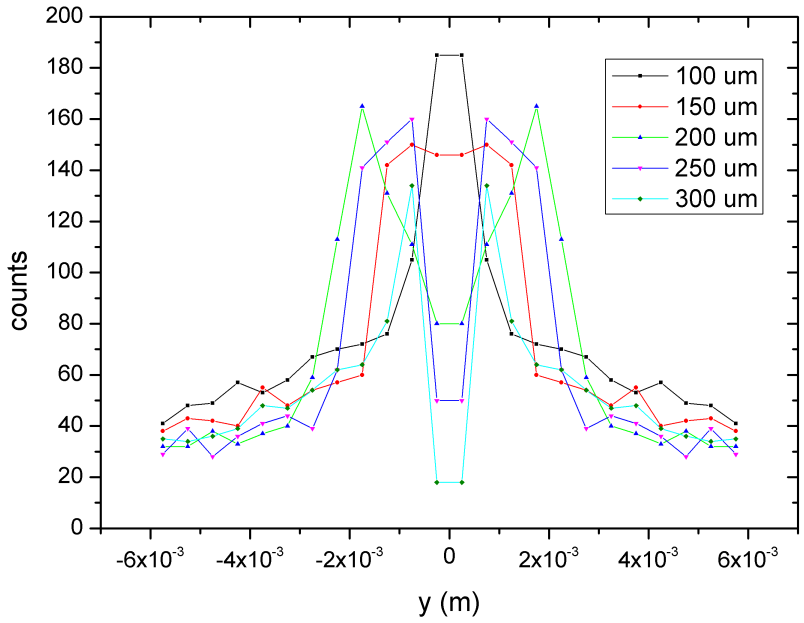

Figure 6.6: Beam profiles for mesh sizes between 100 and 300 µm.

available in Origin. Before starting the analysis it is important to underline that every plot is symmetrical due to the applied geometry: the code creates only the upper half of the simulation field (i.e. the interfaces and the lens) and then it reflects all the elements through a mirror function.

Considering the first four beam profiles (mesh sizes from 15 to 30 µm) one can note that there are no meaningful differences: increasing the mesh size in this range the beam profile is unaffected. As there are small differences, the number of counts could be considered constant: the difference between the 15 µm and the 30 µm plot counts is less than 0.2%. On the contrary, increasing the mesh size to 40 µm, considerable differences appear: even if the total number of counts is nearly equal, the curve clearly shows an atypical evolution when approximating to the center. A sharp increase occurs in the very central range: the percentual difference between the number of counts at 0.25 mm and the one at 0.75 mm is about 22%. Further increasing the mesh size the result becomes more pronounced: the total number of counts decreases (till the difference with the finest mesh is greater than 31% - for the 300 µm mesh) and also the shape changes. In the 100 µm plot there is a very high central peak (the ratio between this peak and the 15 µm peak is more than 1.5), so the trend is already much different. Considering coarser approximations, the outer peaks trend becomes more uniform, while the central one broadens and then splits in two different peaks (in the 300 µm histogram the central counts number is very low). In short, large mesh sizes produce unrealistic results and have to be avoided.

In conclusion the best compromise between quality and computing time is represented by the 30 µm mesh. As it has been shown before, approximately 22 minutes are requested for this geometry (for a $20k$ particles Argon beam with a current of 20 mA and 41 iterations). Furthermore, the space charge density was calculated (data not shown). With increasing mesh size, almost nothing changes close to the skimmer orifice. But a peak between 0.01 and 0.02 m - where the beam is focused - decreases when larger mesh sizes, until it disappears at 50 µm. The ratios between the peak height for three medium meshes, 30 µm, 40 µm and 50 µm, and the smaller mesh used are 60%, 48% and 40%, respectively. Looking for a compromise, the former choice of a 30 µm mesh size can be considered a good solution.

6.3 Task 3 - full 2D geometry switching

As the 2D mirrored geometry could not be considered a good representation of the simulation area (some troubles arise for particles traveling on the x axis), the third task was to modify the code in order to define a 2D "full" geometry. This configuration is not using the mirror function anymore, as the interfaces and the lens are completely defined. After the switch to this new geometry, some simulations were run in order to compare the new computing time with the former one. Table 6.2 shows the time for both geometries. It is important to underline that with the same mesh size the full geometry has a doubled number of nodes with respect to the mirror

Table 6.2: Computing time for 2D mirror and full 2D geometry

	2D mirror			full 2D			
mesh (µm)	no of nodes	time (s)		no of nodes	time (s)		time ratio
300	9956	77.85		24889	161.90		2.0
250	14336	97.61		35840	211.69		2.1
200	22400	131.92		56000	292.98		2.1
150	39822	163.45		99556	385.92		2.3
100	89600	259.35		224000	620.14		2.3
50	358400	619.59		896000	1493.79		2.4
40	560000	853.01		1400000	2164.20		2.5
30	995556	1343.57		2488889	4239.65		3.1
25	1433600	2021.08		3584000	7784.64		3.8

one, because the electrodes and the simulation field are defined in the lower part too.

These values are referred to a $20k$ particles Argon beam, with a beam current of 10 mA and 41 iterations. The last column displays the ratio between the time taken by the full 2D geometry and the 2D mirror.

The data ouput was used to evaluate the beam profile for the smaller mesh sizes (50 µm, 40 µm, 30 µm and 25 µm). The difference between the full 2D and the 2D mirror beam profiles gets obvious: they are no more completely symmetrical, because particles are sent randomly. The member function used in these first simulations was "$add\_2d\_KV\_beam\_with\_emittance()$". It adds a 2D beam with defined KV emittance (KV stands for Kapchinsky-Vladimirsky, whose distribution is used for the beam spread in the projectional space). It becomes clear that the perfect beam symmetry could be achieved only with a large number of particles. Analyzing the number of counts in the two sections (the left and the right one) of each plot, it results that the percentual difference is less than 1%; moreover the bias is anti correlated to the mesh size: 0.54% for 25 µm, 0.45% for 30 µm, 0.27% for 40 µm, 0.09% for 50 µm. In order to compare the beam profile obtained with the two different geometries, one simulation with a $100k$ particles Argon beam, with a current of 10 mA and a 30 µm mesh size was used. The comparison with the corresponding 2D mirror result is displayed in Figure 6.7.

The differences can be summarized in the following way: first of all, even if the trend at the edge is similar, the midmost increasing is larger in the full 2D case. Moreover, the number of central counts is much higher in the full 2D case: the ratio between the peak heights is about 1.2 and the percentual difference of the total number of counts between 2D mirror and full 2D curve is about 19%. This result shows the importance to switch to the new geometry; in fact it clearly proves that the mirror 2D case was affected by some errors in the trajectories calculation for particles in the center of the beam, the region we are mostly interested in.

Finally, some attempts have been done to fit the full 2D beam profile

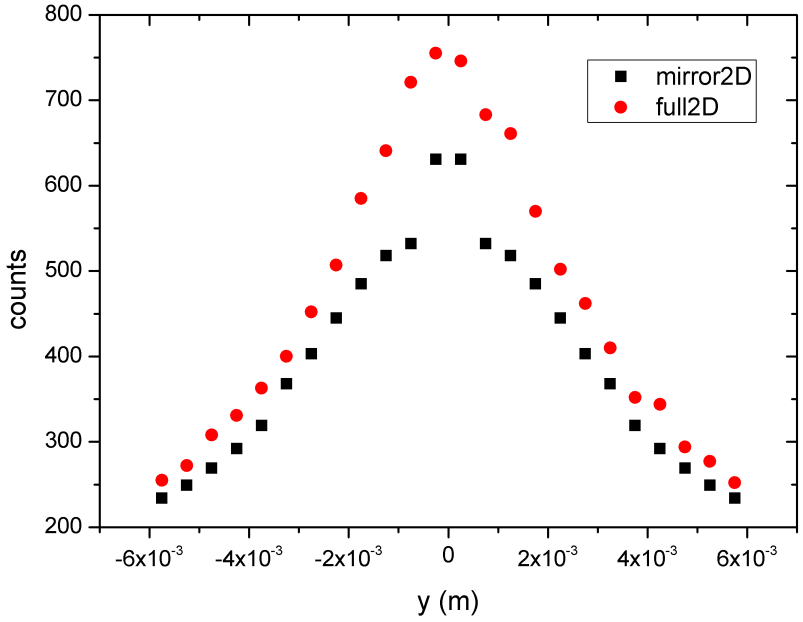

Figure 6.7: 2D mirror - full 2D beam profile @ 50 mm comparison.

(using the data obtained with the 30 µm mesh) with a known distribution: as the Gauss fit had a R^2 adjusted of only 0.99134, it has been chosen a Lorentzian fit, obtaining a better result (R^2 adjusted = 0.9963). This fit is displayed in Figure 6.8.

Olney, Chen and Douglas [30] measured gas flow profiles downstream the skimmer using an impact pressure probe. It consisted of a small 0.254 mm diameter orifice in a flat plate at the end of a 6.35 mm od tube that was connected to a pressure gauge. The gas flow profiles were measured for an interface arrangement with a first stage pressure (P_1) of 3.3 Torr and a sampler-skimmer spacing of 6.4 mm; this interface is similar to that used on commercial ICP-MS systems. Using French calculations [47], they found the density off the centerline:

$$\frac{n(r,\phi)}{n_0} = B\,cos^2\left(\frac{\pi\phi}{2C}\right)\left(\frac{r}{r_0}\right)^{-2} \tag{6.2}$$

where ϕ is the polar angle between the centre axis and the point of interest, r_0 the orifice radius, r the distance of the probe from the source ($r^2 = x_p^2 + z_p^2$, where z_p is the distance of the probe from the centerline) and B and C are, respectively, 0.643 and 1.365 (for Ar).

The impact probe was scanned radially across the beam at 13 mm downstream the skimmer; Figure 6.9 shows the free jet gas flow profile obtained from impact pressure measurements made at several distances from the centerline. Considering the geometry and settings differences between the case on study and the work by Olney, Chen and Douglas, the beam profile obtained with IBSimu is consistent with the one shown in their work.

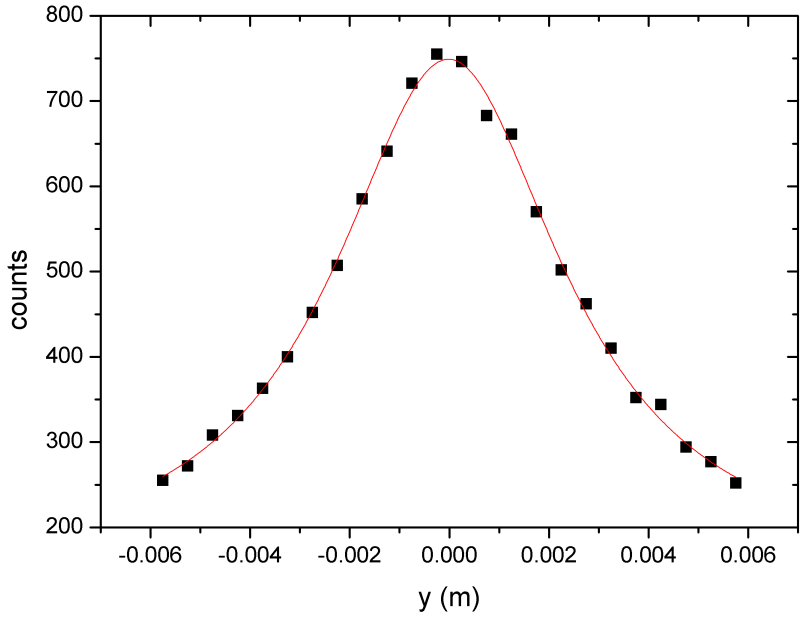

Figure 6.8: Lorentz fit.

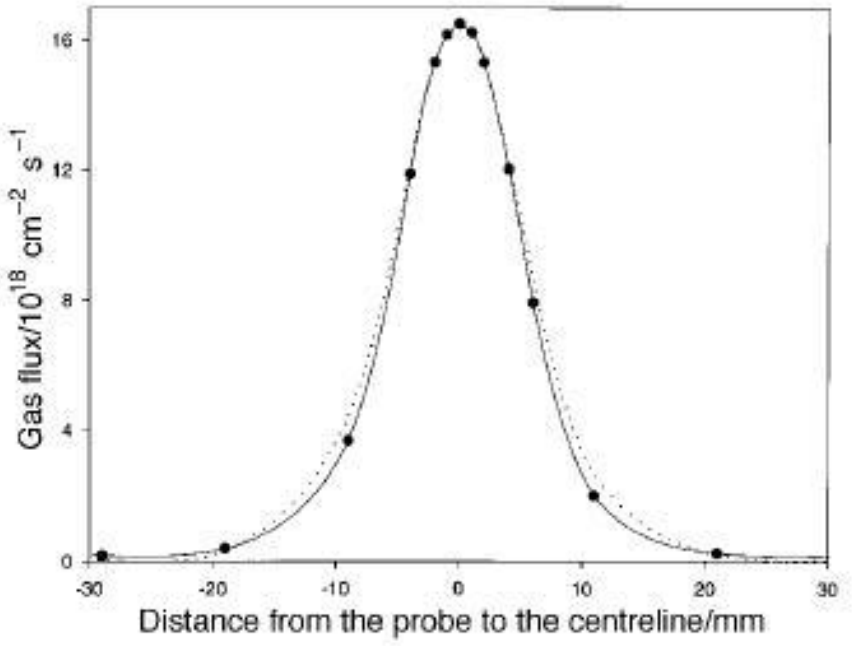

Figure 6.9: Free jet profiles calculated - dotted line - and measured - filled circles; the density field of equation 6.2 is multiplied by an additional factor $cos\phi$ to account for the decrease in the apparent area of the probe (solid angle) viewed from the source orifice as the probe moves off-axis [30].

6.4 Task 4 - U_p and T_e investigation

The optimum mesh size for a mirrored geometry was determined to be 30 µm. Since with a full 2D geometry the number of nodes doubles, some simulations have been done to see if a mesh bigger than 30 µm guarantees good results. It has been found that using a 50 µm mesh the beam profile does not change; so for the following task, this mesh size has been used. The aim was to analyze the effect of plasma potential (U_p) and electron temperature (T_e) on the beam profile. These parameters have been chosen because they define the plasma itself and they represent the main contribution to the particles trajectories. After few simulations it became clear that it was necessary to change the particle seeding function; we soon realized that "$add\_2d\_KV\_beam\_with\_emittance()$" did not take into account the charge density and it was initializing the plasma potential to a Null value (no differences were seen varying the plasma potential). However, the beam profiles calculated in the former task were correct, because with such a high current beam the space charge effect was significant. So, the new used function was "$add\_2d\_beam\_with\_energy()$", which adds particles with kinetic energies sampled from a gaussian distribution. Unfortunately, it was not possible with this new function to set a beam current greater than 5 µA; for higher values, particles are grouped in bundles (needless to say that this result can not be true). So, with a $100k$ particles Argon beam, a current of 5 µA and 21 iterations (after having checked the convergence) some runs have been done with different plasma potential values: $0.1, 0.2, 0.5, 1, 2, 5, 8, 10, 15$ and 20 V. The outcome beam profile does not have any significative difference until 1 V, then, increasing the plasma potential, the number of counts and the peak height decrease. Moreover, above 10 V all plots are almost identical, both in shape and number of counts; as a consequence it does not make sense to investigate low or high intervals and the study was concentrated on the range $2 - 10$ V. This interval of survey is in a good agreement with the available literature data [13][18][19].

The trend shown in Figure 6.10 is probably due to the space charge effect: it becomes more intense with a higher potential, especially in the center of the beam, where the number of particles is high. So, increasing U_p, more and more particles are lost on the skimmer walls; in a calculation for 10 V, this number could be near to 80% of the total number of starting particles. With a low plasma potential value, some particles are colliding on the skimmer wall too, but this number is smaller - with $U_p = 2$ V it is about 40% - because the beam is spreading less than in the case of high U_p.

Regarding the charge density plot, its trend does not change. The only difference is in the peak corresponding to the focus point: its height halves from 2 to 6 V and then remains constant until 10 V. In conclusion of the plasma potential evaluation, one can say that the sharpest beam profiles are achieved at lowest potential, in particular at $U_p = 2$ V.

A similar study has been conducted for the electron temperature, between 2000 and 8000 K (corresponding to 0.259 and 1.035 eV, respectively, using the equipartition theorem). The number of publications inquiring this

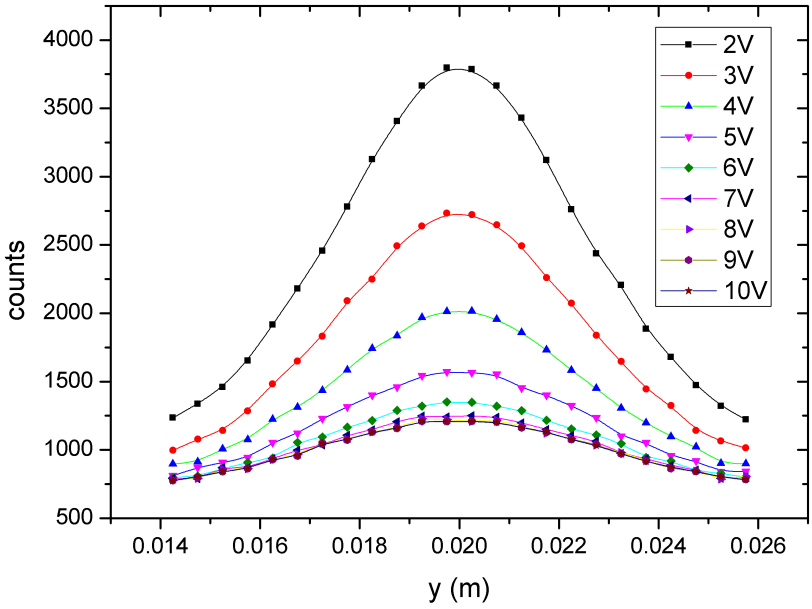

Figure 6.10: Beam profiles for $T_e = 5000$ K and different plasma potentials.

topic is considerable [18][26][32][35][36]; the reported values range between 1000 and 16000 K, depending on many factors (distance from the load coil, radial position, dry or wet plasma, introduced analyte and radio frequency power setting). The results for different plasma potentials (summarized in Figures 6.11 and 6.12) show a different behaviour.

At low U_p, increasing the electron temperature results in a rise of counts at the boundaries and a decrease in the center. Probably due to a greater thermal agitation, the beam profile becomes smoother (this flattening is more uniform than the one obtained increasing U_p). On the contrary, if the potential is high the plot is already flat and by varying the temperature nothing changes. The best solution would be having a sharp peak (like the one obtained for the lower temperature) with a high number of counts (as it happens for high T_e). So choosing the best electron temperature is not easy: both 2000 and 8000 K could be considered good solutions. In the charge density plot, increasing the electron temperature, the peak corresponding to the focus point moves slightly toward the skimmer, while its intensity increases and the full width half maximum (FWHM) gets smaller. These changes are small, so they could be neglected. The best configuration would be a focus point far away from the skimmer, in order to minimize the space charge effect.

In order to better understand how the plasma potential and the electron temperature affect the simulation and, above all, to find the combination that gives the best result, three 3D plots have been done, representing the total number of counts, the peak height and the FWHM as a function of the two fundamental parameters. The results are depicted in Figures 6.13

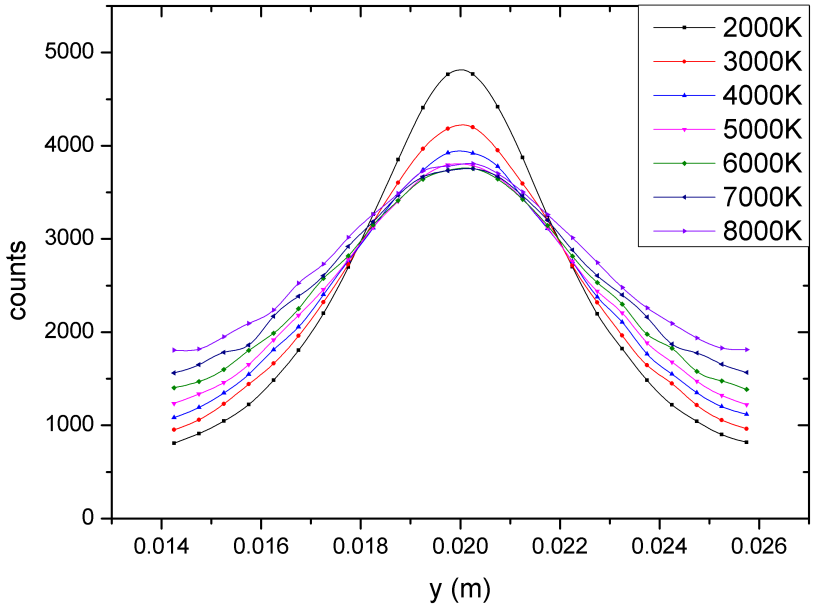

Figure 6.11: Beam profiles for $U_\mathrm{p} = 2$ V and different electron temperatures.

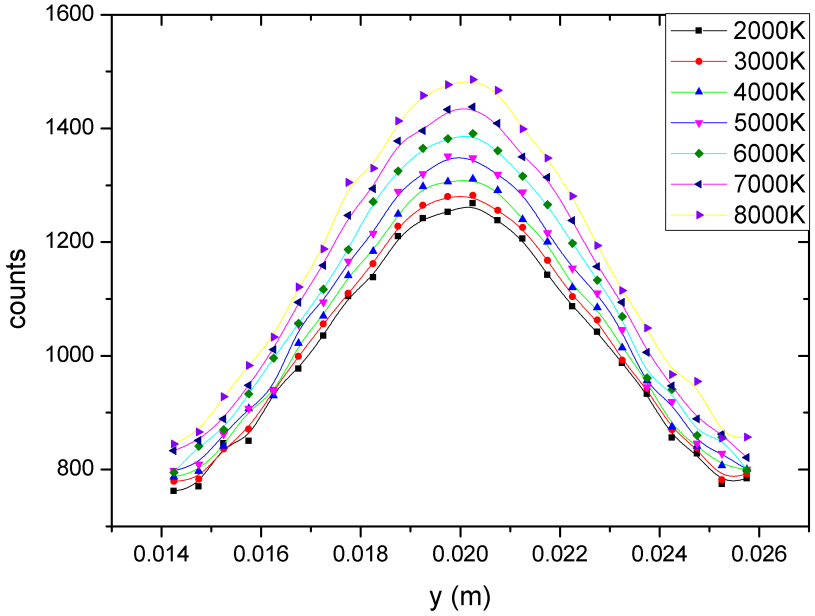

Figure 6.12: Beam profiles for $U_\mathrm{p} = 6$ V and different electron temperatures.

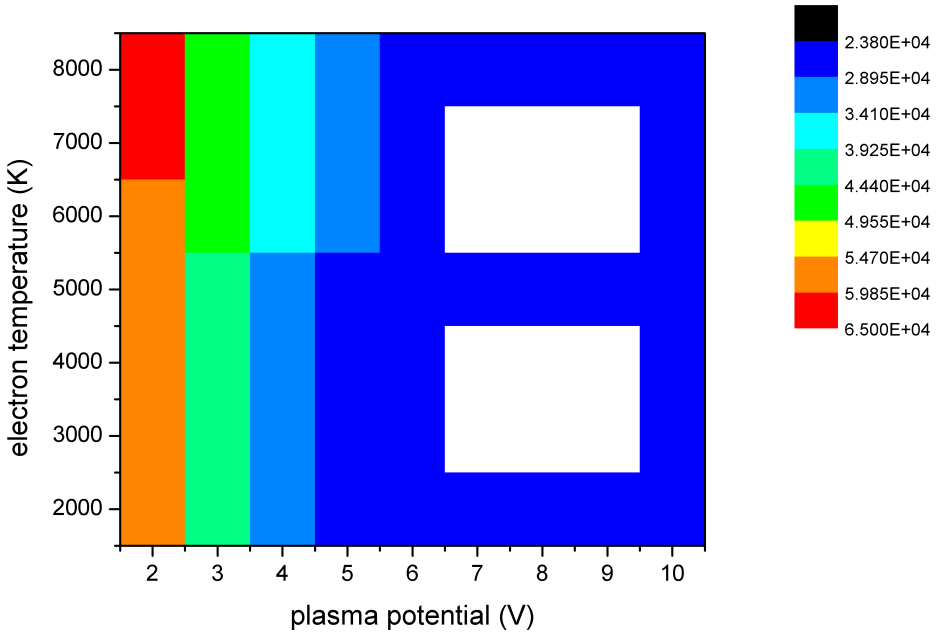

Figure 6.13: Number of counts as a function of U_p and T_e.

to 6.15.

As evaluated before, it was shown that $U_p = 2$ V is the best plasma potential. Regarding the electron temperature, two different values could be good: with $T_e = 2000$ K the peak is narrow (lowest FWHM) and his height is maximum. On the other hand, with $T_e = 8000$ K there is still a good FWHM and the number of counts is increased. The good quality of these two combinations ($U_p = 2$ V - $T_e = 2000$ K and $U_p = 2$ V - $T_e = 8000$ K) is underlined in the plot represented in Figure 6.16, obtained with a combination between number of counts and FWHM.

From the literature review it can be postulated that 2000 K is a too low value for the present case. In fact the electron temperature in a Fassel torch is around 10000 K and the plasma bulk properties remain unchanged as it proceeds through the sampling orifice [19]; the only significant electron loss at the walls of the sampling plate is confined to distances of the order of one Debye length - 10^{-2} to 10^{-3} mm. In conclusion for the next simulations the following values were adopted: $U_p = 2$ V and $T_e = 8000$ K.

6.5 Task 5 - different masses

Once completed the Argon beam simulations, the next step was to introduce other particles, to see the particles beam profile. Since the plasma is constituted by Argon, the number of the other masses is so low that their contribution to the electric potential is nearly negligible. So, to speed up the simulation, it was convenient to simulate only Argon in the first runs

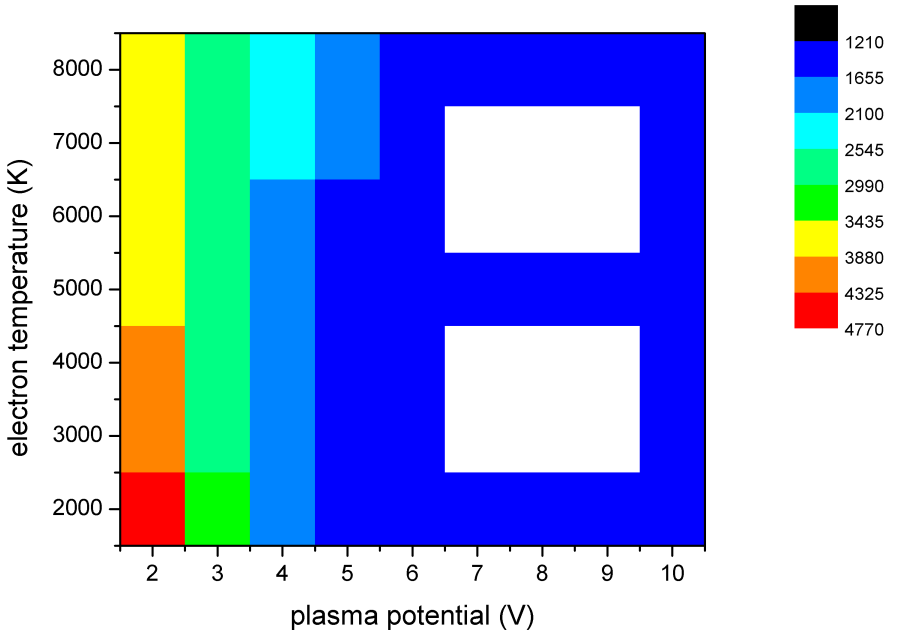

Figure 6.14: Peak height as a function of U_p and T_e.

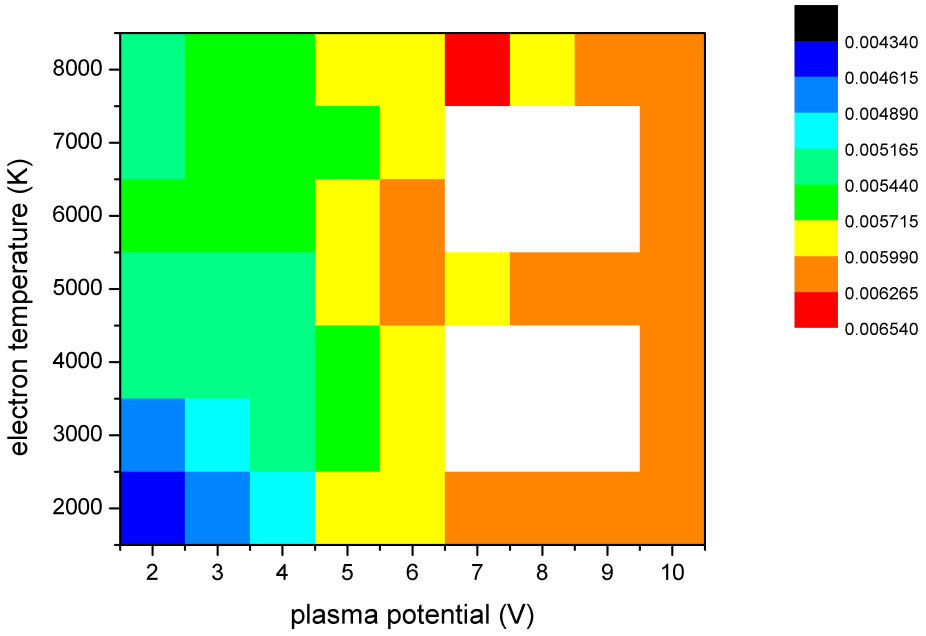

Figure 6.15: Full width half maximum as a function of U_p and T_e.

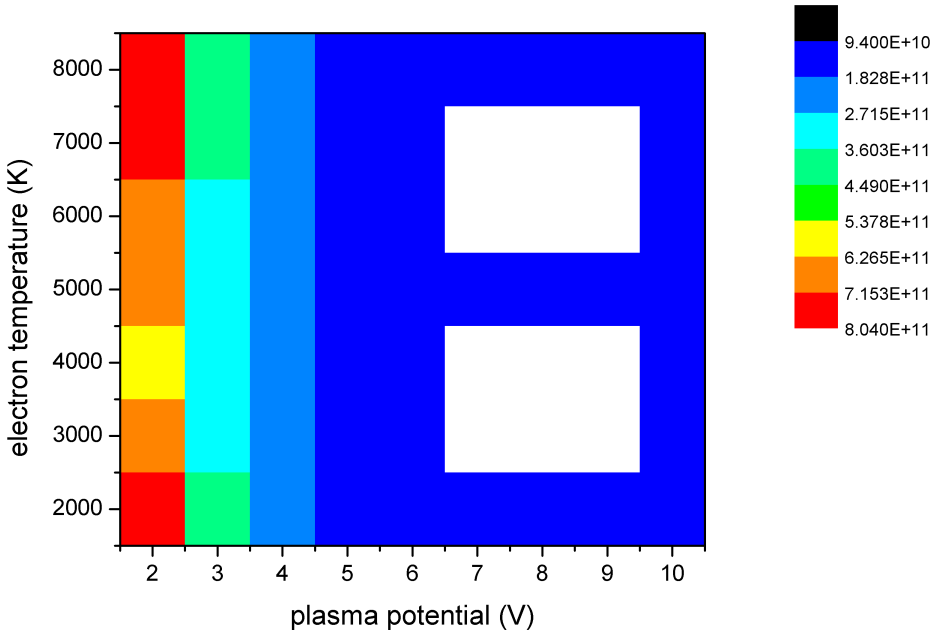

Figure 6.16: (number of counts)^2 / full width half maximum.

(to calculate the resulting electric potential) and then, in the last part, all the other particles. This topic will be discussed in detail in the next section.

The first set of simulations was aimed to study how the number of counts is affected by the mass of the projectile at different potentials. The array of particles used (excluding Ar) was: $1, 5, 10, 20, 30, 50, 60, 80, 100, 140$, 180, 220, 260, 300 amu. $100k$ particles per species were seeded, with a 50 µm mesh, $T_e = 8000$ K and for different plasma potentials: $2, 3, 4, 6, 10$ V. The signal intensity per species, downstream the lens orifice, is given in Figure 6.17.

The trend obtained is logarithmic for each potential, even if with increasing U_p the curves are flattening. A good fit has been found: the curve $y = a - b \cdot ln(x + c)$ always provides R^2 adjusted greater than 0.999. Comparing the plot in Figure 6.17 with the one obtained at 50 mm (just before the lens orifice) and shown in Figure 6.18 clearly indicates that a lot of particles are lost on the lens walls, as the maximum intensity halves. Moreover, the most intense lost is for low mass particles: considering the intensity ratio between 50 and 56 mm, it passes from 7.57 for m=1 to 3.87 for m=100 to 2.08 for m=300. This could mean that lower masses are mostly at the boundary of the beam - whilst higher masses are in the centre - or that the spread is higher for light particles - making the profile nearly flat. In the following this particular distribution was studied through the beam profile plots.

Considering instead the signal intensity per species for different electron temperatures, the curves are not affected and the intensity difference is nearly negligible (see Figure 6.19). Increasing the electron temperature, the

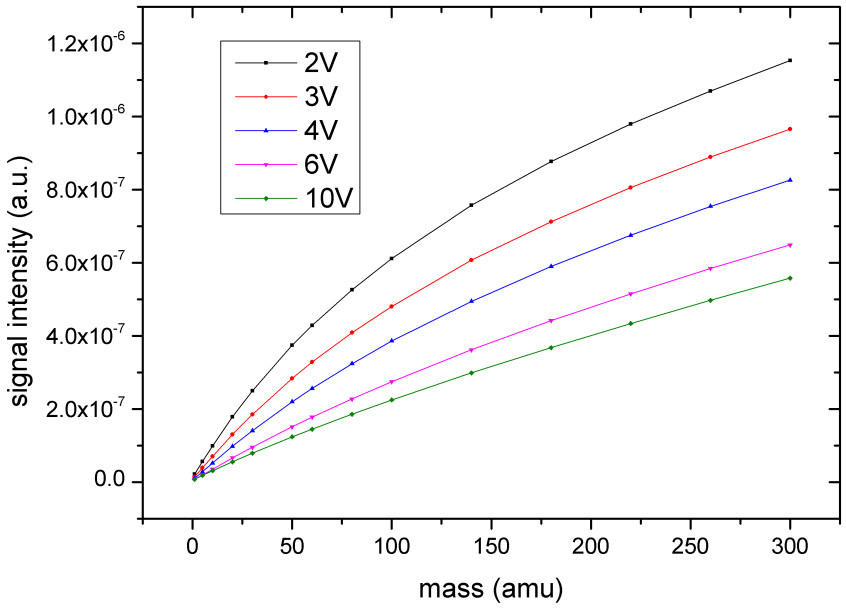

Figure 6.17: Signal intensity per mass @ 56 mm for T_e = 8000 K and different plasma potentials.

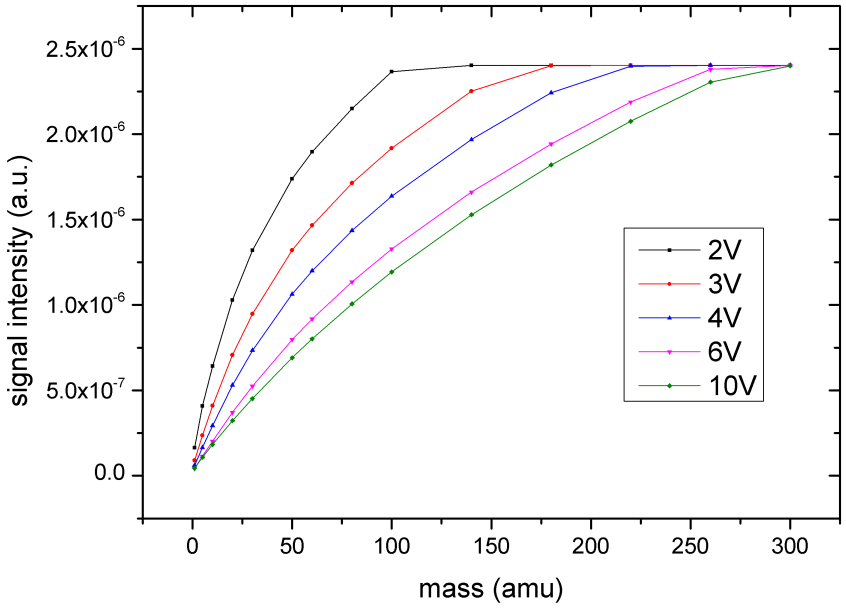

Figure 6.18: Signal intensity per mass @ 50 mm for T_e = 8000 K and different plasma potentials.

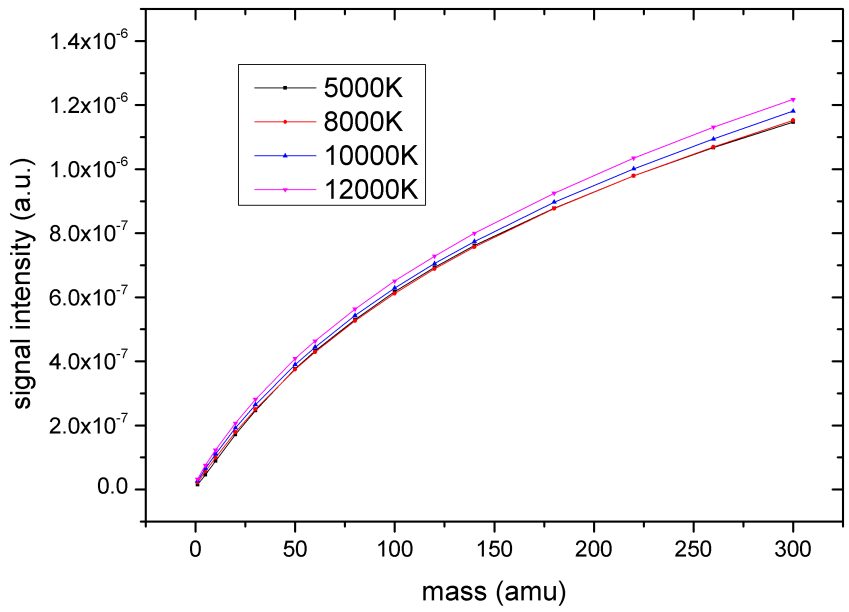

Figure 6.19: Signal intensity per mass @ 56 mm for $U_p = 2$ V and different electron temperatures.

number of counts also increases, in a non linear way: higher the mass, bigger the difference from two different temperatures is. Nevertheless the gap is quite small: for m=300, the percentual difference between 5000 and 12000 K (in respect to the lower T_e) is about 6.

The effect of an electron temperature changing on the number of counts for m=300 is shown in Figure 6.20.

In order to see in detail how plasma potential and electron temperatures affect the beam profile, some simulations have been run with the three masses (in addition to Ar) which give an overall view on all possible particles: $1, 150, 300$. The result is consistent with the one obtained in case of Argon: it validates 2 V as the best plasma potential and the trend for different T_e is equivalent to the one showed in the previous section. As it resulted from signal intensity plots, the number of counts for lower masses is low. Running the same number of particles would make a comparison between beam profiles of mass 1 and 300 impossible: the former one would be completely flat compared to the other. As the beam profile evolution (changing U_p and T_e) is the same for mass $40, 150$ and 300, it is reasonable to presume this trend is identical for mass 1. The beam profile was studied in detail for different electron temperatures (Figure 6.21).

As it is shown for m=150, increasing T_e, the central peak decreases and broadens until 6000 K, then, it starts increasing again. Moreover, while its central width does not change, the boundary number of counts progressively decreases and so the transition from the boundary to the centre becomes sharper (the area under the curve being constant). The only difference with

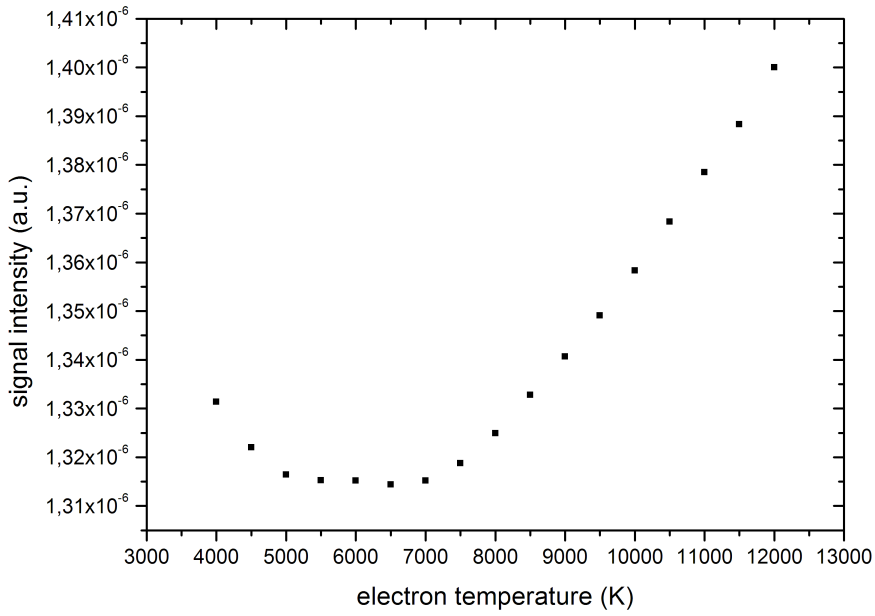

Figure 6.20: Signal intensity @ 56 mm for m = 300 and different electron temperatures.

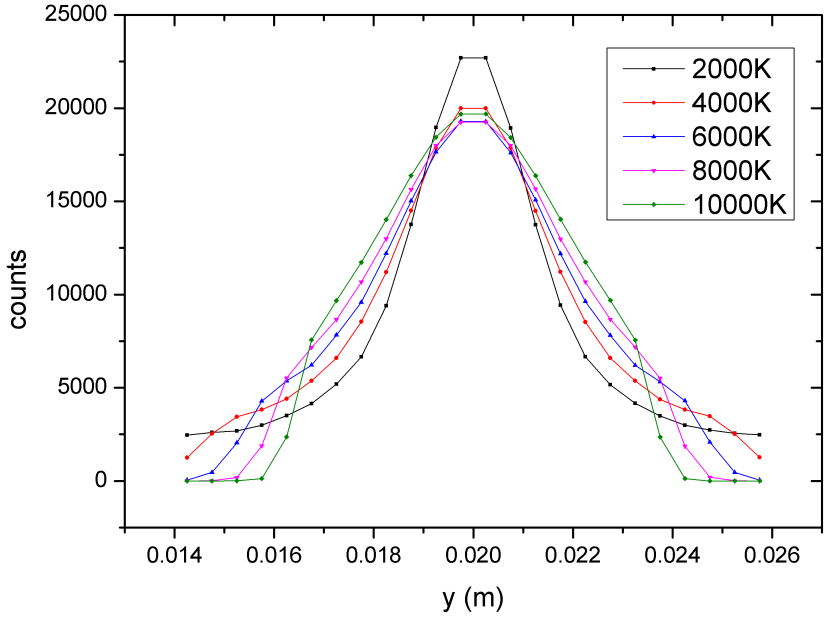

Figure 6.21: Beam profile @ 50 mm for U_p = 2 V, m = 150 and different electron temperatures.

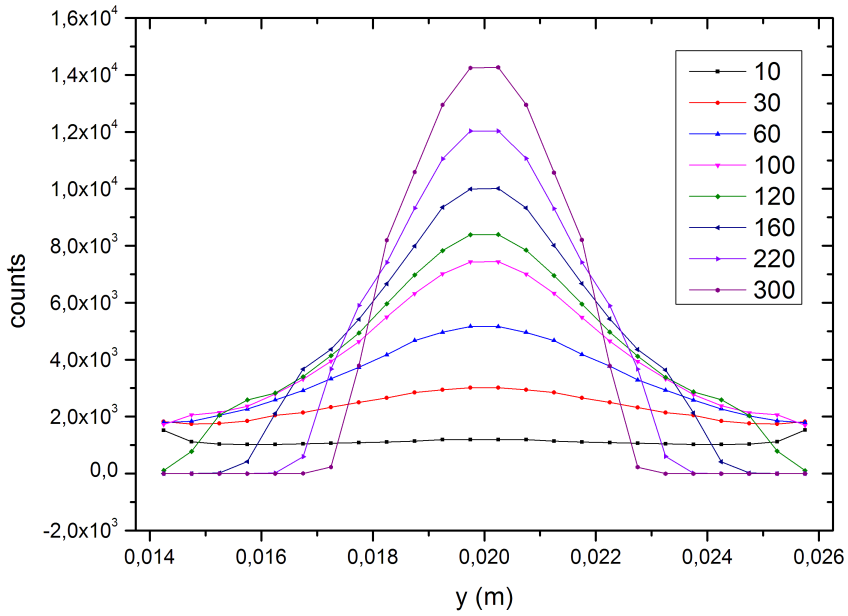

Figure 6.22: Beam profile @ 50 mm for different masses, for $U_p = 2$ V and $T_e = 8000$ K.

argon is right in this area: in the analyzed case the boundary number of counts drops to zero (this feature is even more noticeable for m=300) at about 4 mm from the centre, giving to the profile a more sharp shape. This phenomenon has been more deeply investigated.

With a set of projectile similar to the one used for the first plots, the beam profile for each species has been represented - for $U_p = 2$ V and $T_e = 8000$ K. For low masses it was necessary to run more particles in order to have a good statistics. Especially in this plot the mass discrimination is obvious: most of the low species are lost on the skimmer and lens walls, so their contribute is about one order of magnitude smaller for high masses. As observed before the beam profile progressively changes: while Argon (previously studied) can be fitted with a lorentzian curve, increasing the mass, the profile loses its tails and acquires a better defined shape. Starting from m = 160, the boundary number of counts drops to zero; in other words, high masses are well focused. This is an important result, because it means that all these particles will pass through the lens orifice.

To better visualize the results it was convenient to represent the beam profile ratio between a given mass and mass 120. This value was choosen because its curve is the first having nearly zero counts at the edge. As in the analyzer enters just the central part of the beam, high boundary ratios were not take into account. The plot in Figure 6.23 clearly shows the mass discrimination as a function of atomic mass and radius (radial distance from the beam center - defined as 0.02 m).

This plot underlines how much sharper the beam profiles are for high

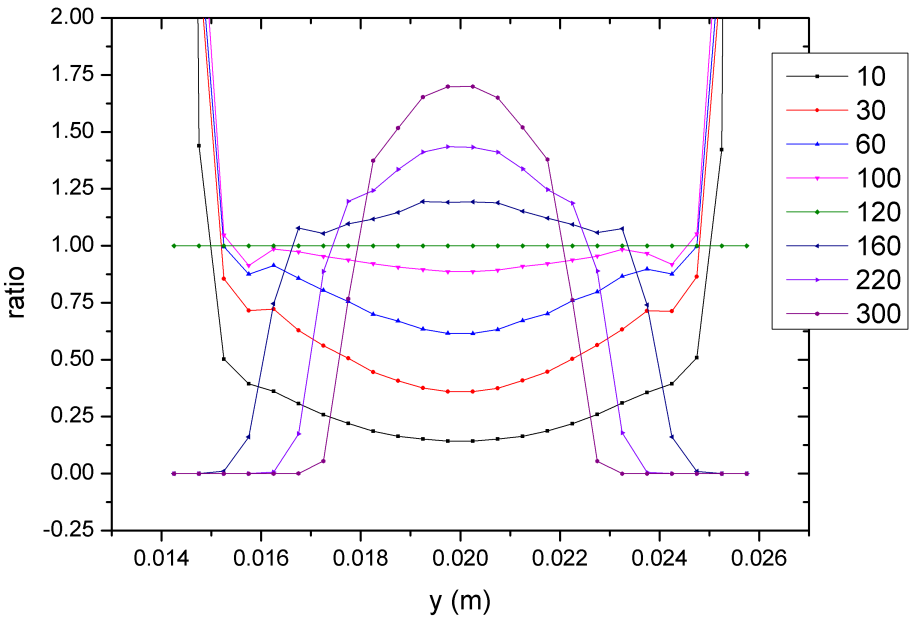

Figure 6.23: Counts ratio @ 50 mm for $U_p = 2$ V and $T_e = 8000$ K.

masses: it is important to notice that the resulting hollow for low masses does not mean the total number of counts in the center is lower than at the boundaries, but just that the number of counts is increasing slower (to the centre) for low than for high masses.

6.6 Task 6 - iteration settings

As anticipated, with many projectiles it is convenient to split the iteration phase in two parts: in the initial runs only Argon is seeded, while in the last all the other particles (defined in the "masses" array) are added. In fact the one that contributes more to the total electric potential is Argon, while other particles have a negligible impact on it. Some simulations have been run to answer the following questions:

- With a fixed number of iterations, does the beam profile change varying the number of initial and final iterations? How? Is the computing time affected?
- How many particles are needed to fly in the last run(s) in order to have a good compromise between a good beam profile and a short computing time?
- How many particles are optimal for the first runs?

The first comparison was aimed to see which changes occur when the number of iterations in which all particles are sent vary. With a fixed

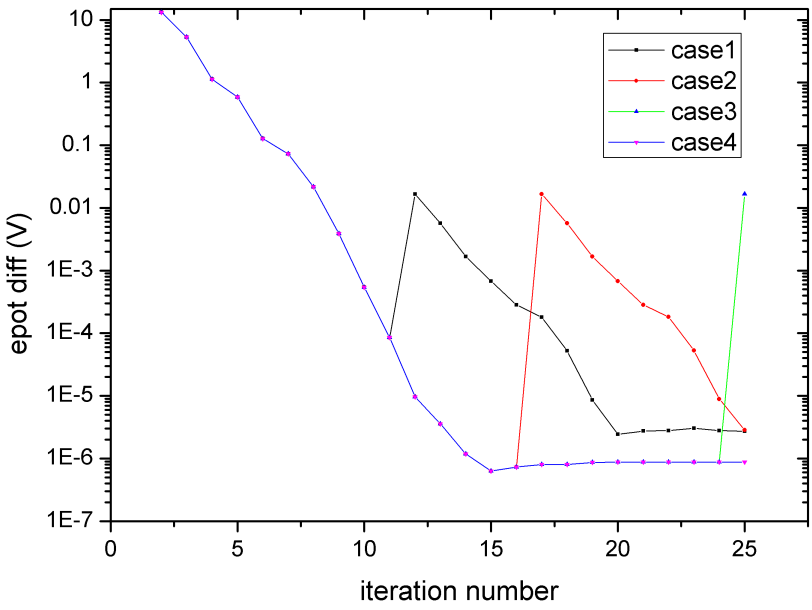

Figure 6.24: Electric potential difference as a function of iteration number for the analyzed cases.

number of total iterations (25), different combinations have been tried: (case 1) 10+15, (case 2) 15+10, (case 3) 23+2, (case 4) 24+1. The first parameter checked was the electric potential convergence: in Figure 6.24 the electric potential difference is shown for the considered cases.

There are two points that have to be underlined: (i) the y axis has a logarithmic scale - this means that the initial decrease is sharp - and (ii) in case4 the electric potential difference is not calculated after flying all particles - because in the code the particles are sent after the electrical potential is recalculated. [2] The increase in each curve is due to the addition of other species: considering that the total electric potential is 2000 V, this operation does not significantly affect the result. To validate this hypothesis, the obtained beam profiles have been compared to the one obtained in the first case. With $15 + 10$ iterations the result is identical (exactly the same number of counts per interval) to the first one, while case 3 and 4 have some small differences, even if the profile shape remains unchanged. As the computing time decreases from 34 (case1) to 29 (case2) to 19 minutes (case4), the conclusion is the following: reducing the number of final iterations does not significantly affect the final result; the difference is negligible in all cases even for particles with low mass - in which case the total number of counts is low. This result has been validated also in the case of $20k$ particles in the first runs and $100k$ in the last one.

Then, two simulations with a different final number of particles have been performed: $50k$ and $100k$. For low masses (m=1 in the analyzed

[2] So case4 represents the convergence for Ar only.

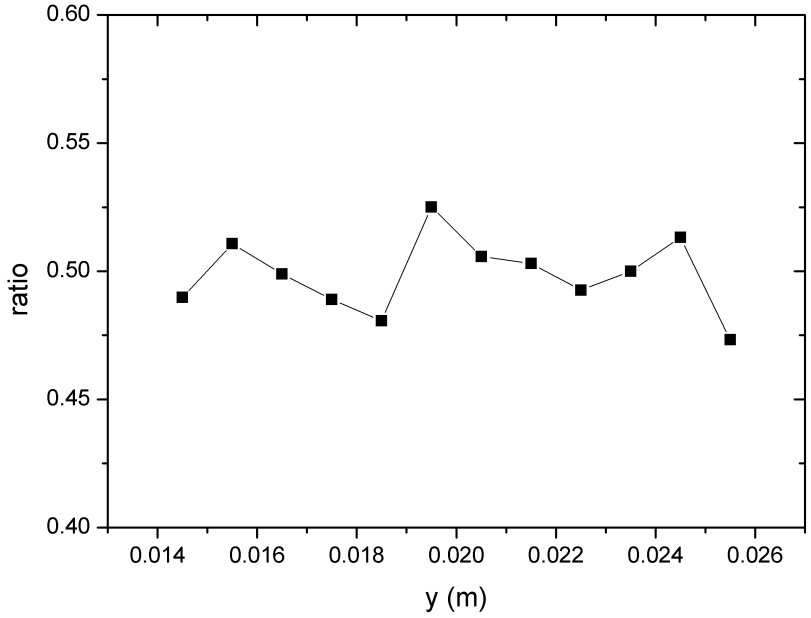

Figure 6.25: Ratio between the beam profile @ 50 mm with $50k$ particles and the one obtained with $100k$ particles, for m=1.

case) the number of particles reaching the end of the simulation field is low and random fluctuations affect significantly the beam profile. As the fluctuation amplitude does not change passing from the first to the second case, the former one represents a coarse approximation (as clearly indicated in Figure 6.25).

Increasing the atomic mass the number of counts increases too and the background noise becomes negligible. So it is better to split the following discussion in two cases. For high masses the solution is likewise the precedent: running with $50k$ instead of $100k$ particles is a good approximation and the advantage is that the simulation time is reduced - halved in the case of $10 + 15$ iterations. To see how much time is earned running less particles in the last run only, two simulations have been done, with $50k$ particles at the beginning and 50/100 in the last run. The difference is about 15%, but is not really significant as the total time needed is around 20 minutes (19 min in the first case and 22 min in the second). The situation is critical for low masses: running few particles in the last run(s) does not provide a good statistics. Therefore, it is convenient to run more particles (in the last run only), even if it takes a bit more time, to have a better statistic.

To conclude this study, the last parameter to change was the number of particles in the first runs: [3] the simulation result for $20k$ particles was compared to the one obtained for $50k$ - with $100k$ particles in the last runs

[3] A variation in the number of Argon particles does not change the total charge density (it is defined as constant); the only quantity changing is the charge density carried by each particle.

- firstly for $10+15$ and then for $24+1$ iterations. In both cases there are no differences between the two simulations - for the case "$10 + 15$ iterations" every single beam has the same amplitude as in the other case and similarly for "$24 + 1$ iterations". In the first case even the computing time does not importantly change, probably because the time needed to seed only Argon is smaller compared to the one for all particles. On the contrary, the difference is notable in the second case: instead of 22, just 14 minutes are needed. Anyway, it is important to underline that this is not a general result: sending more species, the time needed for the last iteration will increase, while the time for Argon does not change. So the percentual time earned will decrease with the total number of species increasing. Anyhow decreasing the number of Argon particles does not affect the beam profile quality, so it can be reduced to $20k$.

The following list summarizes the settings that optimize both the results quality and the computing time:

- number of iterations: $24 + 1$;
- number of particles in the last run: $100k$;
- number of particles in the first runs: $20k$.

6.7 Task 7 - Cadmium

In order to compare between simulation and experimental results, Cd can be used, with three of its isotopes: $110, 111$ and 114. Through this comparison it is possible to find out the plasma fundamental parameters that characterize the used instrument. In the following a short experimental description of the implantation and measure of ions number is given. In order to detect the radial distribution of Cd - this element is used because it shows a significant radial dependence -, an Aluminium target was placed at the base of the extraction lens. Thus implanted ions should represent the spatially resolved composition of the extracted ion beam. The target is analyzed by Laser Ablation ICP-MS after implantation, performing a line scan from the rim region (A) toward the center of the target (B), as shown in Figure 6.26.

The spacing between two adjacent ablation spots (150 µm) is sufficient to have a high spatial resolution density and, in the same time, to avoid overlapping [43]. Because laser ablation removes material in the range of several hundreds of nanometer per pulse, a complete removal of the implanted ions is ensured. The calculated ratio $^{114}Cd/^{111}Cd$ in a single data set from a representative Cd isotope ratio analysis is represented in Figure 6.27, with the corresponding transient signal for ^{114}Cd.

Since laser ablation provides spatially resolved information on the implanted matter, a relation between Cadmium signal and ion beam intensity has to be assumed in order to deduce the ion beam profile. However, the sputtering due to the high Ar-beam current jeopardizes this relation; the

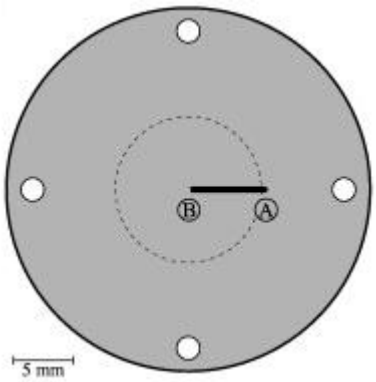

Figure 6.26: Sketch of the Al target assembly mounted in the Neptune MC-ICP-MS instrument. The dotted line defines the area exposed to the ion beam and the position of the line scan is given by the black line [43].

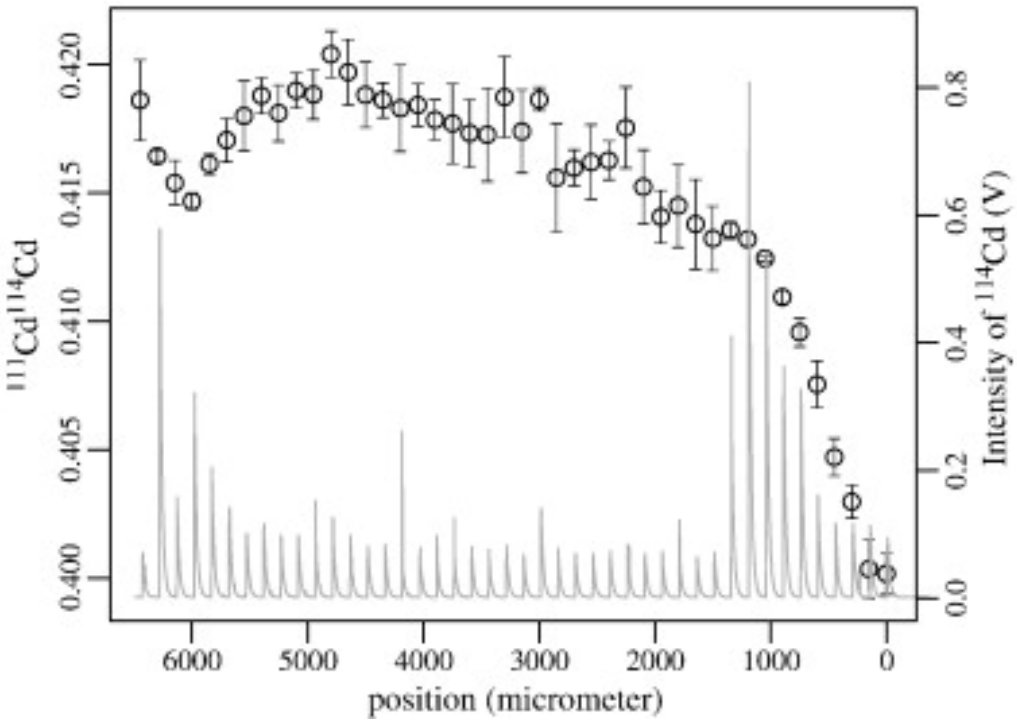

Figure 6.27: $^{114}Cd/^{111}Cd$ isotope ratio (open circles) and signal intensity [43].

Table 6.3: Set of simulation run

run number	U_p (V)	T_e (K)
1	2	8000
2	3	5000
3	4	10000
4	8	5000
5	2	5000
6	2	10000

signal intensity is high in an annulus around 1 mm from the centre and then decreases when moving toward the centre. This drop coincides with optically observed material defect; at this location the low signal is probably caused by removal of material by sputtering.

To plot the ratio $^{114}Cd/^{111}Cd$ against the distance from the centre, some simulations have been run, with the following configuration set:

- 35 iterations, 20 with Argon only + 15 with all the particles,
- masses array = 110, 111, 114,
- beam current = 5 µA,
- mesh size = 50 µm,
- different plasma potentials (U_p) and electron temperature (T_e).

As explained before, the aim of these simulations was to find a beam profile as similar as possible to the one shown in Figure 6.27. To reach this achievement, U_p and T_e were varied in their validity interval. The parameters for each run are summarized in Table 6.3.

Beam profiles have been plotted; increasing Up the trend becomes flat, so $U_p = 2$ V is the setting that resembles the real value best. Regarding the electron temperature, its contribute is not significant as the U_p is. Since the ratio obtained with the simulation is slightly different from the experimental one, identifying the electron temperature real value results more difficult. In Figures 6.28 to 6.30 ratios are given for three values of T_e.

It seems that the intermediate case - 2 V and 8000 K - is the closer to reality, even if the shape differs for some features. While the experimental plot rapidly decreases in the center and its trend is clear, the simulated one decreases slowly; at the edge, it can be seen the same low point it can be found at 6 mm in Figure 6.27 - even if in Figure 6.29 is at different position, 2 mm closer to the center. The trouble is that data processing could give rise to different explanations, depending on which bin size is choosen plotting the histogram. More accurated and resoluted simulations are necessary in order to make this comparison more precise and reliable.

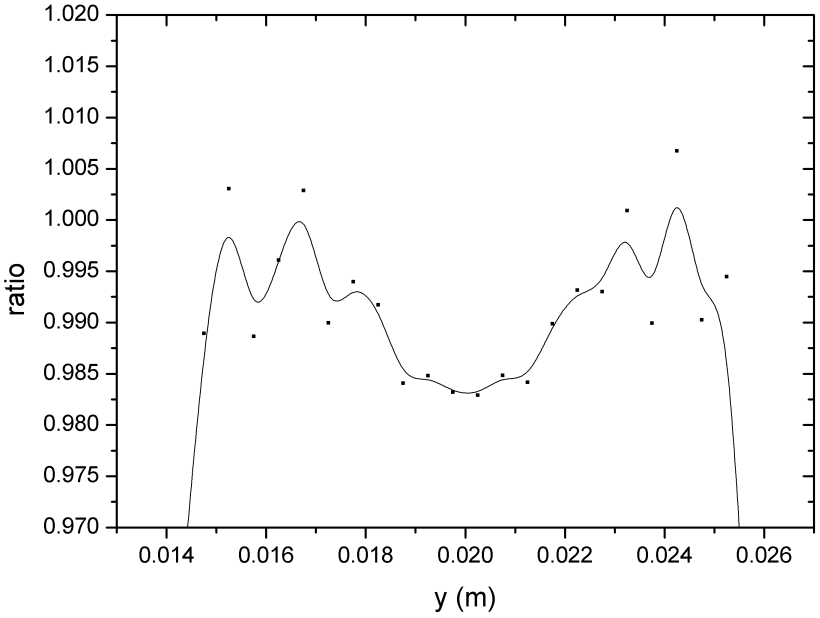

Figure 6.28: ^{114}Cd/^{111}Cd ratio for $U_\mathrm{p} = 2$ V and $T_\mathrm{e} = 5000$ K.

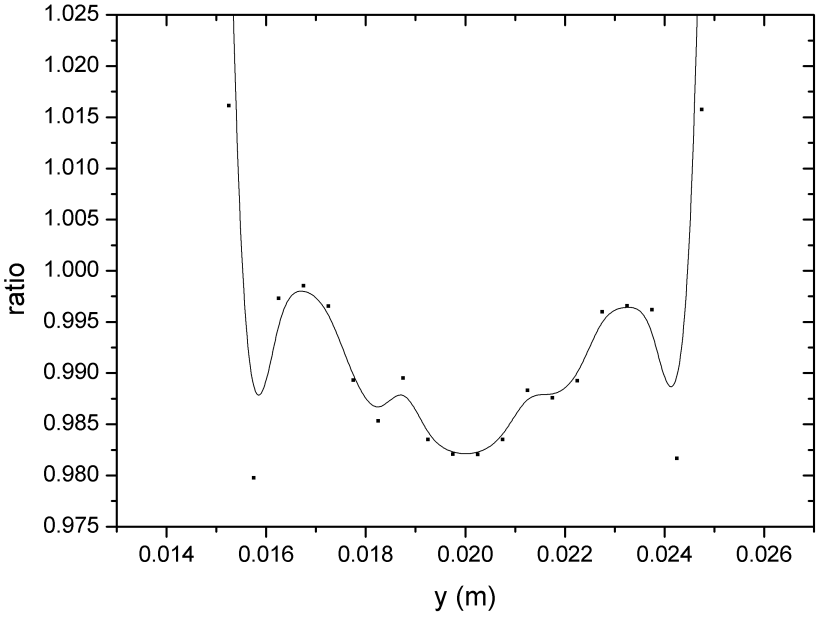

Figure 6.29: ^{114}Cd/^{111}Cd ratio for $U_\mathrm{p} = 2$ V and $T_\mathrm{e} = 8000$ K.

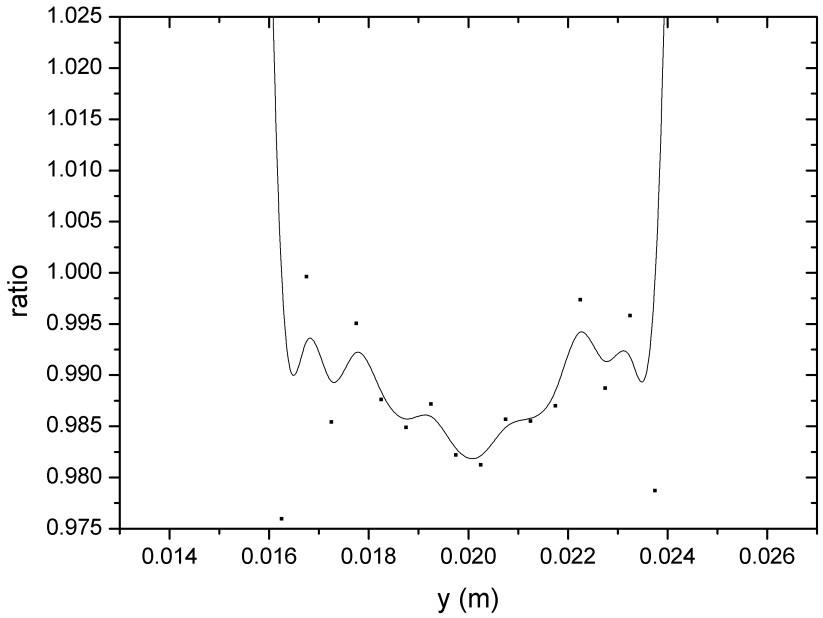

Figure 6.30: ^{114}Cd/^{111}Cd ratio for $U_\mathrm{p} = 2$ V and $T_\mathrm{e} = 10000$ K.

Chapter 7

Results and discussion

The present work wants only to be a starting point in the understanding of the extraction process: in the future, on one hand more simulations and with different softwares can be performed and on the other some improvements can be applied to the instrument. IBSimu already represents a better simulation package compared to SIMION; with the latter, taking into account the space charge effects is difficult and really impractical. Nevertheless, IBSimu still has a liability: it is impossible to fly neutral particles and then simulating the scattering process between neutrals. For this reason the group of Kivel is developing new simulations, both with dsmcFoam[1] and with PI-DSMC (Parallel Interactive Direct Simulation Monte Carlo). Both this programs use the probabilistic (Monte Carlo) simulation to understand the fluidodynamics of the free jet expansion. DSMC has been already documented in some articles [38] [39]; the particular implementation of the algorithm is called FENIX. As the solver in IBSimu, the Monte Carlo algorithm models the gas flow by dividing the simulation region into small spatial collision cells, each one smaller in the extent than the local mean free path. Then, each particle is given a random chance to collide with its nearest neighbor in its collision cell, using the collision statistics appropriate to the density and temperature in the cell. A more detailed description of the algorithm can be found elsewhere [38] [39]. The aim of the FENIX simulation would be to make a more detailed calculation of the flow in the ICP-MS, not limited to the region downstream the skimmer anymore, but in the whole extraction interface. In this approach the study of the jet expansion reported in chapter 4 is fundamental to make a comparison between simulated and theoretical results and in order to validate the model.

This new simulation software is fundamental even for another reason: applying a modest voltage to the skimmer could improve the transmission efficiency. Usually about 10% of the total number of flying particles is lost on the skimmer walls and the trouble is that most of these particles are the lightest. Electrically floating one or both the cones at various potentials could accelerate the ions and therefore reduce this phenomenon. It has been found, with IBSimu, that having the skimmer at few volts would focus the

[1] dsmcFoam is part of the open source CFD package OpenFOAM.

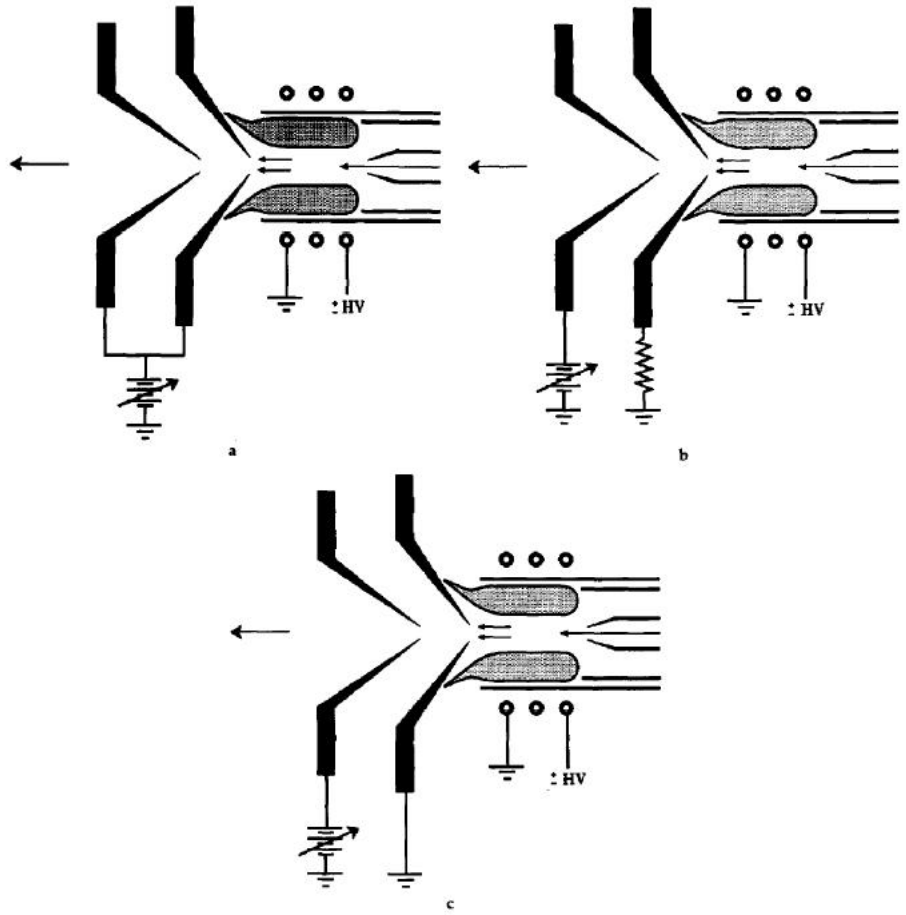

Figure 7.1: Sketches of the three used arrangements [23].

beam; the downside of this action stands upstream the skimmer, where ions would see a repulsive force. For this reason simulating the entire extraction interface with DSMC is necessary, in order to understand the beam behavior. Hu and Houk [23] applied modest DC voltages (+10 to +50 V) to both the sampler and the skimmer or, alternatively, left the sampler floating - i.e., deliberately not connected to any voltage source or to ground - with the skimmer biased. Three specific arrangements (shown in figure 7.1) were studied: (a) sampler and skimmer biased together, (b) sampler floated and skimmer biased and (c) sampler grounded and skimmer biased.

The results are depicted in figure 7.2 with Co^+ as analyte.[2] There is an improvement in each case: by a factor of 4 (modestly) by applying the same DC voltages - about 20 V - to both sampler and skimmer (A), by a factor 5 of in case C, and by a factor of 6 by floating the sampler and applying a DC voltage of $30 - 40\,V$ to the skimmer.

It results that configuration b is the one which gives the higher signal;

[2]"Relative sensitivity" refers to the sensitivity obtained for a given element with one of the new interface arrangements divided by that obtained for the same element with the conventional interface.

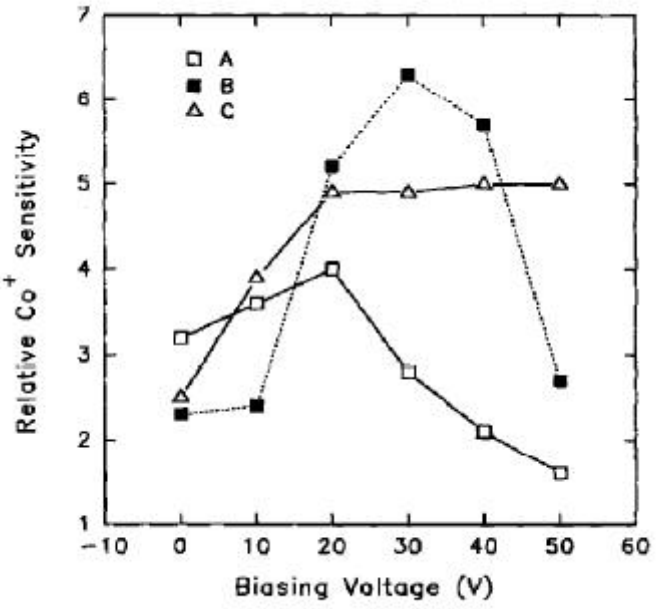

Figure 7.2: Relative Co^+ sensitivity as a function of biasing voltage [23].

Table 7.1: Molar sensitivities for various elements expressed in terms of atomic concentration [23]

	molar sensitivity (counts/ (s · mM))		
interface arrangement	Co $m/z = 59$	Rh $m/z = 103$	Ho $m/z = 165$
conventional interface	$5.6 \cdot 10^7$	$8.5 \cdot 10^7$	$2.2 \cdot 10^8$
interface b	$3.5 \cdot 10^8$	$3.3 \cdot 10^8$	$3.0 \cdot 10^8$

in Table 7.1 molar sensitivities for various elements are compared.

Another advantage given by this configuration is the reducing of the mass bias: in fact, the sensitivity is improved for Co^+ by a much greater factor than is in the case for the heavier Ho^+. Even if it seems that the ions have a sufficient kinetic energy to flow through the sampling cones, some simulations should been run in order to check what happens upstream the skimmer: applicating a positive potential could repel ions and prevent them from passing through the orifice. So in this case the simulation field has to be extended, in order to start the beam in correspondence to the sampler.

Chapter 8

Conclusions

As explained in the introduction, the aim of this work was the optimization of the ion extraction from the ICP. IBSimu turned out to be a suitable and useful instrument for this purpose, thanks to its versatility and easiness of use. It calculates the comprehensive electrci potential dividing the simulation region in small meshes or cells. Once chosen the fastest solver among the many available, the mesh size has been determined in order to have a good compromise between results quality and computing time. At the beginning, the code describing the simulation field was characterized by a 2D mirror geometry; due to some problems, switching to a full geometry came out to be convenient.

Then the main section of the work started: the investigation on how the beam profile changes upon varying the plasma main parameters, i.e. the plasma potential and the electron temperature. Changing the plasma potential, noticeable differences were observed in the beam profile only in the range between 2 and 10 V; increasing U_p more particles collide on the skimmer wall and then the beam profile decreases in intensity flattening. The electron temperature has a less considerable effect and, particularly, its consequence depends on the plasma potential value: if U_p is low, increasing T_e the trend flattens, while if U_p is high nearly nothing changes. Since the aperture to the mass spectrometer is 4 mm wide, the couple of values $U_\mathrm{p} = 2\mathrm{V}$ and $T_\mathrm{e} = 8000\mathrm{K}$ has been chosen in order to have a sharp peak with a high number of counts. This result has been obtained flying only Argon ions, but it has then been ratified simulating a beam with many species.

One of the most severe problem in the Inductively Coupled Plasma Mass Spectrometry is mass discrimination, that is the preferential lost of the beam particles with a low mass in respect to heavier species. This phenomenon has been characterized and then the effect of a plasma potential and electron temperature variation has been studied in order to see if it determines any advantage. While only small and negligible differences occur changing T_e, the logarithmic plot of the number of counts as a function of mass is mitigated by high plasma potentials. This is why, for high U_p, the beam profile has a low number of counts and it is more flat. So the smaller mass discrimination is caused by a higher loss of heavy particles and not by an

improvement of light particles transmission; since this can't be considered as an improvement, $U_{\mathrm{p}} = 2$ V has still to be considered the best plasma potential.

In the case of many particles seeded the iteration settings has been optimized: 24 iterations with Argon only (since the contribution to the total electric potential by other ions is negligible) to define the electric potential and 1 iteration seeding all the other particles. It has also been found to be important to fly many particles in the last run, in order to have a good statistic.

The last task of this work was the characterization of the plasma of the Neptune MC-ICP-MS; the experimental and simulated results obtained for the isotope ratio distribution of Cadmium has been compared. It resulted that 2 V and 8000 K is a couple of values close to the experimental ones, even if more accurated and resoluted simulation would be advisable.

As hinted before, this work is only a small contribution to the optimization of the ion extraction, (a) because other simulation packages could be used, (b) because it could be possible to have the skimmer floating - and in general to change the experimental set up - and, (c) most important, because this simulation only represents the region from the skimmer to the extraction lens. Another critical phase in the extraction process is the one between the sampler and the skimmer, where the free expansion jet takes place. Further studies should go in this direction, investigating and simulating what happens in this region.

Appendices

Appendix A

C++ code

The following is the initial code.

```
/*! \file ibsimu_neptune_new.cpp
 *  \brief Simulation of ion extraction from an ICP into the vacuum with variable charge
    densities for various species
 */


//===========================================================================
//  Paul Scherrer Institute
//  Nuclear Energy and Safety
//  Isotope and Elemental Analysis
//  OHLA / 128
//  5232 Villigen PSI
//  SWITZERLAND
//  Copyright (c) 2012, Niko Kivel and Heiko Potthast. All rights reserved.
//===========================================================================
//
//===========================================================================
//  This software is based on the IBSimu Library by Taneli Kalvas
//  http://ibsimu.sourceforge.net/index.html
//===========================================================================

//---------------------------------------------------------------------------
//  New_Solver since 07/02/2012
//---------------------------------------------------------------------------
#include <cstdlib>
#include <sstream>
```

```
26 #include <fstream>
27 #include <iomanip>
28 #include <stdio.h>
29 //#include <iostream>
30
31
32 #include "epot_gssolver.hpp"
33 #include "epot_umfpacksolver.hpp"
34 #include "epot_bicgstabsolver.hpp"
35 #include "epot_mgsolver.hpp"
36 #include "epot_rbgssolver.hpp"
37
38 #include "particledatabase.hpp"
39 #include "geometry.hpp"
40 #include "convergence.hpp"
41 #include "func_solid.hpp"
42 #include "epot_efield.hpp"
43 #include "meshvectorfield.hpp"
44 #include "ibsimu.hpp"
45 #include "error.hpp"
46 #include "particlediagplotter.hpp"
47 #include "fielddiagplotter.hpp"
48 #include "gtkplotter.hpp"
49 #include "geomplotter.hpp"
50 //------------------------------------------------------------------------------
51
```

```
52 using namespace std;
53
54 double const Pi=4*atan(1); // Pi=3.14
55
56 //*********************************************************************************
57 // start editing here
58 //*********************************************************************************
59
60 //---------------------------------------------------------------------------------
61 // Solver definitions
62 // ATTENTION: Solver selection is now in the simu-function!
63 //---------------------------------------------------------------------------------
64
65 const uint n_iter = 11;   // number of iterations
66 double Epot_error = 1;
67 double Epot_error_last = 1;
68 double Epot_conv = 1e-9;  // Convergence criterion for Epot error in V
69 double SC_conv = 1e-8;  // Convergence criterion for Space charge error in C/m-3
70
71 //---------------------------------------------------------------------------------
72 // Output definitions
73 //---------------------------------------------------------------------------------
74 const bool debug = false; //  print some status information during number crunching
75 const bool verbose = true;  //  print some status information during number crunching
76 const bool GTK = false;   //  open the GUI-based post-prcessing
77 const bool plotting = true; //  produce the output specified in the section PLOTTING
```

```
78 //const bool field_out = false;
79
80 //-------------------------------------------------------------------------
81 // Spectrometer, Beam and Particle definitions
82 //-------------------------------------------------------------------------
83 const double Vacc = -2000.; // Acceleration Voltage (Potential of Lens 1)
84 const double Up = 2.;   // Plasma potential in V
85 const double Te_plasma = 0.69;  // electron Temp of the plasma, 1 k == 8.617343(15)*10-5 eV
       (0.69 eV == 8000 K)
86 const int n_particles =2e1; // number of particles per species
87 //const double Ekin_factor = 0.026; // Ekin_factor * m [amu] = Ekin [eV], approx. 2700 m/s
88 const double Ekin_factor = 0.0406; // Ekin_factor * m [amu] = Ekin [eV], approx 3500 m/s
89
90 // array of ions WITHOUT Ar
91 // The Ar will be added separately because of its higher Charge Density
92 //double masses[] = {1,2,3,4,5,6,7,8,9,10,11,49,50,74,75,99,100,199,200,249,250,299,300};
93 double masses[] = {6, 7 };
94 int n_masses = sizeof(masses)/sizeof(double);
95
96 // array of Ar beam intensities in microamp (uA)
97 //double beams[] = { 0., .001, .002, .003, .004, .005, .006, .007, .008, .009, .01, .02,
       .03, .04, .05, .06, .07, .08, .09, .1, };
98 //double beams[] = { 5,4,3,2,1,0.5,0.4,0.3,0.2,0.1,.09,.08,.07,.06,.05,.04,.03,.02,.01,0};
99 //double beams[] = { 6,7,8,9 };
100 //double beams[] = { 5 };
101 //double beams[] = { 0, 1, 10, 100, 1000, 10000 };
```

```
102 //double beams[] = { 1000, 10000, 20000 };
103 double beams[] = { 0. };
104 int n_beams = sizeof(beams)/sizeof(double);
105
106
107 //*********************************************************************
108 // stop editing here, unless you think you know what you are doing :)
109 //*********************************************************************
110
111 // filename handling function "fname("prefix",number,".file-extension")
112 string fname; //declare variable for filename
113 string fnstring( string prefix, double num, string ext ) {
114   string unit = "_uA";
115   string fname;
116   char numstr[21]; // enough to hold all numbers up to 64-bits
117   // scale 'num' by 1000 and convert to char for string merger
118   sprintf(numstr, "%d", int(num));
119   // merge strings into filename
120   fname = prefix + numstr + unit + ext;
121   return( fname );
122 }
123
124 //---------------------------------------------------------------------
125 // Geometry definitions
126 //---------------------------------------------------------------------
127
```

```
128 //  LENS 1
129 const double rl1 = 0.001;        // radius
130 const double xol1 = 0.0162;      // x center
131 const double yol1 = 0.007;       // y center
132
133 //  Skimmer
134 const double rs = 0.005;         // radius
135 const double xos = 0.003;        // x center
136 const double yos = 0.0074;       // y center
137 const double rso = 0.0004;       // Skimmer orifice radius
138
139 double H = sqrt( pow(xos,2) + pow((yos-rso),2) );
140 double tl = sqrt( pow(H,2) - pow(rs, 2) );
141 double alpha = acos( xos/H ) - asin( rs/H );
142
143 double xt = cos(alpha) * tl;
144 double yt = sin(alpha) * tl;
145
146 //------------------------------------------------------------------------
147 // Geometry BOOL definitions
148 //------------------------------------------------------------------------
149
150 bool solid1( double x, double y, double z )     //Lens 1 + Extension
151 {
152     return( ( x >= 0.0162 && x <= 0.0552 && y >= 0.006 && y <= 0.008) ||
153             ( x >= 0.0542 && x <= 0.0552 && y >= 0.001 && y <= 0.008) ||
```

```
154             ( x >= 0.0522 && x <= 0.0552 && y >= 0.008 && y <= 0.015) ||
155             ( pow((x-xol1),2) + pow((y-yol1),2) <= pow(rl1,2) ) ||
156             ( x >= 0.0552 && y >= 0.0065 && y <= 0.01)
157     );
158 }
159
160 bool solid2(  double x, double y, double z )    //Interface + interface
161 {
162     return(
163             ( x <= xt && y >= ( yt / xt * x + rso ) && y <= 0.015 ) ||    // conical
                  skimmer wall
164             ( x <= rs+xos && y >= yos && y <= 0.015) ||                // skimmer base
165             ( pow((x-xos),2) + pow((y-yos),2) <= pow(rs,2) ) ||             // rounding
                  with r = rs
166
167       ( x <= 0.0092 && y >= 0.0095 ) ||             // tube 1 (1st X-ring mounting body,
             main Interface body)
168             ( x >= 0.0092 && x <= 0.0112 && y >= x + 0.0003 ) ||        // chamfer 1, part
                  of tube 1
169             ( x >= 0.0112 && x <= 0.016 && y >= 0.0145 ) ||             // Slide Valve
                  section
170             ( x >= 0.016 && x <= 0.023 && y >= x - 0.0015 && y <= 0.031) ||             //
                  chamfer 2 ( 2nd X-ring mounting body)
171             ( x >= 0.01 && x <= 0.05 && y >= 2.3*x-0.008) ||
172             ( x >= 0.023 && y >= 0.055)
173     );
```

```
174 }
175
176 //-------------------------------------------------------------------------------
177 // END of Geometry BOOL definitions
178 //-------------------------------------------------------------------------------
179
180 void simu( int *argc, char ***argv, double Ar_beam )
181 {
182 //-------------------------------------------------------------------------------
183 // Geometry
184 //-------------------------------------------------------------------------------
185 //double x_max = 17.; // x dimension in mm
186 //double y_max = 7.;  // y dimension in mm
187 double x_max = 56.; // x dimension in mm
188 double y_max = 16.0;  // y dimension in mm
189 double mesh = 0.05; // mesh size in mm
190   Geometry geom( MODE_2D, Int3D((x_max/mesh)+1,(y_max/mesh)+1,1), Vec3D(0,0,0), mesh/1000 )
        ;
191 //  Geometry geom( MODE_CYL, Int3D(1121,301,1), Vec3D(0,0,0), 5e-5 );
192 //  Geometry geom( MODE_CYL, Int3D(2241,601,1), Vec3D(0,0,0), 2.5e-5 );
193 //  Geometry geom( MODE_CYL, Int3D(561,151,1), Vec3D(0,0,0), 1e-4 );
194
195   Solid *s1 = new FuncSolid( solid1 );
196     geom.set_solid( 7, s1 );
197   Solid *s2 = new FuncSolid( solid2 );
198     geom.set_solid( 8, s2 );
```

```
199
200   geom.set_boundary( 1, Bound(BOUND_NEUMANN,     0.0 ) );       // X_min
201   geom.set_boundary( 2, Bound(BOUND_NEUMANN,     0.0) );        // X_max
202   geom.set_boundary( 3, Bound(BOUND_NEUMANN,     0.0) );        // Y_min
203   geom.set_boundary( 4, Bound(BOUND_NEUMANN,     0.0) );        // Y_max
204   geom.set_boundary( 7, Bound(BOUND_DIRICHLET,   Vacc)  );
205   geom.set_boundary( 8, Bound(BOUND_DIRICHLET,   0.0) );
206
207   geom.build_mesh();
208
209   if ( debug ) geom.debug_print( cout );
210
211 //-------------------------------------------------------------------------
212 //  SOLVER NEW
213 //-------------------------------------------------------------------------
214
215 //  EpotGSSolver solver( geom );
216
217 /*
218   EpotMGSolver solver( geom );
219   solver.set_levels( 3 );
220   solver.set_neumann_order( 2 );
221 */
222   EpotUMFPACKSolver solver( geom );
223   solver.set_newton_residual_eps( 1e-5 );   // default = 1e-5
224   solver.set_newton_step_eps( 1e-6 );   // default = 1e-6
```

```
225   solver.set_newton_imax( 101 );      // default = 10
226
227   InitialPlasma initp( AXIS_X, 1e-8 );
228   solver.set_initial_plasma( Up, &initp );
229
230   EpotField epot( geom );
231   MeshScalarField scharge( geom );
232   MeshVectorField bfield;
233   EpotEfield efield( epot );
234
235   if ( debug ) efield.debug_print( cout );
236
237 //-------------------------------------------------------------------------
238 // Fields
239 //-------------------------------------------------------------------------
240
241   field_extrpl_e efldextrpl[6] = {  FIELD_EXTRAPOLATE, FIELD_EXTRAPOLATE,
242                     FIELD_MIRROR,      FIELD_EXTRAPOLATE,
243                     FIELD_EXTRAPOLATE, FIELD_EXTRAPOLATE };
244   efield.set_extrapolation( efldextrpl );
245
246 //-------------------------------------------------------------------------
247 // Beam
248 //-------------------------------------------------------------------------
249
250 //calculation of the Ar charge density for the first beam in A/m2
```

```
251 double Chdensity_Ar = (Ar_beam * 1e-12) / ( pow((rso/1000),2)*Pi );
252 //double Chdensity_Ar = 1.5;  // charge density of Ar in A/m2
253
254 //-----------------------------------------------------------------------------
255 // Particles
256 //-----------------------------------------------------------------------------
257
258   ParticleDataBase2D pdb;
259   bool pmirror[6] = { false, false, true, false, false, false };
260   pdb.set_mirror( pmirror );
261   pdb.set_polyint( true );
262
263 //-----------------------------------------------------------------------------
264 //  convergence determination
265 //  only new_solver
266 //-----------------------------------------------------------------------------
267   Emittance emit;
268
269   Convergence conv;
270   conv.add_epot( epot );
271   conv.add_scharge( scharge );
272   conv.add_emittance( 0, emit );
273 //-----------------------------------------------------------------------------
274
275 //-----------------------------------------------------------------------------
276 //  Iteration Loop
```

```
277 //-------------------------------------------------------------------------
278   for( size_t i = 0; i < n_iter; i++ ) {
279     if(verbose){
280       printf("*********************************************************\n\n");
281       printf("\t iteration %d of max %d\n", int(i)+1, int(n_iter) );
282       printf("\t Beam Current = %f uA\n", Ar_beam);
283       printf("\t Charge-Density = %f A m-2\n", Chdensity_Ar);
284       printf("\n*********************************************************\n");
285     }
286     if( i == 1 ) {
287       double rhoe = pdb.get_rhosum();
288       solver.set_pexp_plasma( -rhoe, Te_plasma, Up );
289     }
290     solver.solve( epot, scharge );
291     if(verbose){
292       printf("-------------------------------------------------------------\n");
293       printf("RhoSum = %f\n", -pdb.get_rhosum());
294       printf("-------------------------------------------------------------\n");
295     }
296
297     efield.recalculate(); // only new_solver
298
299 //    clear particle data base
300     pdb.clear();
301     if(verbose){
302       printf("-------------------------------------------------------------\n");
```

```
303       printf("Particle data base cleared\n");
304       printf("-------------------------------------------------------------\n");
305     }
306
307 //    seed particles
308 //    1st some Argon with variable Charge Density from the array "beams[]"
309     double M = 40.0;
310 //    pdb.add_2d_beam_with_energy(  n_particles, Chdensity_Ar, 1.0, M,
311 //                      Ekin_factor * M, 0.2, Ekin_factor * M * .001,
312 //                      0.0, 0.0,
313 //                      0.0, rso );
314     pdb.add_2d_KV_beam_with_emittance(  n_particles, Ar_beam/1e6, 1.0, M,
315                       0.04978, 0.0107, 5e-6,
316                       Ekin_factor * M, 0.0, rso);
317
318 //    2nd some real ions from the array "masses[]" with constant charge density
319
320     double Chdensity_S = 0.001; // Charge density for the minor species
321
322     for( size_t m=0; m < uint(n_masses); m++){
323       pdb.add_2d_beam_with_energy(  n_particles, Chdensity_S, 1.0, masses[m],
324                       Ekin_factor * masses[m], 0.2, Ekin_factor * masses[m] * .001,
325                       0.0, 0.0,
326                       0.0, rso );
327     }
328
```

```
329 // acutal data crunch
330     pdb.iterate_trajectories( scharge, efield, bfield, geom );
331 
332 //    pdb.debug_print( cout );  // print trajectory of each particle to std:out
333 
334     ParticleDiagPlotter pplotter( geom, pdb, AXIS_X, 0.01,
335                     PARTICLE_DIAG_PLOT_SCATTER,
336                     DIAG_Y, DIAG_YP );
337     emit = pplotter.calculate_emittance();
338     conv.evaluate_iteration();
339 
340     ofstream ofconv( "convergence.dat" );
341     conv.print_history( ofconv );
342     conv.print_history( cout );
343     ofconv.close();
344 
345       if(i==2 && n_iter >=3){
346         FILE* pipe = popen("gnuplot -persist plot.gp","w");
347 //        fprintf(pipe, "set logscale y\n");
348 //        fprintf(pipe, "plot 'convergence.dat' using 1:2 with lines title 'EPot error' ,
349 //        'convergence.dat' using 1:3 with lines title 'SCharge error'\n");
350         fclose(pipe);
351       }
352       if(i>=3){
353 //        fprintf(pipe, "replot\n");
354       }
```

```
355
356
357     if(verbose){
358       printf("-----------------------------------------------------------------\n");
359       printf("  Beam characteristics:\n");
360       printf("  alpha = %f\n",emit.alpha());
361       printf("  beta = %f m/rad\n",emit.beta());
362       printf("  gamma = %f rad/m\n",emit.gamma());
363       printf("  rms emittance = %f mm mrad\n",1e6*emit.epsilon());
364       printf("-----------------------------------------------------------------\n");
365     }
366
367 // conv.eval becomes true when the both criterions are reached --> stop iteration
368 /*    if( conv.evaluate_iteration( Epot_conv, SC_conv ) ){
369       printf("=================================================================\n");
370       printf("\tConverged (Epot err < %e V), starting post-processing\n", Epot_conv);
371       printf("=================================================================\n");
372       i = n_iter;
373     }
374 */
375     }
376 //-------------------------------------------------------------------------
377 //  End of iteration loop
378 //-------------------------------------------------------------------------
379
380 //-------------------------------------------------------------------------
```

```
381 //  summarize the data from the iterations
382 //-------------------------------------------------------------------------
383 //  Convergence to std::out and file
384   ofstream ofconv( "convergence.dat" );
385   conv.print_history( ofconv );
386   conv.print_history( cout );
387   ofconv.close();
388   FILE* pipe = popen("mv convergence.dat convergence_$(date +%Y%m%d_%H%M%S).dat","w");
389   fclose(pipe);
390 // End of Summary
391
392 //-------------------------------------------------------------------------
393 // Evaluation and Eye-Candy
394 //-------------------------------------------------------------------------
395
396 if( plotting ){
397 //-------------------------------------------------------------------------
398 //  particle traces full and zoom
399 //-------------------------------------------------------------------------
400   GeomPlotter geomplotter( geom );
401   geomplotter.set_font_size( 36 );
402   geomplotter.set_size( 1920, 1080 );
403 //  geomplotter.set_eqlines_auto( 51 );
404   geomplotter.set_epot( &epot );
405   geomplotter.set_scharge( &scharge );
406   geomplotter.set_particle_database( &pdb );
```

```
fname = fnstring("particle_traces_", Ar_beam, ".png");
geomplotter.plot_png( fname );
fname = fnstring("particle_traces_", Ar_beam, ".pdf");
geomplotter.plot_pdf( fname );

geomplotter.set_ranges( 0, 0, 0.01, 0.002 );
fname = fnstring("particle_traces_zoom_",Ar_beam,".png");
geomplotter.plot_png( fname );
fname = fnstring("particle_traces_zoom_",Ar_beam,".pdf");
geomplotter.plot_pdf( fname );

geomplotter.set_ranges( 0, 0, 0.01, 0.002 );
geomplotter.set_fieldgraph_plot( FIELD_EPOT );
geomplotter.set_particle_div( 0 );
fname = fnstring("fieldgraph_Epot_zoom_",Ar_beam,".png");
geomplotter.plot_png( fname );
fname = fnstring("fieldgraph_Epot_zoom_",Ar_beam,".pdf");
geomplotter.plot_pdf( fname );

geomplotter.set_ranges( 0, 0, x_max, y_max );
geomplotter.set_fieldgraph_plot( FIELD_EPOT );
geomplotter.set_particle_div( 0 );
fname = fnstring("fieldgraph_Epot_",Ar_beam,".png");
geomplotter.plot_png( fname );
fname = fnstring("fieldgraph_Epot_",Ar_beam,".pdf");
geomplotter.plot_pdf( fname );
```

```
433
434   geomplotter.set_ranges( 0, 0, 0.01, 0.002 );
435   geomplotter.set_fieldgraph_plot( FIELD_SCHARGE );
436   geomplotter.set_particle_div( 0 );
437   fname = fnstring("fieldgraph_SCharge_zoom_",Ar_beam,".png");
438   geomplotter.plot_png( fname );
439   fname = fnstring("fieldgraph_SCharge_zoom_",Ar_beam,".pdf");
440   geomplotter.plot_pdf( fname );
441
442   geomplotter.set_ranges( 0, 0, x_max, y_max );
443   geomplotter.set_fieldgraph_plot( FIELD_SCHARGE );
444   geomplotter.set_particle_div( 0 );
445   fname = fnstring("fieldgraph_SCharge_",Ar_beam,".png");
446   geomplotter.plot_png( fname );
447   fname = fnstring("fieldgraph_SCharge_",Ar_beam,".pdf");
448   geomplotter.plot_pdf( fname );
449
450 //-------------------------------------------------------------------------
451 //  Emittance @ 50 mm
452 //-------------------------------------------------------------------------
453   ParticleDiagPlotter pplotter1(  geom, pdb, AXIS_X, 5e-2,
454                   PARTICLE_DIAG_PLOT_HISTO2D,
455                   DIAG_Y, DIAG_YP );
456   pplotter1.set_font_size( 36 );
457   pplotter1.set_size( 1920, 1080 );
458   fname = fnstring("emittance_50mm_", Ar_beam, ".png");
```

```
459   pplotter1.plot_png( fname );
460   fname = fnstring("emittance_50mm_", Ar_beam, ".pdf");
461   pplotter1.plot_pdf( fname );
462   fname = fnstring("emittance_50mm_", Ar_beam, ".txt");
463   pplotter1.export_data( fname );
464 //-------------------------------------------------------------------------
465 //  beam profile @ 50 mm
466 //-------------------------------------------------------------------------
467   ParticleDiagPlotter profile(  geom, pdb, AXIS_X, 0.05,
468                   PARTICLE_DIAG_PLOT_HISTO1D,
469                   DIAG_Y );
470   profile.set_font_size( 36 );
471   profile.set_histogram_n( 301 );
472   profile.set_size( 1920, 1080 );
473   fname = fnstring("profile_50mm_", Ar_beam,".png");
474   profile.plot_png( fname );
475   fname = fnstring("profile_50mm_", Ar_beam,".pdf");
476   profile.plot_pdf( fname );
477   fname = fnstring("profile_50mm_", Ar_beam,".dat");
478   profile.export_data( fname );
479 //-------------------------------------------------------------------------
480 //  beam profile @ 4 mm
481 //-------------------------------------------------------------------------
482
483   ParticleDiagPlotter profile4( geom, pdb, AXIS_X, 0.004,
484                   PARTICLE_DIAG_PLOT_HISTO1D,
```

```
485                     DIAG_Y );
486   profile4.set_font_size( 36 );
487   profile4.set_histogram_n( 301 );
488   profile4.set_size( 1920, 1080 );
489   fname = fnstring("profile_4mm_", Ar_beam,".png");
490   profile4.plot_png( fname );
491   fname = fnstring("profile_4mm_", Ar_beam,".pdf");
492   profile4.plot_pdf( fname );
493   fname = fnstring("profile_4mm_", Ar_beam,".dat");
494   profile4.export_data( fname );
495
496 //-------------------------------------------------------------------------
497 //  E_kin @ 50 mm
498 //-------------------------------------------------------------------------
499 /*
500   ParticleDiagPlotter Ekin( geom, pdb, AXIS_X, 0.05,
501                 PARTICLE_DIAG_PLOT_HISTO1D,
502                 DIAG_EK );
503   Ekin.set_font_size( 36 );
504   Ekin.set_histogram_n( 4000 );
505   Ekin.set_size( 1920, 1080 );
506   fname = fnstring("Ekin_50mm_", Ar_beam,".png");
507   Ekin.plot_png( fname );
508   fname = fnstring("Ekin_50mm_", Ar_beam,".pdf");
509   Ekin.plot_pdf( fname );
510   fname = fnstring("Ekin_50mm_", Ar_beam,".dat");
```

```
511   Ekin.export_data( fname );
512 */
513 //-------------------------------------------------------------------------------
514 //  mass spectrum @ 8 mm
515 //-------------------------------------------------------------------------------
516
517   ParticleDiagPlotter massspec8(  geom, pdb, AXIS_X, 0.008,
518                   PARTICLE_DIAG_PLOT_HISTO1D,
519                   DIAG_MASS );
520   massspec8.set_font_size( 36 );
521   massspec8.set_histogram_n( 901 );
522   massspec8.set_size( 1920, 1080 );
523   fname = fnstring("mass_spectrum_8mm_", Ar_beam,".png");
524   massspec8.plot_png( fname );
525   fname = fnstring("mass_spectrum_8mm_", Ar_beam,".pdf");
526   massspec8.plot_pdf( fname );
527   fname = fnstring("mass_spectrum_8mm_", Ar_beam,".dat");
528   massspec8.export_data( fname );
529
530 //-------------------------------------------------------------------------------
531 //  mass spectrum @ 50 mm
532 //-------------------------------------------------------------------------------
533   ParticleDiagPlotter massspec( geom, pdb, AXIS_X, 0.05,
534                   PARTICLE_DIAG_PLOT_HISTO1D,
535                   DIAG_MASS );
536   massspec.set_font_size( 36 );
```

```
massspec.set_histogram_n( 901 );
massspec.set_size( 1920, 1080 );
fname = fnstring("mass_spectrum_50mm_", Ar_beam,".png");
massspec.plot_png( fname );
fname = fnstring("mass_spectrum_50mm_", Ar_beam,".pdf");
massspec.plot_pdf( fname );
fname = fnstring("mass_spectrum_50mm_", Ar_beam,".dat");
massspec.export_data( fname );
//-------------------------------------------------------------------------------
//  mass spectrum @ 56 mm
//-------------------------------------------------------------------------------
ParticleDiagPlotter massspec1( geom, pdb, AXIS_X, 0.056, PARTICLE_DIAG_PLOT_HISTO1D,
   DIAG_CURR );
massspec1.set_font_size( 36 );
massspec1.set_histogram_n( 901 );
massspec1.set_size( 1920, 1080 );
fname = fnstring("mass_spectrum_56mm_", Ar_beam,".png");
massspec1.plot_png( fname );
fname = fnstring("mass_spectrum_56mm_", Ar_beam,".pdf");
massspec1.plot_pdf( fname );
fname = fnstring("mass_spectrum_56mm_", Ar_beam,".dat");
massspec1.export_data( fname );
//-------------------------------------------------------------------------------
//  scatter 1 @ 50 mm
//-------------------------------------------------------------------------------
```

```
561   ParticleDiagPlotter scatter_1( geom, pdb, AXIS_X, 0.05, PARTICLE_DIAG_PLOT_SCATTER,
          DIAG_MASS, DIAG_Y );
562   scatter_1.set_font_size( 36 );
563 //  scatter_1.set_histogram_n( 251 );
564 //  scatter_1.set_histogram_m( 251 );
565   scatter_1.set_size( 1920, 1080 );
566   fname = fnstring("scatter_50mm_", Ar_beam,".png");
567   scatter_1.plot_png( fname );
568   fname = fnstring("scatter_50mm_", Ar_beam,".pdf");
569   scatter_1.plot_pdf( fname );
570   fname = fnstring("scatter_50mm_", Ar_beam,".dat");
571   scatter_1.export_data( fname );
572 //-------------------------------------------------------------------------
573 //  Field Diagnostics @ 56 mm
574 //-------------------------------------------------------------------------
575   FieldDiagPlotter fplotter( geom );
576   fplotter.set_font_size( 18 );
577   fplotter.set_scharge( &scharge );
578   fplotter.set_epot( &epot );
579   fplotter.set_coordinates( 1000, Vec3D(0,0,0), Vec3D(56e-3,0,0) );
580
581   field_diag_type_e diag[2] = {FIELDD_DIAG_EPOT, FIELDD_DIAG_NONE};
582   field_loc_type_e loc[2] = {FIELDD_LOC_X, FIELDD_LOC_NONE};
583   fplotter.set_diagnostic( diag, loc );
584   fname = fnstring("fielddiagplot_Pot_",Ar_beam,".png");
585   fplotter.plot_png( fname );
```

```
586   fname = fnstring("fielddiagplot_Pot_",Ar_beam,".dat");
587   fplotter.export_data( fname );
588
589   field_diag_type_e diag2[2] = {FIELDD_DIAG_SCHARGE, FIELDD_DIAG_NONE};
590   field_loc_type_e loc2[2] = {FIELDD_LOC_X, FIELDD_LOC_NONE};
591   fplotter.set_diagnostic( diag2, loc2 );
592   fname = fnstring("fielddiagplot_phi_",Ar_beam,".png");
593   fplotter.plot_png( fname );
594   fname = fnstring("fielddiagplot_phi_",Ar_beam,".dat");
595   fplotter.export_data( fname );
596 } // end of plotting
597
598 if( GTK ) {
599     GTKPlotter plotter( argc, argv );
600     plotter.set_geometry( &geom );
601     plotter.set_epot( &epot );
602     plotter.set_scharge( &scharge );
603     plotter.set_particledatabase( &pdb );
604     plotter.new_geometry_plot_window();
605     plotter.run();
606 } // end GTK
607
608 } // end ibsimu
609
610 int main( int argc, char **argv)
611 {
```

```
612   try {
613 //    ibsimu.set_verbose_output( 1 ); //old style
614     ibsimu.set_message_threshold( MSG_VERBOSE, 1 ); // new_solver
615     ibsimu.set_thread_count( 12 );
616     for( size_t b = 0; b < uint(n_beams); b++){
617       simu( &argc, &argv, beams[b] );
618     }
619   }
620
621   catch ( Error e ) {
622     e.print_error_message( std::cout );
623     exit( 1 );
624   }
625   return( 0 );
626 }
```

Bibliography

[1] Megh Nad Saha. Liii. ionization in the solar chromosphere. *Philosophical Magazine Series 6*, 40(238):472–488, 1920.

[2] Arthur Kantrowitz and Jerry Grey. A high intensity source for the molecular beam. part i. theoretical. *Review of Scientific Instruments*, 22(5):328–332, 1951.

[3] Harry Ashkenas and Frederick S Sherman. The structure and utilization of supersonic free jets in low density wind tunnels(inviscid and viscous flow in central core of supersonic free jet in wind tunnel, noting shock wave location at high reynolds number). *Rarefied gas dynamics, proceedings of the Toronto, Canada*, pages 84–105, 1966.

[4] Roger Campargue. Aerodynamic separation effect on gas and isotope mixtures induced by invasion of the free jet shock wave structure. *The Journal of Chemical Physics*, 52:1795–1802, 1970.

[5] Velmer A. Fassel. Quantitative elemental analyses by plasma emission spectroscopy. *Science*, 202(10):183–191, 1978.

[6] Robert S. Houk, Velmer A. Fassel, Gerald D. Flesch, Harry J. Svec, Alan L. Gray, and Charles E. Taylor. Inductively coupled argon plasma as an ion source for mass spectrometric determination of trace elements. *Analytical Chemistry*, 52(14):2283–2289, 1980.

[7] S. R. Koirtyohann, J. Stephen Jones, and Dennis A. Yates. Nomenclature system for the low-power argon inductively coupled plasma. *Analytical Chemistry*, 52(12):1965–1966, 1980.

[8] Alan L. Gray and Alan R. Date. Inductively coupled plasma source mass spectrometry using continuum flow ion extraction. *Analyst*, 108:1033–1050, 1983.

[9] A. Höglund and L-G. Rosengren. A new sensitive molecular beam mass spectrometer. *International Journal of Mass Spectrometry and Ion Processes*, 60(1):173 – 187, 1984.

[10] Jose A. Olivares and R. S. Houk. Ion sampling for inductively coupled plasma mass spectrometry. *Analytical Chemistry*, 57(13):2674–2679, 1985.

[11] Alan L. Gray. Communication. influence of load coil geometry on oxide and doubly charged ion response in inductively coupled plasma source mass spectrometry. *J. Anal. At. Spectrom.*, 1:247–249, 1986.

[12] R. S. Houk. Mass spectrometry of inductively coupled plasmas. *Analytical Chemistry*, 58(1):91A–105A, 1986.

[13] Alan L. Gray, R. S. Houk, and John G. Williams. Langmuir probe potential measurements in the plasma and their correlation with mass spectral characteristics in inductively coupled plasma mass spectrometry. *J. Anal. At. Spectrom.*, 2:13–20, 1987.

[14] D. J. Douglas and J. B. French. Gas dynamics of the inductively coupled plasma mass spectrometry interface. *J. Anal. At. Spectrom.*, 3:743–747, 1988.

[15] George R. Gillson, Donald J. Douglas, John E. Fulford, Kenneth W. Halligan, and Scott D. Tanner. Nonspectroscopic interelement interferences in inductively coupled plasma mass spectrometry. *Analytical Chemistry*, 60(14):1472–1474, 1988.

[16] Neil Bradshaw, Edward F. H. Hall, and Neil E. Sanderson. Communication. inductively coupled plasma as an ion source for high-resolution mass spectrometry. *J. Anal. At. Spectrom.*, 4:801–803, 1989.

[17] Masatoshi Morita, Hiroyasu Ito, Takashi Uehiro, and Kiichiro Otsuka. High resolution mass spectrometry with inductively coupled argon plasma ionization source. *Analytical Sciences*, 5:609–610, 1989.

[18] H.B. Lim and R.S. Houk. Langmuir probe measurement of electron temperature in a supersonic jet extracted from an inductively coupled plasma. *Spectrochimica Acta Part B: Atomic Spectroscopy*, 45(4/5):453 – 461, 1990.

[19] D.M. Chambers, J. Poehlman, P. Yang, and G.M. Hieftje. Fundamental studies of the sampling process in an inductively coupled plasma mass spectrometer-i: Langmuir probe measurements. *Spectrochimica Acta Part B: Atomic Spectroscopy*, 46(6/7):741 – 760, 1991.

[20] B.S. Ross, Pengyuan Yang, D.M. Chambers, and G.M. Hieftje. Comparison of center-tapped and inverted load-coil geometries for inductively coupled plasma-mass spectrometry. *Spectrochimica Acta Part B: Atomic Spectroscopy*, 46(13):1667 – 1687, 1991.

[21] Scott D. Tanner. Space charge in icp-ms: calculation and implications. *Spectrochimica Acta Part B: Atomic Spectroscopy*, 47(6):809 – 823, 1992.

[22] Ke Hu, P. Scott Clemons, and R. S. Houk. Inductive coupled plasma mass spectrometry with an enlarged sampling orifice and offset ion lens.

i. ion trajectories and detector performance. *Journal of the American Society for Mass Spectrometry*, 4(1):16 – 27, 1993.

[23] Ke Hu and R. S. Houk. Inductively coupled plasma mass spectrometry with an electrically floating sampling interface. *Journal of the American Society for Mass Spectrometry*, 4(9):733 – 741, 1993.

[24] Ulrich Gießmann and Ulrich Greb. High resolution icp-ms — a new concept for elemental mass spectrometry. *Fresenius' Journal of Analytical Chemistry*, 350:186–193, 1994.

[25] Alan L. Gray. Inductively coupled plasma mass spectrometry in maturity-what problems remain? *Anal. Proc.*, 31:371–375, 1994.

[26] Hongsen Niu and R.S. Houk. Langmuir probe measurements of the ion extraction process in inductively coupled plasma mass spectrometry-i. spatially resolved determination of electron density and electron temperature. *Spectrochimica Acta Part B: Atomic Spectroscopy*, 49(12-14):1283 – 1303, 1994.

[27] Hongsen Niu, Shen Luan, Ho-Ming Pang, and R. S. Houk. Langmuir probe measurements of the ion extraction process in inductively coupled plasma-mass spectrometry. part 2. measurements of floating voltage and radiofrequency voltage. *Spectrochimica Acta Part B: Atomic Spectroscopy*, 50(10):1247 – 1261, 1995.

[28] Xiaoshan Chen and R. S. Houk. Spatially resolved measurements of ion density behind the skimmer of an inductively coupled plasma mass spectrometer. *Spectrochimica Acta Part B: Atomic Spectroscopy*, 51(1):41 – 54, 1996.

[29] Hongsen Niu and R. S. Houk. Fundamental aspects of ion extraction in inductively coupled plasma mass spectrometry. *Spectrochimica Acta Part B: Atomic Spectroscopy*, 51(8):779 – 815, 1996.

[30] Terry N. Olney, Wei Chen, and D. J. Douglas. Gas dynamics of the icp-ms interface: impact pressure probe measurements of gas flow profiles. *J. Anal. At. Spectrom.*, 14:9 – 17, 1999.

[31] Brett S. Duersch. The effects of a torch shield on performance of the vacuum interface of an inductively coupled plasma mass spectrometer. *J. Anal. At. Spectrom.*, 14:615–619, 1999.

[32] Pengyuan Yang, Julie A. Horner, Norman N. Sesi, and Gary M. Hieftje. Comparison of simulated and experimental fundamental icp parameters. *Spectrochimica Acta Part B: Atomic Spectroscopy*, 55(12):1833 – 1845, 2000.

[33] Nicolas G. Hadjiconstantinou. The limits of navier-stokes theory and kinetic extensions for describing small-scale gaseous hydrodynamics. *Physics of Fluids*, 18(11):111301/1–19, 2006.

[34] W. Neil Radicic, Jordan B. Olsen, Rebecca V. Nielson, Jeffrey H. Macedone, and Paul B. Farnsworth. Characterization of the supersonic expansion in the vacuum interface of an inductively coupled plasma mass spectrometer by high-resolution diode laser spectroscopy. *Spectrochimica Acta Part B: Atomic Spectroscopy*, 61(6):686 – 695, 2006.

[35] Gerardo Gamez, Scott A. Lehn, Mao Huang, and Gary M. Hieftje. Effect of mass spectrometric sampling interface on the fundamental parameters of an inductively coupled plasma as a function of its operating conditions: Part i. applied r.f. power and vacuum. *Spectrochimica Acta Part B: Atomic Spectroscopy*, 62(4):357 – 369, 2007.

[36] Gerardo Gamez, Scott A. Lehn, Mao Huang, and Gary M. Hieftje. Effect of mass spectrometric sampling interface on the fundamental parameters of an inductively coupled plasma as a function of its operating conditions: Part ii. central-gas flow rate and sampling depth. *Spectrochimica Acta Part B: Atomic Spectroscopy*, 62(4):370 – 377, 2007.

[37] Jennifer Griffiths. A brief history of mass spectrometry. *Analytical Chemistry*, 80(15):5678–5683, 2008.

[38] Paul B. Farnsworth, Ross L. Spencer, W. Neil Radicic, Nicholas Taylor, Jeffrey Macedone, and Haibin Ma. A comparison of ion and atom behavior in the first stage of an inductively coupled plasma mass spectrometer vacuum interface: Evidence of the effect of an ambipolar electric field. *Spectrochimica Acta Part B: Atomic Spectroscopy*, 64(9):905 – 910, 2009.

[39] Ross L. Spencer, Jaron Krogel, Jamie Palmer, Adam Payne, Andrew Sampson, William Somers, and Charles N. Woods. Modeling the gas flow upstream and in the sampling nozzle of the inductively coupled plasma mass spectrometer via the direct simulation monte carlo algorithm. *Spectrochimica Acta Part B: Atomic Spectroscopy*, 64(3):215 – 221, 2009.

[40] T. Kalvas, O. Tarvainen, T. Ropponen, O. Steczkiewicz, J. Arje, and H. Clark. Ibsimu: A three-dimensional simulation software for charged particle optics. *Review of Scientific Instruments*, 81(2), 2010.

[41] Norbert Jakubowski, Thomas Prohaska, Frank Vanhaecke, Peter H. Roos, and Torsten Lindemann. Inductively coupled plasma- and glow discharge plasma-sector field mass spectrometry part i. tutorial: Fundamentals and instrumentation. *J. Anal. At. Spectrom.*, 26:693–726, 2011.

[42] Norbert Jakubowski, Thomas Prohaska, Frank Vanhaecke, Peter H. Roos, and Torsten Lindemann. Inductively coupled plasma- and glow discharge plasma-sector field mass spectrometry part ii. applications. *J. Anal. At. Spectrom.*, 26:727–757, 2011.

[43] Niko Kivel, Ines Günther-Leopold, Frank Vanhaecke, and Detlef Günther. Isotope fractionation during ion beam formation in multi-collector inductively coupled plasma mass spectrometry. *Spectrochimica Acta Part B: Atomic Spectroscopy*, 76(0):126 – 132, 2012.

[44] Nicholas Taylor and Paul B. Farnsworth. Experimental characterization of the effect of skimmer cone design on shock formation and ion transmission efficiency in the vacuum interface of an inductively coupled plasma mass spectrometer. *Spectrochimica Acta Part B: Atomic Spectroscopy*, 69(0):2 – 8, 2012.

[45] J. A. C. Broekaert. *Analytical Atomic Spectrometry with Flames and Plasmas*. Wiley-VCH, 2005.

[46] Chhabil Dass. *Fundamentals of contemporary mass spectrometry*. Wiley, 2007.

[47] J.B. French. *Molecular beams for rarefied gasdynamic research*. Wilbur C. Nelson, 1966.